THE H. NIEWODNICZAŃSKI INSTITUTE OF NUCLEAR PHYSICS
POLISH ACADEMY OF SCIENCES

DOCTORAL THESIS

Search for baryon and lepton number violation in heavy baryon decays and the background studies for exotic searches

Author:
Bartłomiej RACHWAŁ

Supervisor:
Prof. Tadeusz LESIAK
Auxiliary supervisor:
Assoc. Prof. Marcin KUCHARCZYK

A thesis submitted in fulfilment of the requirements for the degree of Doctor of Philosophy

Kraków, July 2016

"We are not talking about a confirmation of an established theory, but about opening a door into an unknown and unexplored world."

Gian Giudice

Abstract

Search for baryon and lepton number violation in heavy baryon decays and the background studies for exotic searches

The thesis describes searches for baryon and lepton number violation in $X_b \to K^-\mu^+$ ($X_b = \Lambda_b, \Xi_b^0$) decays. The study is performed in the LHC*b* experiment using data sample corresponding to an integrated luminosity of 3.0 fb^{-1} of proton-proton collisions at the centre-of-mass energy of 7 TeV (8 TeV), collected in 2011 (2012), respectively. No statistically significant signal of the decays in question has been found. As a result, the upper limits have been set: $\mathcal{B}(\Lambda_b \to K^-\mu^+) < 3.6 \times 10^{-9}$ and $\mathcal{B}(\Xi_b^0 \to K^-\mu^+) < 1.8 \times 10^{-8}$ at the 95% confidence level.

The second part of the thesis presents the background studies for exotic searches. The measurement of $\sigma(b\bar{b})$ and $\sigma(c\bar{c})$ production cross-sections with $b-(c-)$ hadron inclusive final states has been performed with data collected by the LHC*b* experiment in 2010 in proton-proton collisions at the centre-of-mass energy of 7 TeV. The author of this thesis has prepared the interface to the Next-To-Leading-Order POWHEG simulation framework into the LHC*b* software chain. All the kinematic characteristics of the hadron production in proton-proton collisions have been studied. The resulting angular and momentum correlations indicate a possible contribution from other mechanisms of $b\bar{b}$ production than the *flavour creation*, mainly the *gluon splitting*.

Streszczenie

Poszukiwanie łamania liczby barionowej i leptonowej w rozpadach ciężkich barionów oraz badanie tła dla poszukiwań długożyciowych cząstek egzotycznych

W rozprawie doktorskiej przedstawiono wyniki poszukiwań rozpadu $X_b \to K^-\mu^+$ ($X_b = \Lambda_b, \Xi_b^0$) łamiącego zachowanie liczby barionowej i leptonowej. Badania przeprowadzono w ramach współpracy LHC*b* przy użyciu próbki danych odpowiadającej scałkowanej świetlności 3.0 fb^{-1}, zebranej w zderzeniach proton-proton przy energii w układzie środka masy wynoszącej 7 TeV (8 TeV), dla okresu zbierania danych odpowiednio w roku 2011 (2012). Nie zaobserwowano znaczącego statystycznie sygnału pochodzącego od badanego rozpadu. Wyznaczono górną granicę częstości jego występowania jako $\mathcal{B}(\Lambda_b \to K^-\mu^+) < 3.6 \times 10^{-9}$ oraz $\mathcal{B}(\Xi_b^0 \to K^-\mu^+) < 1.8 \times 10^{-8}$ na poziomie ufności wynoszącym 95%.

W rozprawie przedstawiono również badania tła dla poszukiwań długożyciowych cząstek egzotycznych. Opisano pomiar przekrojów czynnych na produkcję par $b\bar{b}$ i $c\bar{c}$ z użyciem inkluzywnych hadronów pięknych (powabnych) w stanie końcowym, przy wykorzystaniu próbki danych zebranej w eksperymencie LHC*b* w roku 2010 w zderzeniach proton-proton przy energii w układzie środka masy wynoszącej 7 TeV. Autor niniejszej dysertacji opracował interfejs do symulacji przypadków z użyciem wyższych rzędów rachunku zaburzeń w oparciu o metodę POWHEG. Przedstawiono charakterystyki kinematyczne dla produkcji hadronów w zderzeniach proton-proton. Widoczne korelacje kątowe oraz pędowe podkreślają możliwe dodatkowe przyczynki do produkcji $b\bar{b}$, głównie od procesów typu rozszepienie gluonu (ang. *gluon splitting*).

Acknowledgements

This thesis was funded by the Henryk Niewodniczański Institute of Nuclear Physics Polish Academy of Sciences. The Author of this thesis was granted the KNOW scholarship and financial support within the framework of the project "Doctus - Lesser Poland scholarships for PhD candidates" co-financed by the European Union under the European Social Fund.

I would like to express my gratefulness to all the persons who have made possible and memorable the five years of my PhD.

First, I would like to thank my primary supervisor Prof. Tadeusz Lesiak for his help and guidance throughout these five years. At anytime, even under difficult circumstances, you have always found a way to motivate me.

I would also like to thank my second supervisor Assoc. Prof. Marcin Kucharczyk. It was you that introduced me to work with the LHC*b* issues. Thanks also to both of you for reading many times each chapter of this thesis. Both your constructive comments helped me to learn from the assignment.

In addition, I am grateful to Prof. Mariusz Witek for the opportunity to work in the LHC*b* collaboration. Thanks to all of you for giving me the advantage to be part of the Experimental Particle Physics Group of the Institute.

I would like to thank Dr Marcin Chrząszcz for his guidance in my physics analysis. My thanks also go to Prof. Clara Mateuzzi for her support I received during the collaborative work I undertook with her.

This PhD study would not have been possible without all our LHC and LHC*b* collaborators who over the years have contributed to setting up the experimental environment. Special thanks also go to the LHC*b* Rare Decays Working Group conveners for the opportunity to perform my physics analysis.

Contents

Chapter 1

Introduction

The Standard Model (SM) of particle physics describes the fundamental particles and their interactions. It was formulated in the 1960-1970s, and since then this theory has been remarkably successful at predicting the behaviour of elementary particles, including the discovery of the Higgs boson. However, there are several phenomena reflected in experimental observations that cannot be explained by the Standard Model. Its limitations have led to extensive studies of extended theories, commonly labelled as the physics Beyond the Standard Model (BSM).

The conservation of baryon and lepton numbers has been checked up to a high precision. The stability of ordinary matter is attributed to the conservation of baryon number, as it ensures that the basic building block of an atomic nucleus, the proton, does not decay. The half-life of the proton is estimated to exceed about 10^{34} years. However, some theories postulate that the baryon number is only an approximate symmetry. If confirmed, it would have a profound impact on our understanding of the evolution of the Universe, both in its early history and its late-time future. Baryon number violation (BNV) is an essential ingredient in the creation of an asymmetry between matter and antimatter observed in the present Universe.

The studies performed in this thesis are devoted to the search for the lepton and baryon number violating decay $X_b \to K^- \mu^+$ ($X_b = \Lambda_b, \Xi_b^0$)[1] and have been performed in a model independent way within the LHC*b* collaboration. That kind of search has a strong motivation owing to the fact that we observe a strong matter-antimatter asymmetry in our Universe which can be explained by the existence of processes that violate the baryon number in combination with a CP violation. The presented search for baryon- and lepton-number violating decays of heavy baryons provides a way to constrain couplings of such interactions to the beauty quark. The violation of baryon number is expected to happen in a vast category of BSM models. In particular the R-parity non-conservation can be considered. Here, the studies of such models interplay with searches for exotic particles decaying into Standard Model particles.

The experimental signature of massive long-lived exotic particles production are displaced vertices related to quarks that these particles are decaying into. However, similar signature may also originate from heavy quarks produced in the Standard Model processes like *e.g.* $pp \to b\bar{b}X$. Hence, for the

[1] Throughout this thesis, whenever a decay mode is given, the charge conjugate is also implied.

exotica related searches, an important issue is to explore and understand the above mentioned Standard Model background. This dissertation, among others dedicated to the measurement of $b\bar{b}$ and $c\bar{c}$ production cross sections with inclusive final states, incorporates more detailed background characteristics. For this purpose an additional Monte Carlo generator, the so-called POWHEG-BOX, has been incorporated into the framework of the LHC*b* software by the Author of this dissertation. This made it possible to handle Next-to-Leading Order (NLO) accuracy for the $b\bar{b}$ production cross section within LHC*b* event simulation.

The dissertation is organized as follows: Chapter 2 describes the theoretical foundations of the Standard Model as well as the BSM models. In addition, it provides a description of the basic idea behind NLO calculations and MC event generators.

Chapter 3 introduces previous experimental results, including constraints on BNV and LNV and $\sigma(b\bar{b})$ measurements in hadronic collisions.

Chapter 4 describes the experimental apparatus of the LHC*b* detector. Special attention is given to subdetectors that are of particular importance to this analysis.

The results of data analysis in search for the decay $X_b \to K^-\mu^+$ are presented in Chapter 5. First, the chapter discusses the event selection requirements and signal classification. Next, a calibration of the multivariate classifier responses to the data together with the optimization of the full selection are described. In the following parts of this chapter the studies on control channels handling MC/data discrepancies and the verification of the signal selection are discussed. Finally, the background estimation is performed and in view of the lack of observation of the decay in question, a limit on the respective branching fraction is computed, being normalized to the decay with a known branching fraction.

Chapter 6 describes the background studies for exotic decays. First, it describes the work performed by the Author which includes the implementation of the new Monte Carlo generator into the LHC*b* software chain. Hereby MC event production has been performed using the POWHEG method. Next, the measurement of $\sigma(b\bar{b})$ and $\sigma(c\bar{c})$ cross-section with inclusive final states is described, which is based on the PYTHIA and POWHEG event productions. An essential part of the work described in this chapter is devoted to compare the characteristics of the generated b-hadrons and reconstructed b–hadron secondary vertices between PYTHIA and POWHEG simulations.

Chapter 2

Theoretical introduction

The story of physics is, to a large extent, the pursue of fundamental constituents of matter. Nowadays, this search is both experimentally and theoretically challenging. However, the success can arise from a succession of pioneering experiments that would provide crucial hints for the theorists. Throughout the twentieth century, the development of new sophisticated detectors and accelerators in parallel with breakthrough theoretical ideas in quantum field theories has led to the establishment of viable theories of electromagnetism as well as weak and strong forces.

This thesis is based on the experimental data which were collected during the so-called *Run 1* period of the LHC operation, when the discovery of the Higgs boson completed the evidence for the Standard Model. It is motivated by the fact that, in spite of overwhelming success of the SM, this theory exhibits clear shortcomings. As a result, a vast category of new theoretical models, labelled generally as New Physics, has been proposed. Most of these theories predict new processes, in particular those occurring with the violation of the lepton and baryon number. This work aims at providing experimental constraints on one category of the above mentioned processes, encompassing the beauty baryon decays. In addition, this work refers to the search for exotic particles using LHCb data. In some of the models the exotic particles have non-zero lifetime and, decaying to the quark pairs, form displaced vertices. Hence, the studies of backgrounds to these processes are of key importance.

The structure of this chapter is the following. First, a very brief description of the Standard Model is given. Next, the New Physics theories which are of particular relevance for this study are briefly reviewed. Special attention is paid to the Minimal Supersymmetric Standard Model. Finally, the calculation of the $b\bar{b}$ production cross section is discussed, including its implementation within MC event generators.

2.1 Standard Model of particle physics

The Standard Model of particle physics is a gauge quantum field theory (QFT) that specifies what are, at the current level of human knowledge, the basic particles and how they interact [1]. These fundamental blocks are fermions of spin 1/2. The pattern of elementary fermions repeats itself three times in the form of the so-called *generations*. Experimentally, three generations have been observed. The forces (electromagnetic, weak and strong) act among building

blocks via exchange of the respective spin-one bosons. The fourth force of nature, gravity, is so weak as to be negligible as far as the SM is concerned.

The main quantum numbers, such as electric charge (Q), total angular momentum (J) and parity (P) are listed in Tab.2.1 and 2.2 for quarks and leptons, respectively. The same information about gauge bosons is collected in Tab.2.3.

The lepton number $\mathcal{L}$ is defined as a quantum number with value $+1$ for leptons, -1 for anti-leptons and 0 for all other particles. In addition, leptonic flavour quantum numbers are defined, each associated to the individual lepton family. These flavour quantum numbers, denoted as $\mathcal{L}_f$, $f = e, \mu, \tau$, determine the *total lepton number*, which is the sum of three lepton flavour numbers $\mathcal{L}_{TOT} = \mathcal{L}_e + \mathcal{L}_\mu + \mathcal{L}_\tau$.

Quarks carry also an additional quantum number, the baryonic one $\mathcal{B} = 1/3$ (and $\mathcal{B} = -1/3$ for anti-quarks). All others particles (*e.g.* leptons, gauge bosons, *etc.*) have $\mathcal{B} = 0$. Thus, all baryons (anti-baryons), which are composed of three quarks (anti-quarks), are characterized by $\mathcal{B} = 1$ ($\mathcal{B} = -1$), respectively.

TABLE 2.1: Characteristics of quarks [1].

Generation	Name	$Q/\lvert e\rvert$	$I(J^P)$	Mass [MeV/c^2]
1st	u (up)	$+\frac{2}{3}$	$\frac{1}{2}(\frac{1}{2}^+)$	$2.3^{+0.7}_{-0.5}$
	d (down)	$-\frac{1}{3}$	$\frac{1}{2}(\frac{1}{2}^+)$	$4.8^{+0.5}_{-0.3}$
2nd	c (charm)	$+\frac{2}{3}$	$0(\frac{1}{2}^+)$	$1,275 \pm 25$
	s (strange)	$-\frac{1}{3}$	$0(\frac{1}{2}^+)$	95 ± 5
3rd	t (top)	$+\frac{2}{3}$	$0(\frac{1}{2}^+)$	$173,210 \pm 510 \pm 710$
	b (bottom)	$-\frac{1}{3}$	$0(\frac{1}{2}^+)$	$4,180 \pm 30$

TABLE 2.2: Characteristics of leptons [1].

Generation	Name	$Q/\lvert e\rvert$	J^P	Mass [MeV/c^2]
1st	e (electron)	-1	$\frac{1}{2}^+$	$0.510998928 \pm 0.000000011$
	ν_e	0	$\frac{1}{2}$	0^{SM}
2nd	μ (muon)	-1	$\frac{1}{2}^+$	$105.6583715 \pm 0.0000035$
	ν_μ	0	$\frac{1}{2}$	0^{SM}
3rd	τ (tau)	-1	$\frac{1}{2}^+$	1776.86 ± 0.12
	ν_τ	0	$\frac{1}{2}$	0^{SM}

Superscript "SM" stands for Standard Model expectation.

TABLE 2.3: Characteristics of gauge bosons [1].

Force	Name	$Q/\|e\|$	J^P	Mass [GeV/c^2]
Electromagnetic	γ (photon)	0	1^-	0
Weak	$W^\pm$	± 1	1	80.385 ± 0.015
	Z^0	0	1	91.1876 ± 0.0021
Strong	g (gluon)	0	1^-	0
	H^0 (Higgs)	0	0	$125.09 \pm 0.21 \pm 0.11$

The strength of individual fundamental interactions is characterized by the dimensionless gauge coupling parameters. The one which characterizes the electromagnetic force, the so-called *fine structure constant*, amounts to $\alpha \approx 1/137$. The value of the respective coupling corresponding to strong interaction is much larger than α. As for quark and gluon interactions, at high energies the strong interaction coupling constant takes values close to one. Finally, the large mass of the associated intermediate boson induces the value of the weak coupling constant, which is much smaller in comparison with the electromagnetic one. While typically labelled as *constants*, actually all these coupling strengths vary as a function of the energy scale or momentum transfer of the particular process looked at, as will be discussed later. This justifies the more appropriate name "running coupling constants".

The general properties of the SM originate from the symmetries which are captured mathematically in terms of the corresponding group structure given as $SU(3)_C \times SU(2)_L \times U(1)_Y$[2]. Here the subscripts C, L and Y correspond to the colour, weak isospin and hypercharge quantum numbers, respectively.

The electromagnetism is associated with the abelian symmetry group $U(1)$ and described by the quantum field theory called quantum electrodynamics (QED). According to QED, all electromagnetic phenomena, in particular the interaction of light with matter and those occurring between charged particles, are realized via exchange of photons.

The weak interaction is, in particular, responsible for the β decay. The key physical invariance is the lack of distinction between the neutrino and the electron - it only "sees" a generic lepton (within a single generation). All particles have a property called *weak isospin*, which plays a role of charge of the weak interaction. Mathematically, the above mentioned invariance of the weak isospin corresponds to the non-abelian $SU(2)_L$ symmetry group. The subscript "L" denotes the weak isospin coupling to left-handed fermions only. The weak interaction involves the exchange of the intermediate vector bosons, charged $W^\pm$ and neutral Z^0. Since these weak force mediators have non-zero mass, ($80(91)$ GeV/c^2 for the W (Z^0), respectively), the uncertainty principle dictates an interaction range of $\mathcal{O}(10^{-18}\mathrm{m})$, which is about 1 ‰ of the diameter of a proton. The weak field quanta couple to both quarks and leptons. An interaction mediated by $W^\pm$ bosons is called a Charged Current (CC), whereas when the Z^0 is involved, it is called a Neutral Current (NC) process.

[2] $\times$ - a direct product of two groups.

The gauge theory based on the non-abelian $SU(3)_C$ group, quantum chromodynamics (QCD), postulates quarks as the basic entities and the ultimate constituents of hadrons (the bound states composed either of three quarks (baryons) or a quark-antiquark pair (mesons)). The associated eight gauge bosons are called gluons. The subscript "C" in the group's name represents the *colour charge* quantum number of gluons and quarks - the QCD analogue of electric charge and weak isospin. The colour charge takes three values labelled as red, blue and green, together with the respective anti-colours attributed to antiquarks. Owing to the fact that gluons themselves have a colour charge, they self-interact. This leads to the *confinement* phenomenon, which means that the quarks are not observable in the nature as free particles and are hidden inside colourless bound states of hadrons.

The strong interaction is the strongest of the four fundamental forces. At distances comparable to the diameter of a proton, the strong interaction between quarks is about 100 times greater than the electromagnetic one. At smaller distances, however, the strong force between quarks becomes weaker, and the quarks begin to behave almost like independent particles, an effect known as *asymptotic freedom*.

Although weak and electromagnetic interactions appear very different at low energies, they do share some common features. Both kinds of interactions affect leptons and hadrons, both are mediated by particles carrying unit spin and negative parity, and both have their own universal coupling constant that governs the strength of the interactions. As follows, at extremely high temperatures, such as those found in the early Universe, corresponding to the energy scale of $100\ \mathrm{GeV}$, these two forces are modelled as two different aspects of the same interaction. Above this unification energy, they merge into a single electroweak force described by the direct product of the $SU(2)$ group related to the weak isospin interactions and the $U(1)$ group of electromagnetism. Such a unified electroweak theory is known as the Glashow-Salam-Weinberg (GSW) model [2, 3, 4]. This model has been proved to be renormalizable by 't Hooft and Veltman [5].

The bosons carrying the electroweak force ($W^{\pm}$, Z^0 and γ) should be massless as a consequence of the underlying gauge symmetry. A theoretical mechanism, according to which the $W^{\pm}$ and Z^0 acquire mass while the photon remains massless, was proposed in 1964 [6, 7] and named the *Higgs mechanism*. Its essence is the postulate of the existence of a new scalar, complex quantum field (the Higgs field) that permeates all space. The potential associated with the Higgs field keeps the full lagrangian of electroweak interaction renormalizable and invariant under the $SU(2)_L \times U(1)_Y$ symmetry group, while the perturbations around the vacuum (the minimum of the potential) do not preserve the symmetry. This spontaneous breaking of the local gauge symmetry is called the Higgs mechanism. In terms of group theory it leads to the breakdown of the symmetry $SU(2)_L \times U(1)_Y \to U(1)_Q$, where the subscript Q denotes the electric charge.

The Higgs field comprises a complex $SU(2)$ doublet consisting of four real fields. A massless gauge boson, such as the photon, has two orthogonal spin components transverse to the direction of motion, while massive gauge bosons

have three components, including a longitudinal one. In the electroweak theory, the $W^{\pm}$ and the Z^0 absorb three of the four degrees of freedom of the Higgs field, thereby forming their longitudinal spin components and acquiring mass. The remaining fourth component should be observable as a scalar particle, the Higgs boson.

Masses of fermions are introduced in the SM by adding to the Lagrangian a new $SU(2)_L \times U(1)_Y$ invariant term which describes the coupling of the Higgs doublet to the fermion fields (the so-called Yukawa couplings).

The particle with properties compatible to the Higgs boson [6, 7] was discovered in 2012 by the ATLAS [8] and CMS [9] experiments. Nowadays, the ATLAS and CMS collaborations are taking physics data for *Run 2*, which will allow them to study this new state in depth.

Nevertheless, there are still several questions that remain unanswered by the SM, such as why the nature prefers matter over antimatter, and what is the composition of dark matter and dark energy. The limitations of the SM are discussed further in the next section.

In spite of extensive searches, up to now there is no evidence neither for lepton nor baryon number violation. Thus, only upper limits on the branching ratios for the $\mathcal{B}$ and/or $\mathcal{L}$ violating decays are provided. The main problem in searches for rare phenomena is the identification and drastic reduction of the background sources. This is described in detail in the chapter dedicated to the study of the decay of heavy baryons $X_b \to K^- \mu^+$ ($X_b = \Lambda_b, \Xi_b$) in a model independent way. The processes in question violate both the baryon and lepton number, but conserve the difference $\mathcal{B}$–$\mathcal{L}$.

The SM allows for the violation of the lepton and baryon number only at the negligible level (typically of the order of 10^{-50}) owing to high-order virtual effects. The observation of neutrino oscillations has proved that neutrinos possess mass, thus yielding the first experimental evidence that the SM is incomplete. Moreover, it has provided indisputable evidence that the separate lepton flavour is not conserved, though the conservation of a total lepton number is still an open question.

2.2 Limitations and extensions of the Standard Model

At the current level of knowledge the SM offers the best description of the known fundamental particles and the forces that govern them. Its predictions are in good overall agreement with experimental results, reaching for some observations the precision of the permil level. However, as it has been already mentioned, there are observed phenomena which necessitate extension of the SM. Giving an example of the neutrino oscillations, to accommodate them in SM at least nine more parameters must be introduced, in addition to the 19 arbitrary parameters which the SM already contains. Additionally, there are also several fundamental questions which are not addressed properly, or even at all, in the Standard Model.

Among them is the fact that the SM does not include gravity, one of the four fundamental forces. The model also fails to explain why the gravity is so much weaker in comparison with the remaining three forces. This huge difference in the strength of fundamental forces is one aspect of the *hierarchy problem* [1].

The hierarchy problem also refers to the wide range of masses of elementary particles. In the table shown in the previous section, the significant differences in the mass of leptons and quarks may be seen. In addition, the hierarchy problem is also related to the Higgs boson mass, where the requirements on the maximum allowed value of the Higgs boson mass from precision measurements on weak interactions are of the order of $100\,\mathrm{GeV}/c^2$, which is in agreement with the observed Higgs mass of $\sim 126\ \mathrm{GeV}/c^2$. However, if the SM is valid up to the Planck scale of $\sim 10^{19}\ \mathrm{GeV}$, loop corrections in the self-coupling of the Higgs would drive the mass towards very high values [10]. Thus, very uncomfortable degree of fine-tuning is needed to cancel the loop corrections to achieve the observed Higgs mass, considering only the SM particles.

Another problem of the SM is the fact that it does not describe the observed matter-antimatter asymmetry, usually called baryon asymmetry, which comprises one of the greatest mysteries of the universe. Baryogenesis is a dynamical creation of a baryon asymmetry from an initially baryon-symmetric universe. It can be explained by the existence of decays that violate the baryon number in combination with a CP violation in these decays and the departure from thermodynamical equilibrium. These three requirements are usually called Sakharov's conditions [11]. The SM provides the relevant processes to satisfy Sakharov's conditions. However, they lead to the matter-antimatter asymmetry which is approximately ten orders of magnitudes too weak as compared with experimental observations (in particular those from the cosmic microwave background and from nucleosynthesis).

Last but not least, cosmological observations encapsulated in the so-called *concordance model*[3] have shown that the SM particles contribute to $\approx 4.6\%$ of the total energy density, with the remaining $\approx 22.9\%$ in the form of *dark matter* and another $\approx 72.5\%$ in the form of *dark energy* [12]. Dark matter can interact with the SM particles only via weak force and manifests itself mainly through gravitational effects. Among all the particles contained in the SM, none has the properties of dark matter (apart from a possible small admixture of neutrinos and population of black holes similar to those detected recently by the LIGO experiment[4]). Consequently, the SM does not provide a viable dark matter candidate. Theorists have turned to extensions of the SM of particle physics in the search for dark matter candidates, mainly in the form of weakly interacting massive particles (WIMPs) [1].

The list of limitations of the SM allows to assume naturally that there is a low-energy limit of more fundamental theory [15]. In addition, there is an evidence that the strengths of the fundamental forces vary with energy in

[3] The *concordance model* refers to the SM of cosmology with the specified contributions of different types of matter.

[4] LIGO's discovery [13] of a gravitational wave from two merging black holes of similar masses rekindled suggestions that primordial black holes make up the dark matter [14].

such a way that they converge to a single value at a certain high-energy scale of the order of 10^{16} GeV. This fact has allowed physicists to develop in the late 1970s the so-called Grand Unification Theories (GUT) [16], *i.e.* an idea that the strong, weak and electromagnetic forces can be unified in a field theory with a single coupling constant and a single gauge symmetry group, providing more degrees of freedom as compared with the SM structure. Below the GUT energy scale, the theory breaks down to the familiar SM structure through spontaneous symmetry breaking. However, it has been proved that the strengths of the forces do not converge exactly unless new effects come into play at higher energies. In particular the convergence of couplings is reasonably precise in the framework of the so-called *supersymmetry* (SUSY), which may be seen in Fig.2.1. This dissertation refers to theoretical models arising from SUSY, which, in particular, provide estimate for the presence of exotic decays which violate the baryon and lepton number.

The underlying idea of SUSY is the restoration of symmetry between fermions and bosons [17]. The irreducible representations of the SUSY algebra are called *supermultiplets*. Each of them contains the same number of fermionic and bosonic degrees of freedom, which are commonly called *superpartners* of SM particles. Thus, SUSY requires that each of the known fundamental particles is paired with a superpartner with a spin different by 1/2. In this way, the new supersymmetric partners (spartners) for all known SM particles are introduced: quark $\rightarrow$ squark, lepton $\rightarrow$ slepton, photon $\rightarrow$ photino, Z $\rightarrow$ Zino, W $\rightarrow$ Wino, gluon $\rightarrow$ gluino, Higgs $\rightarrow$ Higgsino. There is a generic nomenclature to append a postfix "ino" for a spin 1/2 superpartner, while for the scalar spin-0 superpartner a prefix "s" is applied: squarks, sleptons, stau, sbottom, *etc.* However, no supersymmetric particle has been observed to date. It is believed that this is because supersymmetry is a broken symmetry, and as a result the superpartners are much heavier than the known elementary particles.

The SUSY theory provides a natural solution to the hierarchy problem by introducing additional loop corrections to the Higgs mass. Since the set of particles is doubled, the loop corrections to the Higgs mass coming from a given SM particle are almost exactly cancelled by the respective contributions from the superpartners (bosonic and fermionic loops yield opposite signs here).

The GUT models generally provide new processes leading to the violation of the baryon and lepton number (the fact of paramount importance for this thesis).

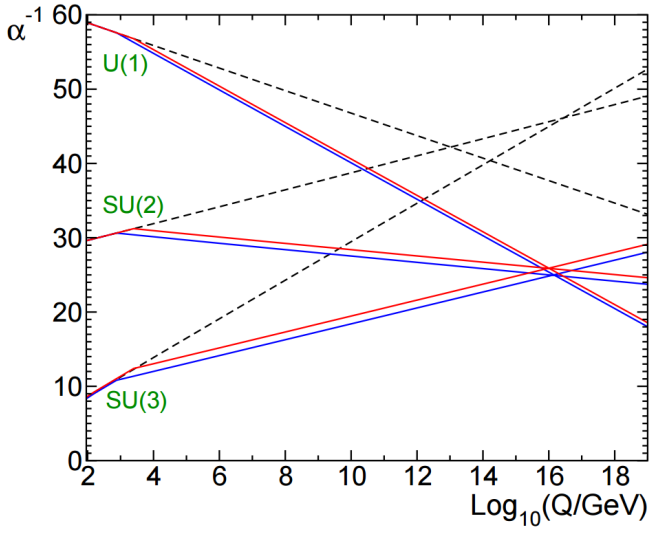

FIGURE 2.1: Evolution of the inverse of the three coupling constants in the SM (dashed lines) and in the supersymmetric extension of the SM (solid lines). Figure adopted from [17].

In view of the above facts the so-called R-parity has been introduced. Its conservation (or violation) is closely related the conservation (or violation) of baryon and lepton numbers, $\mathcal{B}$ and $\mathcal{L}$. The R-parity quantum number is defined as:

$$P_R = (-1)^{3(\mathcal{B}-\mathcal{L})+2S}, \tag{2.1}$$

where $\mathcal{B}$, $\mathcal{L}$ and S stand for baryon, lepton and spin of the field, respectively. All of the SM particles have even R-parity ($P_R = +1$), while all of the super-particles have odd R-parity ($P_R = -1$).

Most of SUSY models assume R–parity conservation which implies that superparticles and super antiparticles must be produced in pairs. Owing to the R–parity conservation, the lightest superpartner (LSP) is expected to be stable and must eventually be produced at the end of a decay chain initiated by the decay of a heavy unstable supersymmetric particle. Depending on the mass and production cross section the LSP could be a good candidate for dark matter (see Sect.2.2.2).

It is also possible that R-parity is replaced by some alternative discrete symmetry to protect R-parity conservation. One particularly attractive way in which this could occur is the scenario in which B–L is a continuous gauge symmetry that is spontaneously broken (since there is no corresponding massless vector boson) at some very high energy scale. If a unique gauged $U(1)_{B-L}$ symmetry is only broken by the scalar vacuum expectation value (VEV) that carries even integer values of $3(B$–$L)$, then P_R automatically survives as an exactly conserved discrete remnant subgroup. A variety of extensions of the MSSM with exact R-parity conservation have been proposed even recently (see for example [18, 19]).

The breakdown of the R–parity symmetry can be achieved either through BNV or through LNV. In this case, the LSP is no longer required to be stable and it is allowed to decay into ordinary particles. The present SUSY searches for

R-parity violation (RPV) rely mostly on signatures such as *missing energy* due to the LSP escaping the detectors. These studies have not revealed any hints of signals yet. The decay of the LSP would eliminate missing energy signatures in events with supersymmetric particles. Then, depending on the amount of the violation, the LSP acquires a certain lifetime and leaves a displaced vertex signature [20] (see Sect.2.2.2).

In the case of the R-parity violation caused by LNV, the allowed amount of LNV is constrained by the neutrino masses, and by limits on rare processes such as $\mu^- \to e^- e^+ e^-$. However, an interesting scenario is that of SUSY models with R–parity violation and baryon number violation that have a significant range of parameter space in which the Higgs dominantly decays to six quarks, creating a displaced vertex signature [21].

2.2.1 Minimal Supersymmetric Standard Model

The Minimal Supersymmetric Standard Model (MSSM) is the simplest possible supersymmetric extension of the SM of particle physics [22]. In this model the single particle states of the SM are extended to form supermultiplets that contain both fermionic and bosonic states. It has the gauge group $SU(3)_C \times SU_L(2) \times U(1)_Y$, consisting of three gauge superfields and seven left-handed chiral superfields, leading to the sparticles summarized in Tab.2.4.

An important feature of the MSSM is that the superpartners listed are not necessarily the mass eigenstates of the theory. This comes from taking into account the effects of electroweak symmetry breaking and supersymmetry breaking. Accordingly, there can be a mixing between the electroweak gauginos and the higgsinos, and within the various sets of squarks and sleptons, as well as the Higgs scalars sharing the same electric charge. After electroweak symmetry breaking, the W^0, B^0 gauge eigenstates mix to give mass eigenstates Z^0 and γ, and so do their SUSY counterparts $\widetilde{W}$, $\widetilde{B}$, to give zino $\widetilde{Z^0}$ and the photino $\widetilde{\gamma}$. The charginos and neutralinos are the mass eigenstates of the $\widetilde{W^\pm}$ and $\widetilde{H^\pm}$ fields, respectively.

TABLE 2.4: Fundamental particles of the MSSM to be added to the already discovered particles of the SM.

Particle	Spin	P_R	Mass eigenstates	Gauge eigenstates
Higgs bosons	0	$+1$	h^0, H^0, A^0, $H^\pm$	H_u^0, H_d^0, H_u^+, H_d^-
squarks	0	-1	$\widetilde{u_L}$, $\widetilde{u_R}$, $\widetilde{d_L}$, $\widetilde{d_R}$	$\widetilde{u_L}$, $\widetilde{u_R}$, $\widetilde{d_L}$, $\widetilde{d_R}$
			$\widetilde{s_L}$, $\widetilde{s_R}$, $\widetilde{c_L}$, $\widetilde{c_R}$	$\widetilde{s_L}$, $\widetilde{s_R}$, $\widetilde{c_L}$, $\widetilde{c_R}$
			$\widetilde{t_1}$, $\widetilde{t_2}$, $\widetilde{b_1}$, $\widetilde{b_2}$	$\widetilde{t_L}$, $\widetilde{t_R}$, $\widetilde{b_L}$, $\widetilde{b_R}$
sleptons	0	-1	$\widetilde{e_L}$, $\widetilde{e_R}$, $\widetilde{\nu_e}$	$\widetilde{e_L}$, $\widetilde{e_R}$, $\widetilde{\nu_e}$
			$\widetilde{\mu_L}$, $\widetilde{\mu_R}$, $\widetilde{\nu_\mu}$	$\widetilde{\mu_L}$, $\widetilde{\mu_R}$, $\widetilde{\nu_\mu}$
			$\widetilde{\tau_L}$, $\widetilde{\tau_R}$, $\widetilde{\nu_\tau}$	$\widetilde{\tau_L}$, $\widetilde{\tau_R}$, $\widetilde{\nu_\tau}$
neutralinos	$1/2$	-1	$\widetilde{\chi}_1^0$, $\widetilde{\chi}_2^0$, $\widetilde{\chi}_3^0$, $\widetilde{\chi}_4^0$	$\widetilde{B}^0$, $\widetilde{W}^0$, $\widetilde{H}_u^0$, $\widetilde{H}_d^0$
charginos	$1/2$	-1	$\widetilde{\chi}_1^\pm$, $\widetilde{\chi}_2^\pm$	$\widetilde{W}^\pm$, $\widetilde{H}_u^+$, $\widetilde{H}_d^-$
gluinos	$1/2$	-1	$\widetilde{g}$	$\widetilde{g}$
gravitino/goldstino	$3/2$	-1	$\widetilde{G}$	$\widetilde{G}$

SUSY is a spontaneously broken symmetry in the same manner as the SM, *i.e.* by means of the Higgs mechanism. Owing to the fact that the MSSM uses only left-handed superfields, the Higgs sector of the MSSM is composed of two hypercharge ($Y = \pm 1$) Higgs doublets which generate masses for up-type and down-type quarks and charged leptons. This leads to five Higgs bosons, *i.e.* a charged pair $H^\pm$, a CP–odd neutral boson A^0, two neutral CP–even bosons h^0, and two VEV, V_u and V_d. As follows, the tree-level Higgs sector parameters depend on the ratio between the two Higgs VEV's (tan$\beta = V_u/V_d$) and the mass of the A^0 boson. In addition, the SUSY breaking terms are consistent with the low-energy breaking of SUSY. In other words there must be soft terms, in the sense that the residual one-loop correction is maintained small.

Even though the general MSSM has 124 free parameters, most of them can be tightly constrained by requiring the model consistency within the present experimental bounds. For example, one interesting feature of the minimal super-gravity model (mSUGRA) is the LSP with macroscopic decay length large enough to be detected in a state-of-art particle detector.

2.2.2 mSUGRA with R-parity violation

So far, there is no realistic model of spontaneously-broken low-energy SUSY, where the supersymmetry breaking arises exclusively as a consequence of the interactions of the particles of the MSSM. An alternative scheme assumes a theory consisting of at least two distinct sectors: a *hidden* sector composed from particles that are completely neutral with respect to the SM gauge group, and a *visible* sector consisting of the particles of the MSSM.

Supersymmetry breaking is assumed to originate in the hidden sector, and its effects are transmitted to the MSSM by some mechanism involving the mediation by particles that comprise an additional *messenger* sector. One theoretical scenario that exhibits this structure is a gravity mediated supersymmetry breaking, which has received the name of *supergravity* models. In this

case, the mediating interactions are of gravitational nature, where gravity enters at the Planck scale. The spontaneous breaking of global supersymmetry implies the existence of a massless Weyl fermion, the goldstino. It unifies the space time symmetries of ordinary general relativity with local supersymmetry transformations and the spin-2 graviton is assigned to the spin 3/2 fermion superpartner named gravitino. Once supersymmetry is spontaneously broken, the gravitino acquires a mass by absorbing the goldstino. This scenario, called the super-Higgs mechanism, is entirely analogous to the ordinary Higgs mechanism.

The most popular and developed recently are the minimal super-gravity models (mSUGRA) [21]. This kind of models assume the universality of the gaugino and sfermion masses at a high energy scale. In addition, they always have an extra scalar mass parameter m_0^2, which needs to be fine tuned. In this way the sparticle exchange does not generate flavour changing neutral current effects at an unacceptable level. mSUGRA naturally generates the soft SUSY breaking terms which are the consequence of the super-Higgs effect. It is one of the most widely investigated models of particle physics, which is due to its large predictive power, requiring only four input parameters and a sign to determine the low energy phenomenology from the scale of GUT.

The mSUGRA framework incorporates the breaking of the R-parity symmetry that would result in BNV and/or LNV processes and might lead to metastable particles. In the event that R-parity violation is caused by BNV, the neutralino decays are purely hadronic. Such decays into three quarks give rise to three jets with a total invariant mass equal to that of the original sparticle [23]. The decay length is mainly fixed by the BNV couplings λ". A lifetime of $10\ \mathrm{ps}$, which is compatible with limits on λ", results in the lightest neutralino $\widetilde{\chi}_1^0$ decaying well inside the LHC*b* vertex detector (see Sect.4.2.1.1). The production of $\widetilde{\chi}_1^0$ happens in pairs through the decay of a Higgs boson h^0. If the parameter defining the Higgs couplings, tan(β) is small (typically < 3), the SUSY h^0 is essentially equivalent to the SM Higgs, with an expected production cross-section of about 20 pb at 7 TeV proton-proton collisions, as suggested in [24].

In the case of mSUGRA scenarios with explicit RPV via BNV proposed in [21], a study at LHC*b* has been already performed [25]. This search for SUSY, via vertices displaced from the beam axis and a primary vertex, considered pure hadronic neutralino decays $\widetilde{\chi}_1^0 \to qqq$. Addressing these experimental searches, the dominant background for the exotic long-lived particles with jets in the final state comes from the inclusive $b\bar{b}$ production. Thus, a precise measurement of the $b\bar{b}$ production cross section is fundamental for this kind of analyses related to new particle searches. In addition, such a measurement is a powerful probe of QCD at very high energies. As a consequence, one of the main themes of the corresponding MC simulation is to strive for an increased accuracy in the description of physical processes participating in a cross section for producing hadrons.

2.3 Calculations of the $b\bar{b}(c\bar{c})$ production cross section

The production of b and c quarks happens predominantly in pairs from quark and gluon scattering. As in the proton-proton collisions at the LHC, the partons from both protons hard scatter, a $b\bar{b}$ and $c\bar{c}$ pairs, are produced.

Free quarks and gluons cannot be directly observed because of the colour confinement – this means that the hadron structure has a nonperturbative nature. Therefore, to relate cross sections for producing quarks and gluons with a cross section for producing hadrons, the QCD factorization theorem is used. Regarding this theorem, the cross section is separated into two parts: the cross section on short-distances, and the universal long-distance functions. The long-distance part features the so-called infrared divergences – singularities caused by gluon emission in the direction of the outgoing parton (collinear divergence), or equivalently, singularities caused by low momentum gluon emission (soft divergence). As follows, the long-distance part is not accessible to perturbative QCD (pQCD) calculations, while the short-distance one is calculable in pQCD. The latter covers the hard scattering (high momentum) process of producing the bottom quarks. An important consequence of the factorization theorem is the fact that the non-perturbative effects can be determined in measurements with simpler experimental environments and theoretically precise predictions and then convoluted to the prediction of the bottom production.

In the pQCD, the b–quark mass m_b acts as an effective low momentum cut-off in this kind of calculation. As $m_b \gg \Lambda_{QCD}$[5], the strong coupling α_s is small ($\alpha_s(m_b) \approx 0.24$) and therefore pQCD works well, so inclusive quantities in strong processes can be computed. The production of b and c quarks has been determined at next-to-leading-order (NLO) in pQCD [26, 27], where the NLO calculations include diagrams up to $\mathcal{O}(\alpha_s^3)$ of the strong coupling constant α_s. The first terms in the perturbation series, which come from quark-antiquark annihilation and gluon-gluon fusion, are of $\mathcal{O}(\alpha_s^2)$, *i.e.* $q\bar{q} \to b\bar{b}$ and $gg \to b\bar{b}$. Such processes are called *flavour creation*. The Feynman diagrams contributing to these processes are shown in Fig.2.2. In addition, b–quarks can be produced in *flavour excitation* processes and *gluon splitting* events. An example of Feynman diagrams for the b quark production at order $\mathcal{O}(\alpha_s^3)$ is shown in Fig.2.3.

In the flavour excitation process, the b quark is considered to be already present in the incoming hadron. It is excited by the exchange of a gluon with the other hadron and appears on mass-shell in the final state. The products of the fragmentation of b and $\bar{b}$ quarks do not need to be back-to-back, as the third parton can carry away some transverse momentum. In the gluon splitting the b quark occurs in $g \to b\bar{b}$ events in the initial- or final-state shower. It is important to stress the fact that within the framework of pQCD, the flavour creation, flavour excitation and gluon splitting have interference terms between them, thus they are not independent. The resulting heavy flavoured final state

[5] $\Lambda_{QCD} \approx 200$ MeV- is the renormalization scale used to set the validity limit of the perturbative approach.

can carry a large combined transverse momentum and thus can be concentrated within a small cone of angular separation.

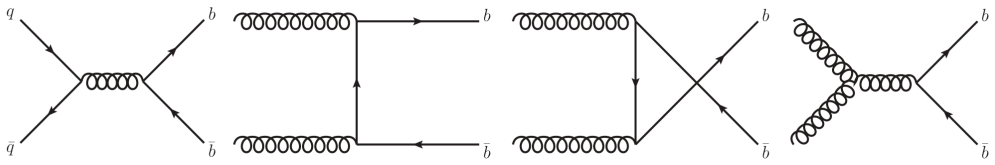

FIGURE 2.2: Lowest-order Feynman diagrams $\mathcal{O}(\alpha_s^2)$ of flavour creation processess: quark-antiquark annihilation $q\bar{q} \to b\bar{b}$ (left) and gluon-gluon fusion $gg \to b\bar{b}$ (three of the most right).

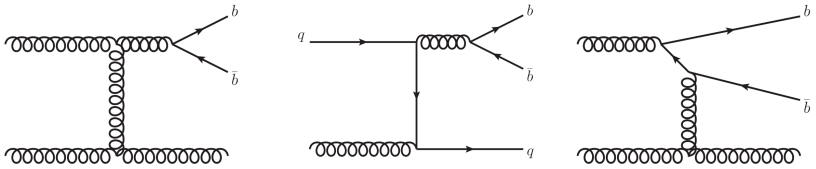

FIGURE 2.3: Examples of NLO Feynman diagrams $\mathcal{O}(\alpha_s^3)$ for $b\bar{b}$ pair production: gluon splitting $gg \to b\bar{b}g$ (left) and $gq \to b\bar{b}q$ (middle), and flavour excitation $gg \to b\bar{b}g$ (right).

LO and NLO contributions to the total cross sections of charm and bottom as a function of centre-of-mass are shown in Fig.2.4. As it may be seen, for charm production there are significant contributions from higher order terms across all energy ranges. Bottom production is less dependent on higher order terms at lower energies. However, as centre-of-mass energies approach the TeV scale, NLO processes become important.

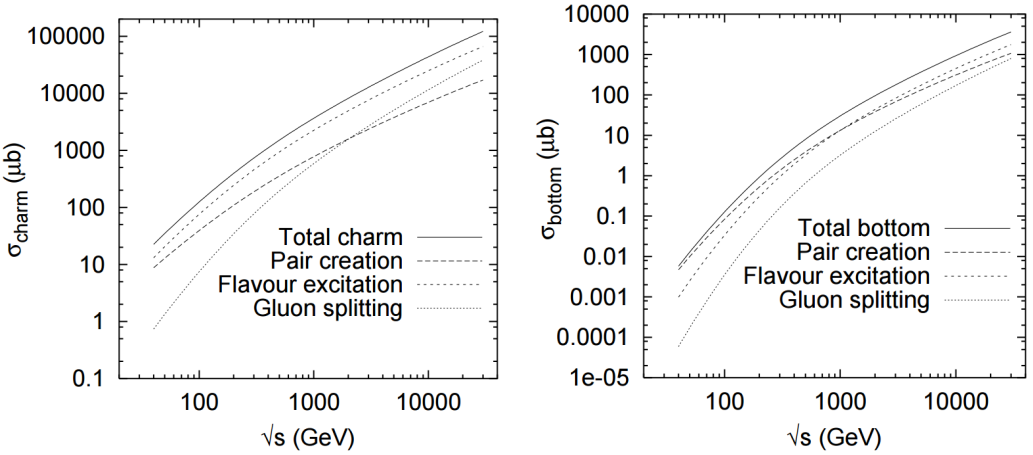

FIGURE 2.4: The total (left) charm and (right) bottom cross sections for pp collisions as a function of a centre-of-mass energy. The contributions from pair creation, flavour excitation and gluon splitting are shown separately. Figure adopted from [28].

Calculations of the parts described above are difficult because of the occurrence of the ultraviolet and infrared divergences. Those divergences

in fixed order calculations with a definite final state have caused an additional puzzle - even if we could perform computations at arbitrary order, one would not be able to give predictions for exclusive quantities. Strictly speaking, tree-level matrix elements cannot be blindly combined with a parton shower (see the next section). The former are inclusive in nature, while the latter produce exclusive final states. The way how these phenomena are handled in the MC event generator is discussed below.

2.3.1 NLO calculations and MC event generators

MC event generators construct outcomes of proton-proton collision in the following main steps: hard process, parton shower, hadronization, underlying event and unstable particle decay [29]. To describe what is observed in a detector as a result of a given process, all outgoing coloured partons must first undergo the parton showering and then must be combined into hadrons, carried by the hadronization phase of the event generator chain.

The basic idea of the parton shower is to describe how quarks and gluons behave at a given momentum scale - how they split (and give extra strongly interacting objects that we see as jets in the final state) and evolve down to energy scale of the order of 1 GeV, associated with infrared cut-off. At the scale below the cut-off, a non pertutbative model of the hadronization process is performed and combined with the previous perturbative treatment employed above this energy level. In particular, to describe events with many hard jets in the final state, one needs to combine tree-level matrix elements for several jet multiplicities simultaneously with parton showers. To perform these combinations the NLO matrix-element/parton-shower merging procedure has been adopted [27]. The goal of this merging procedure is to extend tree-level multi-jet merging methods to NLO accuracy in QCD for every available jet multiplicity. However, this is a nontrivial task since the parton shower MC programs (PSMCP) do implement approximate NLO corrections already. In addition, the kinematics of all hard objects in the event is explicitly represented and it is simply assumed that there is a one-to-one correspondence between hard partons and jets. Such an assumption may cause problems of double counting of some region of the phase space or undercounting others. There is a problem defined by the question: if a NLO matrix element and a Leading Log parton shower is given, how to make sure that there is no double-counting of the first jet? Does it come from the matrix element or the parton shower? In other words, since the PSMCP do include NLO corrections already, as mentioned before, the possibility of having the same kinematical configuration from the parton shower and from the NLO may lead to double counting. To overcome this, one would need to get simultaneously NLO normalization, a good description of hard multi-jet systems, but also match them with a good parton shower of the internal structure of these jets.

The first two methods proposed for including NLO corrections within parton shower algorithms and giving solution to the overcounting problem were MC@NLO [30] and POWHEG [31]. The aim of these methods is to improve the event generation of a basic process in such a way that the NLO accuracy

is reached for inclusive observables, maintaining the leading logarithmic accuracy for the shower approach. Presently, both methods are available for many processes.

The MC@NLO scheme removes from the NLO expressions those terms that are being generated by the parton showers. This is achieved by modifying the subtraction terms of the NLO calculation. An alternative idea is used in POWHEG (the acronym stands for Positive Weight Hardest Emission Generator). Within the POWHEG framework the hardest radiation is generated first, and then the event is fed to general purpose event generator to complete the simulation chain, including showering stage. This solution can be performed since the algorithm does not depend upon a particular parton shower program. Furthermore, in POWHEG the events are produced with positive (constant) weights, while in the MC@NLO formalism it is not guaranteed that the weights of the generated states are defined positive (the exact NLO cross section minus the MC subtraction terms may not be positive). Both methods, MC@NLO and POWHEG are by now well established as mature techniques, and their detailed comparison may be found in [32].

The POWHEG output can be easily interfaced to any modern shower generator that is capable of handling user processes, typically those that comply with the Les Houches (LHE) interface [33]. In particular, once the POWHEG generates first a partonic event at the NLO level with the correct weight in order to not have double counting coming from subsequent radiation, the PYTHIA with the transverse momenta (p_T) ordering can be used. The p_T of the produced radiation works as an upper cut-off for the p_T's of the entire subsequent shower, which is performed with p_T less than the p_T generated by POWHEG.

The POWHEG-BOX program [34, 35] is a framework to implement in practice the theoretical construction of the POWHEG method. This implementation has already been applied to a variety of processes at the LHC. In case of the LHC*b* simulation, the logic of its implementation, performed by the Author of this thesis, is described in Appendix A.0.2. However, there are other implementations of the POWHEG on the market as well. The new version of MADGRAPH framework [36] has been designed to support a full automation and optimization of NLO computations in the SM and beyond via both MC@NLO and POWHEG methodology. Independently, POWHEG has been also included in the HERWIG++ [37] and the SHERPA [38] generators. Besides having implemented several processes in the POWHEG framework, the HERWIG++ includes the implementation of the so-called *truncated showers*, which is needed to recover soft gluon interference when interfacing POWHEG with an angular ordered PSMCP[6]. The SHERPA generator incorporates a partially automated procedure for the implementation of the POWHEG methodology.

It is worth mentioning one additional method of matching NLO QCD with a parton shower in the MC scheme, namely the KRKNLO [39]. It offers a simpler alternative to the MC@NLO and POWHEG methods. However, the overall

[6] In angular ordered PSMCP, a large-angle soft emission is generated first and the hardest emission (*i.e.* highest p_T) happens later. Hence, a special care must be put to transform an angular-ordered shower into a shower where the hardest emission happens first.

simplifications of the KRKNLO method come not completely for free, as it requires using parton distribution functions in a special MC factorization scheme. In addition, it is required that the basic parton shower MC generators provide the NLO with a complete coverage of the hard process phase space (this is not a problem for all modern PSMCPs). However, for the time being, the theoretical construction and implementation of the KRKNLO is relevant for the future developments in the sense that it presents a simplified method of correcting the hard process to the NLO level in combination with the parton shower. Anyway, it may pave the way to the Next-to-Next-to-Leading Order (NNLO) hard process combined with NLO parton shower MC.

Chapter 3

Previous experimental results

3.1 Constraints on BNV and LNV

The baryon number violation has been vigorously searched in several processes over the last few decades. These studies were motivated by GUTs predicting this phenomena, the consequence of which is that a nucleons can have finite, if long, lifetime. A proton decay became the focus of major experimental physics efforts starting in the early 1980s. However, a proton decay has not yet been observed [1]. The most stringent results from the nucleon decay experiments put partial lifetime limits on $p \to \pi^0 e^+$ and $p \to K^+ \overline{\nu}$ decays which read $\tau(p \to \pi^0 e^+) > 1.67 \times 10^{34}$ years [40] and $\tau(p \to K^+ \overline{\nu}) > 1.08 \times 10^{34}$ years [41], respectively. The lack of observation of a proton decay has been used to constrain baryon- and lepton-number violating decays involving higher-generation quarks and leptons [42]. Being inspired by this work , the CLEO [43], BaBar [44] and CLAS [45] experiments performed searches for such decays, all summarized in Tab.3.1.

The CLEO collaboration performed also a unique search for the BNV decays of the D^0 meson [46]. Specifically, they looked for $D^0 \to \overline{p}e^+$ and $D^0 \to pe^-$ and found no evidence of these decays. As a consequence, the results have been interpreted with the branching fraction upper limits for the decays in question.

The BaBar collaboration reported the results of searches for the decays $B^0 \to \Lambda_c^+ \ell^-$, $B^- \to \Lambda \ell^-$ and $B^- \to \overline{\Lambda} \ell^-$, where the lepton is a muon or electron [47]. No significant signal for any of such decay modes has been observed and upper limits are determined at the 90% confidence level.

The CLAS collaboration performed a search for BNV decay modes of Λ hyperons as a direct probe of couplings of BNV interactions to the strange quark [48]. They investigated eight decay modes in which the Λ decays to a charged meson and a charged lepton, conserving charge in all decays. The meson is either a $\pi^\pm$ or $K^\pm$ and the lepton is either $e^\mp$ or $\mu^\mp$. No BNV signal was found in any of ten decay channels investigated, and upper limits on branching fraction were set for each of the processes studied, in the range from 7×10^{-7} to 2×10^{-5}.

No previous searches have investigated the possibility of heavy beauty baryons decays involving the violation of $\mathcal{B}$ and $\mathcal{L}$. However, such studies would provide stringent tests of SUSY GUT models.

TABLE 3.1: Negative results of searches for baryon- and lepton-number violating decays, presented as upper limits on branching fractions at 90% CL.

Experiment	Decay mode	$\mathcal{B}(\times 10^{-8})$
CLEO	$D^0 \to \overline{p}e^+$	1100
	$D^0 \to pe^-$	1000
BaBar	$B^0 \to \Lambda_c^+ \mu^-$	180
	$B^0 \to \Lambda_c^+ e^-$	520
	$B^- \to \Lambda \mu^-$	6.2
	$B^- \to \Lambda e^-$	8.1
	$B^- \to \overline{\Lambda} \mu^-$	6.1
	$B^- \to \overline{\Lambda} e^-$	3.2
CLAS	$\Lambda \to K^{\pm} e^{\mp}$	200
	$\Lambda \to K^{\pm} \mu^{\mp}$	300
	$\Lambda \to \pi^{\pm} \mu^{\mp}$	600
	$\Lambda \to \pi^+ e^-$	60
	$\Lambda \to \pi^- e^+$	40
	$\Lambda \to \overline{p}\pi^+$	90
	$\Lambda \to K_S^0 \nu$	2000

3.2 $b\bar{b}$ cross section measurements in pp collisions at LHC

The bottom production measurements in hadronic collisions have suffered from large discrepancies between the data and theoretical predictions. The theoretical calculation to $\mathcal{O}(\alpha_s^3)$ of the inclusive bottom quark transverse momentum spectrum in hadronic collisions shows reasonable agreement with the data. Still, the comparisons are affected by large theoretical errors.

Both the ATLAS and CMS experiments have carried out measurements of the b-jet production cross section in the pp collisions as a function of transverse momentum at $\sqrt{s} = 7$ TeV in different rapidity ranges. The inclusive double-differential b–jet cross-section, measured as a function of transverse momentum, is shown in Fig.3.1, where the comparison with the NLO QCD predictions are included.

The results from [49] obtained by the ATLAS Collaboration agree well with the NLO QCD predictions (POWHEG). The MC@NLO shows good agreement with the measured $b\bar{b}$–dijet cross-section. However, it does not reproduce the measured inclusive cross-section well, particularly for b-jets with large transverse momenta. Similarly, the results from [50] obtained by CMS are found to be in reasonable agreement with MC@NLO.

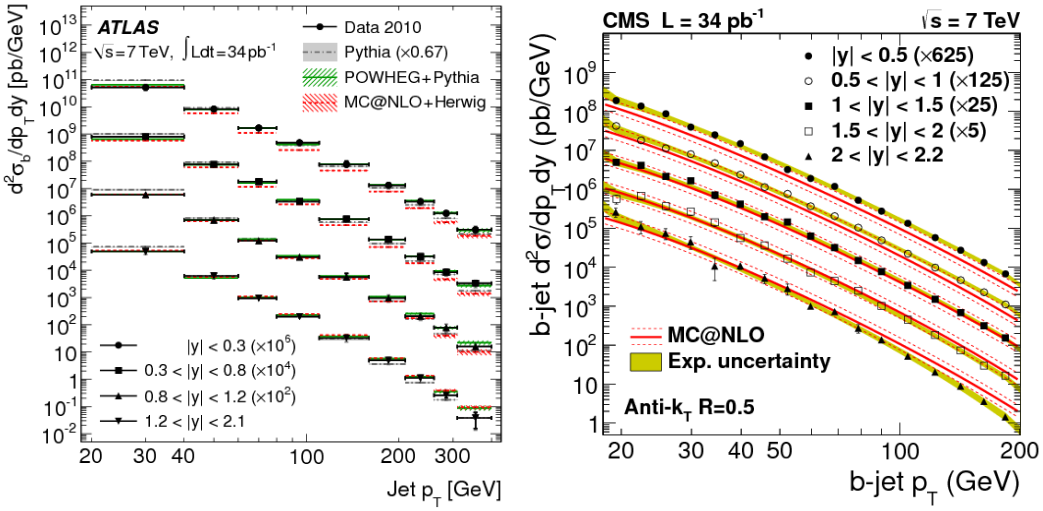

FIGURE 3.1: The inclusive double-differential b–jet cross-section from the jet analysis as a function of p_T for different rapidity ranges for ATLAS and CMS. Figures adopted from [49, 50].

The LHCb Collaboration has previously carried out the measurement of $\sigma(pp \to b\bar{b}X)$ at $\sqrt{s} = 7$ TeV in the forward region [51]. This measurement was based on exclusive decays of b–hadrons into final states containing a D^0 meson and a muon. Two independent data samples, "microbias" and "triggered", have been examined[7]. The extracted cross-sections are shown in Fig.3.2 as a function of η for both data sets and the average. Two theories that predict b production cross-section as a function of pseudorapidity η are used for comparison with data. The MCFM [52] and FONLL [53] models both exhibit NLO accuracy, but the latter improves the NLO result with the resummation of p_T logarithms up to next-to-leading order. In addition, this method also includes the b–quark fragmentation into hadrons. It has been found that the measured cross-section is consistent with theoretical predictions, both in normalization and η–dependent shape. However, as it may bee seen for the FONLL model, the comparison of the measurement with model predictions is affected by large theoretical uncertainties.

The measurement of $\sigma(pp \to b\bar{b}X)$ based on the b–hadron inclusive final states has also been performed at LHCb and the results have been published in [54]. This measurement is related to the scope of present thesis and is described in Sect.6.2.

[7] These samples have been recorded at different times. The microbias sample corresponds to the time when HLT (see Sect.4.2.2) could process all crossings since the number of colliding bunches was sufficiently low. This sample possesses accepted events where at least one track was reconstructed in either the VELO (see Sect.4.2.1.1) or the tracking stations (see Sect.4.2.1.2). The triggered sample uses triggers designed to select a single muon.

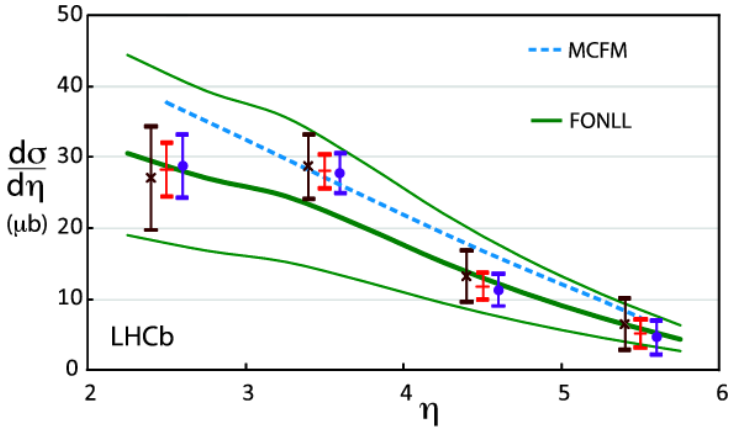

FIGURE 3.2: The cross-section for the process $pp \to b\bar{b}X$ as a function of η for different samples: microbias ($\times$), triggered ($\bullet$) and the average ($+$). The data are represented as points with error bars, the MCFM prediction as a dashed line, and the FONLL prediction as a thick solid line. The thin upper and lower lines indicate the theoretical uncertainties on the FONLL prediction. The systematic uncertainties in the data are not included. Figure adopted from [51].

Chapter 4

Experimental environment

This study has been performed using the data collected over the years 2011 and 2012 by the Large Hadron Collider beauty (LHC*b*) experiment, operating at the Large Hadron Collider (LHC) accelerator at the laboratory complex of the European Organization of Nuclear Physics (CERN, fr. Conseil Européen pour la Recherche Nucléaire) near Geneva. In the following chapter the LHC accelerator complex and the conditions under which the LHC*b* experiment gathers data are briefly described. Next, a description of the detector is provided, including all subsystems necessary for its operation. This chapter concludes with a discussion of the LHC*b* trigger system and the preselection, the so-called stripping.

4.1 The Large Hadron Collider

The LHC accelerator [55], which is currently the most powerful of its kind in the world, is the final element in a succession of machines that accelerate particles at CERN. It is a two-ring superconducting accelerator and collider installed in a tunnel of 27 km in circumference that straddles the French-Swiss border to the north-west of Geneva, 50 to 175 m below the ground. Its primary operation mode is the proton-proton (pp) collision; however, it has also collided protons with lead ($\mathrm{p\text{-}Pb}$) and lead–lead ($\mathrm{Pb\text{-}Pb}$) nuclei.

In the so-called *Run 1*, which stands for the 2011-2012 data taking period, the LHC was providing pp collisions at a bunch crossing rate of $40\,\mathrm{MHz}$, with a centre of mass energy of $\sqrt{s} = 7\ \mathrm{TeV}$ (2011) and $\sqrt{s} = 8\ \mathrm{TeV}$ (2012) and nominal luminosity of $1 \times 10^{-34}\mathrm{cm}^{-2}\mathrm{s}^{-1}$.

Fig.4.1 shows a schematic overview of the LHC together with a set of pre-accelerators. Each machine boosts the energy of a beam of particles before injecting the beam in a consecutive order into Linac2 [56], the Proton Synchrotron Booster (PSB) [57], the Proton Synchrotron (PS) [58] and the Super Proton Synchrotron (SPS) [59].

The protons are produced by ionisation of hydrogen atoms with an electric field. The first accelerator in the chain, Linac2, accelerates the protons to the energy of $50\ \mathrm{MeV}$. The beam is then injected into the PSB, made up of four superimposed synchrotron rings, which accelerates the protons up to $1.4\ \mathrm{GeV}$. Subsequently, the protons are injected into the PS which pushes the beam to $25\ \mathrm{GeV}$, followed by the SPS, the last stage before entering the LHC, where they are accelerated to $450\ \mathrm{GeV}$. Finally, the protons are injected into the LHC main ring.

In order to accelerate the look-alike particles in the opposite directions, two separate beam pipes are used, each with a magnetic field in opposite directions. A series of $400\ \mathrm{MHz}$ radio-frequency (RF) cavities is used, together with 8.3 T dipole bending magnets, quadrupole focusing and defocusing magnets as well as sextupole and decapole corrector magnets.

The RF cavities are responsible for accelerating the beam and providing an energy gain of $\simeq 0.5\,\mathrm{MeV}$ per turn. Unlike the other accelerators in the CERN infrastructure, which use warm (room temperature) iron magnets, the magnets in the LHC main ring are superconducting and operate at liquid helium temperatures.

In the LHC ring there are four interaction points. Three of them are equipped with detectors for pp collision physics (ATLAS, CMS and LHCb [60]) and one (ALICE [61]) for dedicated heavy ion physics.

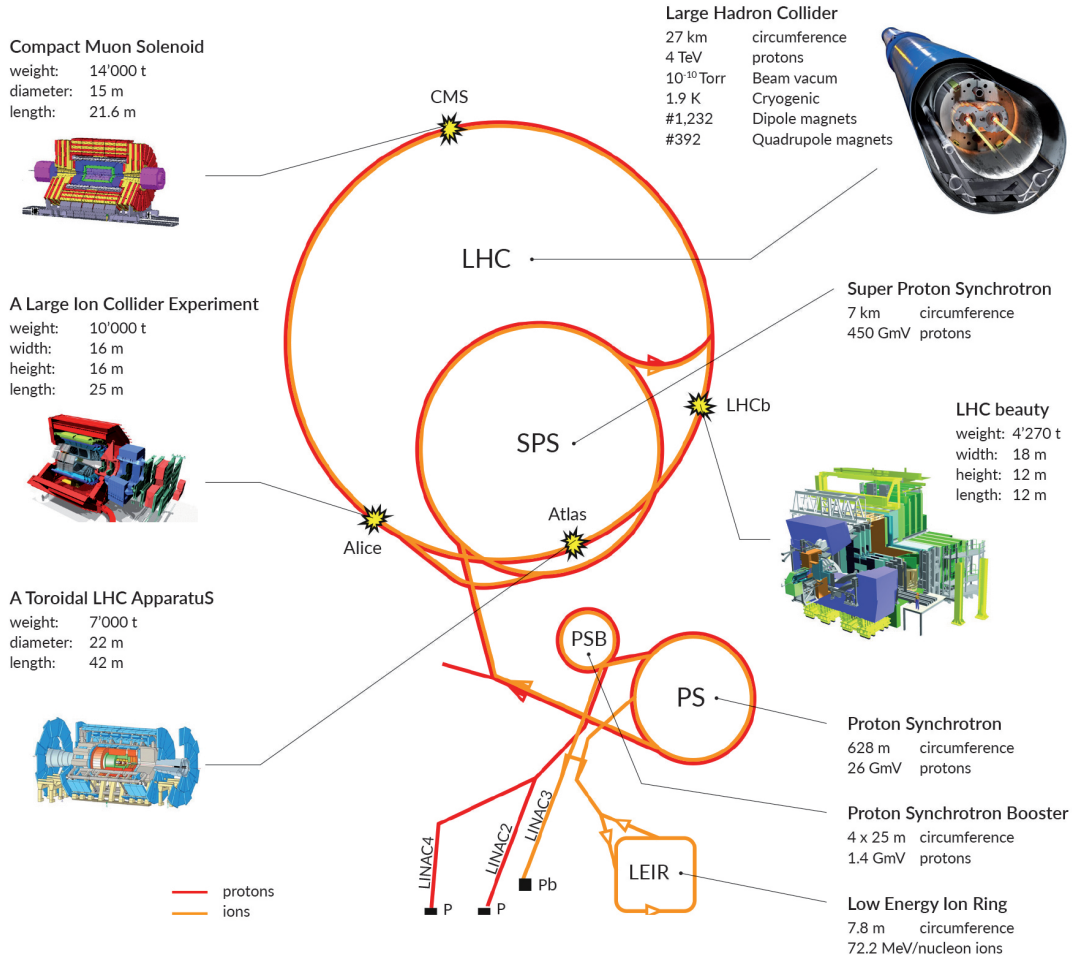

FIGURE 4.1: Layout of the CERN accelerator complex.

4.2 LHC*b* spectrometer

LHC*b* is one of four large-scale experiments established at the LHC facility. In addition to the general purpose detectors (GPD) of ATLAS and CMS, and likewise the ALICE one, the LHC*b* spectrometer is designed to study specific phenomena. Its primary goal is to look for indirect evidence of BSM physics in CP violation and rare decays of beauty and charm hadrons. In addition, owing to the long length of the vertex detector and its excellent tracking capabilities, the LHC*b* experiment has a sensitivity for long-lived exotic particles identified by their decay into SM particles at a decay vertex displaced from the primary interaction point.

All four detectors are installed underground in caverns localized at four interaction points set up on the LHC ring. Contrary to the enclosed detector type that surrounds the entire collision region, such as ATLAS and CMS, the LHC*b* detector uses a series of subsystems to detect mainly particles produced in the forward direction. Therefore it is a single-arm forward spectrometer.

The layout of the LHC*b* detector is shown in Fig.4.2. The right-handed coordinate system with the origin in the interaction point has the z-axis pointing downstream and y-axis pointing vertically upwards. The choice of the detector geometry is justified by the fact that the dominant $b\bar{b}$ production mechanism at the LHC is the gluon fusion where the momenta of the incoming partons are strongly asymmetric in the laboratory frame. Consequently, the centre of mass energy of the produced $b\bar{b}$ pair is boosted along the direction of the higher momentum gluon, and both b hadrons are produced in the same forward (or background) direction (*cf.* Fig. 4.3). For that reason the LHC*b* apparatus stretches along the beam pipe, covering only about 4% of the solid angle around the beam pipe[8], which corresponds to the pseudorapidity (see Sect. 5.3.1) coverage of $1.8 < \eta < 4.9$. Such an angular acceptance allows capturing half of the produced $b\bar{b}$ pairs. This leads to precise measurement of the cross section for inclusive jets and dijets that might be of interest to low-x perturbative QCD tests.

[8] The forward angular coverage is approximately from 10 to $300(250)$ mrad in the bending (non-bending) plane.

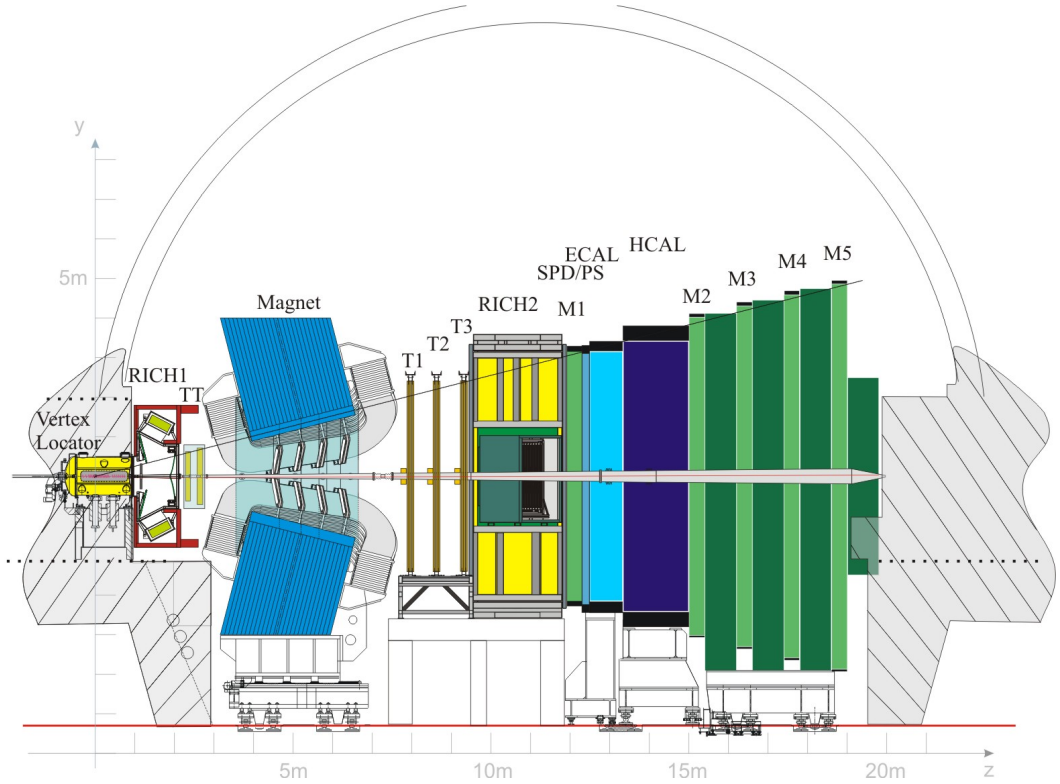

FIGURE 4.2: Side view of the LHC*b* detector. The right-handed coordinate system adopted has the z-axis along the beam line, and the y-axis along the vertical one. The schema shows the VErtex LOcator, the dipole magnet, two RICH detectors, four tracking stations TT and T1- T3, the Scintillating Pad Detector, Preshower, Electromagnetic and Hadronic calorimeters, and five muon stations M1- M5. The region of the detector at positive (negative) z values is known as the forward (backward) or downstream (upstream) end. Figure adopted from [62].

The LHC*b* detector was designed to operate at a luminosity of $2\times10^{32}\,\mathrm{cm}^{-2}\mathrm{s}^{-1}$, which is considerably below the luminosity at which ATLAS and CMS are working ($\mathcal{L} = 1 \times 10^{34}\,\mathrm{cm}^{-2}\mathrm{s}^{-1}$). Thus, the luminosity in LHC*b* is being locally controlled using a luminosity levelling technique [63]. A constant luminosity is delivered to LHC*b* throughout the fill to yield a mean value within $(2\text{-}5) \times 10^{32}\,\mathrm{cm}^{-2}\mathrm{s}^{-1}$. An example of instantaneous luminosity curves for a typical LHC fill is given in Fig.4.4 (on the left). It follows that the number of pp interactions per bunch crossing in visible events (the so-called pile-up) is limited to such a level that the risk of radiation damage of the vertex detector as well as combinatorial background is minor. In fact, events containing more than one interaction per bunch crossing are expected to create a difficult environment for b-physics analyses [64].

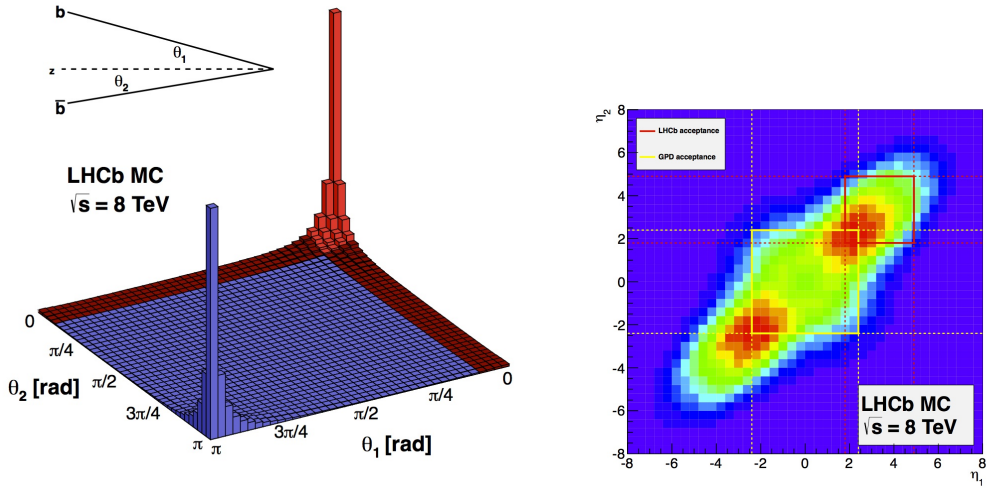

FIGURE 4.3: Forward-background production fractions as a function of b-quark polar angle with respect to the beam axis for simulated $b\bar{b}$ pairs (left). Pseudorapidity of $b\bar{b}$ pairs (right), where the LHCb acceptance is marked in red. Figures adopted from [65].

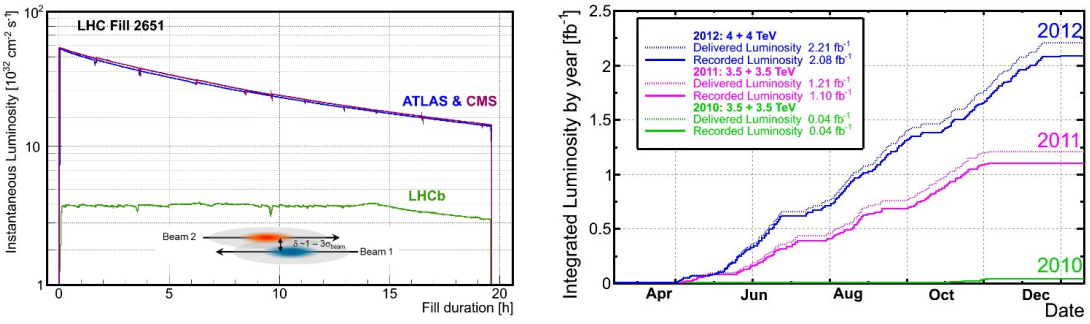

FIGURE 4.4: Typical evolution of the luminosity during an LHC fill (left) and the integrated luminosity collected by the LHCb detector in 2010-2012 (right). Figures adopted from [66, 67].

The most important LHCb running parameters in *Run 1* are summarized in Tab.4.1. In 2011 the LHCb was operating with close to or above the designed values for both the luminosity and the number of visible interactions per bunch crossing. Successfully, in 2012 the well operating apparatus allowed the spectrometer to work in a more harsh environment. Over the whole *Run 1* the LHCb detector demonstrated an excellent performance, reaching 91% and 95% of data taking efficiency in 2011 and 2012, respectively. This allowed the experiment to collect the data samples corresponding to an integrated luminosity of $1.107\,\text{fb}^{-1}$ and $2.082\,\text{fb}^{-1}$ of pp collisions at a centre-of-mass energy of $7\,\text{TeV}$ and $8\,\text{TeV}$ collected in 2011 and 2012, respectively (*cf.* Fig.4.4 on the right).

The reconstruction of beauty hadrons requires effective tracking and particle identification systems specialized in collecting specific information about particles produced in pp collisions. The following subsections discuss briefly the LHCb sub-detectors, focusing on the features most relevant to the analysis in the present thesis. More details can be found in [62].

TABLE 4.1: LHC*b* running parameters in 2011 and 2012.

Year	2011	2012
Beam energy (TeV)	3.5	4.0
Instantaneous luminosity ($\times 10^{32}\,\mathrm{cm}^{-2}\mathrm{s}^{-1}$)	2–4	4
Visible interaction/beam crossing	$\mu = 0.4$–1.4	$\mu = 1.6$
Data taking efficiency (%)	> 91	> 95
High Level Trigger output rate (kHz)	3	4.5
Integrated luminosity recorded (fb^{-1})	1.107	2.082

4.2.1 Tracking system and particle identification

An efficient tracking system and particle identification are fundamental for the measurements of the branching fraction of rare decays. Owing to the fact that b-hadrons have a substantial lifetime and as a result of the large boost, they are expected to fly distances of several mm in the detector before decaying. Hence, they are reconstructed in the LHC*b* detector as the secondary vertices (SV) displaced with respect to the beam axis. In spite of that, usually each pp interaction creates around 80 tracks in the LHC*b* detector detached from the so-called primary vertex (PV) [68]. This yields a non-negligible, measurable separation between the PV and SV, the so-called flight distance (FD). The distribution of FD with respect to the interaction point, for reconstructed $B^0 \to K^+\pi^-$ and $\Lambda_b \to pK^-$ decays in the LHC*b* Monte Carlo, is shown in Fig. 4.5. In addition, the decay products of b-hadrons have a large value of the impact parameter (IP, see Sect. 5.3.1). In general, the tracks originating from b-hadron SV have higher values of transverse momenta as compared to the tracks from PV.

The LHC*b* spectrometer tracking system consists of the VErtex LOcator (VELO) and the planar detectors: the Tracker Turicensis (TT), Inner Tracker (IT) and Outer Tracker (OT). The track deviation in the magnetic field of the dipole magnet is used to determine the momentum of the reconstructed particles.

The VELO measures with a high precision the spatial coordinates of the track close to the interaction point and provides the location of SV coming from short lived particles as well as track IP. The TT stations, which sit at the front of the entrance to the magnet, are used to measure the transverse momentum for tracks with large IP, giving the input to the early levels of the trigger system. Such tracks are used in the offline analysis as well to reconstruct the trajectories of long-lived neutral particles that decay outside the fiducial volume of the VELO and of low-momentum particles that are bent out of the LHC*b* acceptance before reaching the OT stations. The signatures of charged particles passing through the detector captured with the tracking system are labelled by tracks and they constitute necessary input to the reconstruction algorithms.

The Particle identification (PID) system consists of a pair of Ring Imaging Cherenkov Detectors responsible for the separation of different long-lived charged hadrons (pions, kaons and protons). Subsequently, there are five muon stations, labelled M1 through M5, that provide fast information for

the high transverse momentum muon trigger and muon identification. The muon stations are separated by the arrangement of the calorimeter system that is located behind the first muon station. The Scintillating Pad Detector (SPD), Pre-Shower (PS), electromagnetic (ECAL) and hadron (HCAL) calorimeters measure the energy of neutral particles.

In the following subsections the construction and operating principles of the above indicated LHC*b* sub-detectors are briefly described.

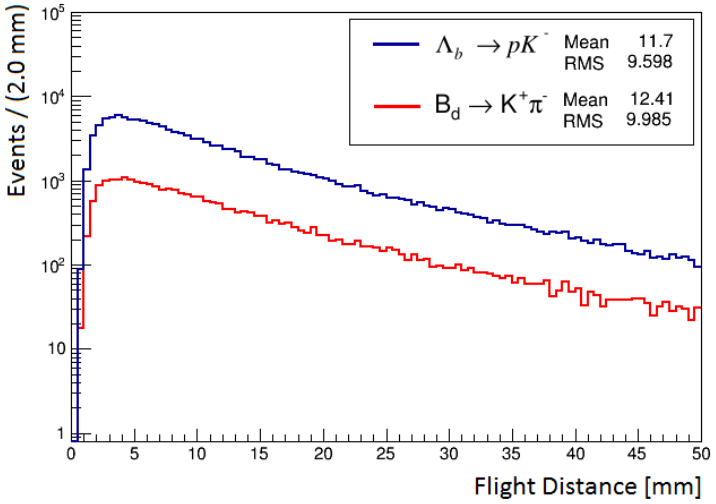

FIGURE 4.5: The reconstructed B_d and Λ_b flight distance in $B^0 \to K^+\pi^-$ and $\Lambda_b \to pK^-$ decays, respectively.

4.2.1.1 VELO

The VErtex LOcator (VELO) is the main tracking device before the magnet and it is crucial for the reconstruction of PV's and SV's. It contains a series of 21 stations arranged along the beam direction with a cylindrical coordinate system. Each station is made of two half disks of silicon microstrip sensors providing r and ϕ coordinates of the trajectory of charged particles. Fig.4.6 shows the layout of the VELO sensor stations.

The VELO layout has been optimized to minimize the amount of material in the acceptance while keeping good geometrical coverage. All tracks inside the LHC*b* acceptance pass through at least three modules. Each module contains one R-sensor measuring the r coordinate and the Phi-sensor providing determination of the ϕ angle (see Fig. 4.7a). The R-sensor has strips arranged radially, while the so-called Phi-sensor has strips arranged approximately azimuthally. This geometry allows precise two-dimensional measurement of the position of a traversing particle, performed in both radial and azimuthal coordinates. Two additional R-type planes of the VELO that are located upstream to the interaction region are used as a pile-up veto detector.

Fig.4.7b shows a picture of a single half of the VELO. The silicon sensors are mounted in a vacuum vessel and separated from the LHC beam by a 200 μm-thick aluminium foil. Each station has left and right parts, which are retracted away from the circulating beam during injection. They are moved back

simultaneously once the beams are stable. For the fully closed stage the inner edge of the detector comes within $7\,\mathrm{mm}$ of the LHC beam.

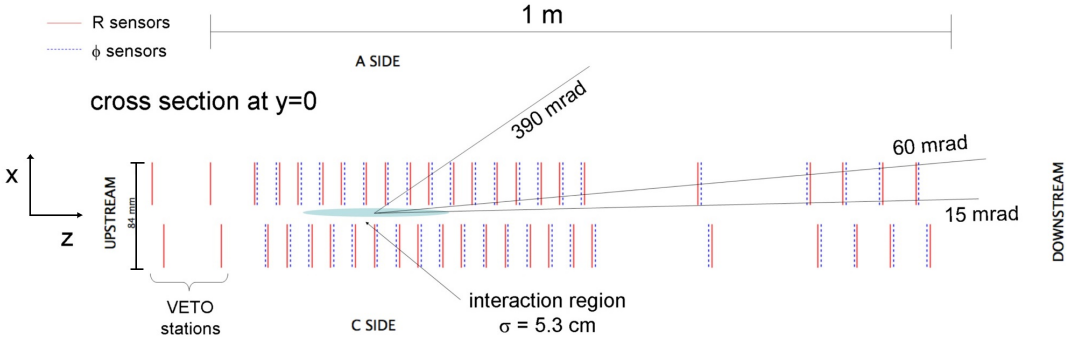

FIGURE 4.6: Schematic layout of the positioning of the VELO stations. Figure adopted from [62].

The VELO detector offers an excellent spatial resolution of about $10\ \mu\mathrm{m}$ in x and y directions and $\sim 40\ \mu\mathrm{m}$ in z. In practice, the number of tracks making a vertex ranges from 5 to around 100. It was found in 2011 data that a 25-track vertex had a resolution in the transverse plane of $13\mu\mathrm{m}$, while the resolution in z was $71\ \mu\mathrm{m}$. The vertex resolution for 2012 data is very similar [69]. Such a precision in the location of the track's origin is crucial for reducing the so-called combinatorial background in which at least one of the tracks gets assigned to the wrong decay vertex. This type of background is the dominant one for most analyses of rare decays.

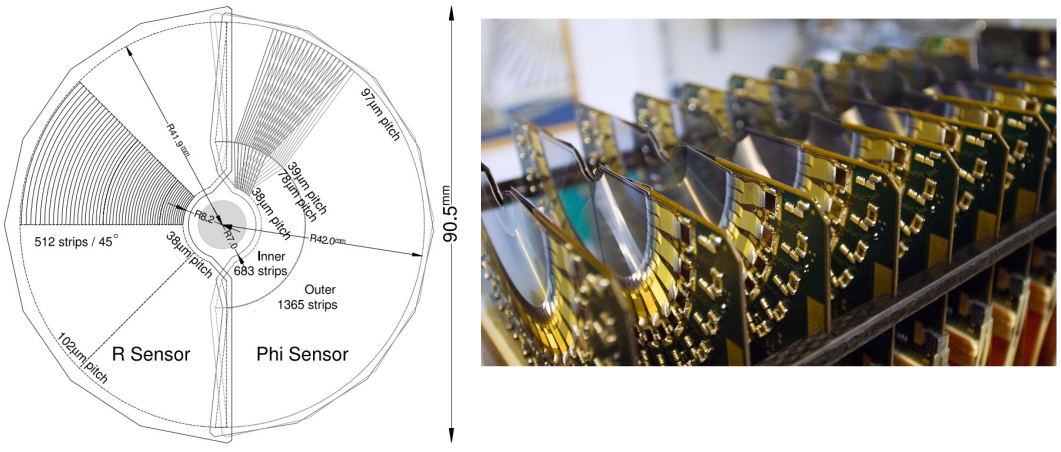

FIGURE 4.7: The VELO sensor $r\phi$ geometry layout (left). For clarity, only a portion of the strips is illustrated. A photograph of one side of the VELO silicon sensors assembly (right) shows the silicon sensors and readout hybrids. Figures adopted from [62, 70].

Another important task of the VELO is to measure the track IP to a high precision, throughout a good understanding of the effects contributing to the

resolution of IP measurement. The requirements on the IP are very effective in excluding prompt backgrounds from long-lived heavy flavour hadron decays and in maximizing the signal content of a data set. The IP resolution is determined to be $< 35\ \mu\mathrm{m}$ for particles with $p_T > 1\,\mathrm{GeV}/c$ [69].

4.2.1.2 TT, IT and OT

The LHC*b* trackers are of two kinds, a silicon tracker and a drift-time detector [62]. The silicon tracker consists of two parts: the TT one, installed between the RICH1 and the entrance to the magnet, and the IT, which covers the closest area around the LHC beam pipe in the tracking stations T1- T3, between the magnet and RICH2.

Fig.4.8 illustrates the layout of the detector layers and shows a photograph of the TT detector taken from the upstream direction. The TT is composed of a single station which covers a rectangular area of approximately $150\,\mathrm{cm}$ in width and $130\,\mathrm{cm}$ in height. Its four detection layers ($X1, U, V, X2$) add up to a total silicon sensitive area of approximately $8\,\mathrm{m}^2$, covering the nominal LHC*b* acceptance of $300\,\mathrm{mrad}$ with silicon micro-strip detectors. The two internal layers are arranged at $stereo$ angle of $\pm 5^\circ$ with respect to x[9]. The silicon sensors for the TT are $500\ \mu\mathrm{m}$ thick single sided p-on-n. They are $9.64\ \mathrm{cm}$ wide and $9.44\ \mathrm{cm}$ long and carry 512 readout strips with a strip pitch of $183\ \mu\mathrm{m}$ [62].

The cross-shaped layout of the IT detector ($120 \times 40\ \mathrm{cm}$) covers only 1.3% of the total sensitive area of each tracking plane in which it is installed. As most of the tracks are produced in the forward/backward region along the beamline, about 20% of the total number of charged tracks in each event is concentrated in this region.

The IT detector modules use the same silicon strip technology as the TT. However, two types of silicon sensors of different thickness are used [62]. The IT module is arranged in the same manner as the TT ones, with two internal layers at a *stereo* angle. Each of the three IT stations consists of four boxes forming a cross-shape around the beam pipe, as shown in Fig. 4.9. The installed detector boxes are showed on the photograph.

The spacial hit resolution is $62\ \mu\mathrm{m}$ and $58\ \mu\mathrm{m}$ for TT and IT, respectively. The corresponding sensors ability to detect charged particles (*i.e.* hit efficiency) was measured to be 99.3% for TT and 99.7% for IT [72].

[9] The *stereo angle* is defined to be positive for a counter-clockwise rotation. The value of $\pm 5^\circ$ gives optimal performance for pattern recognition orientation which prevents ambiguities between the measured hits in order to measure the transverse component of the particle momenta, *i.e.* they improve the precision of the track measurement in x and y and thus the transverse momentum resolution [71].

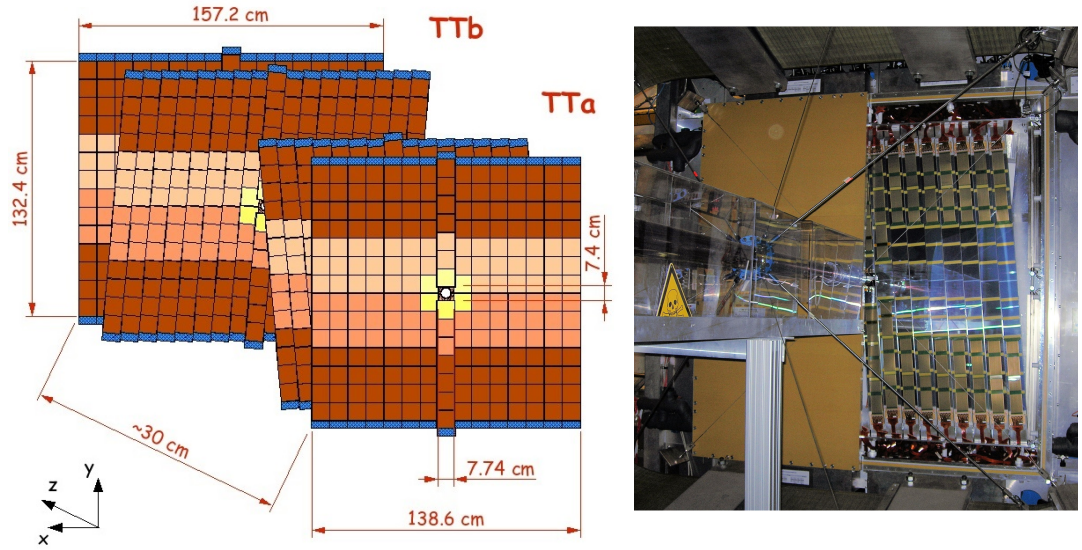

FIGURE 4.8: Layout of the TT detection layers (left): $X1$, V, U, $X2$ (looking downstream). Different readout sectors are indicated by different shadings. A photograph of the TT stations (right): view through the magnet. Figures adopted from [62, 73].

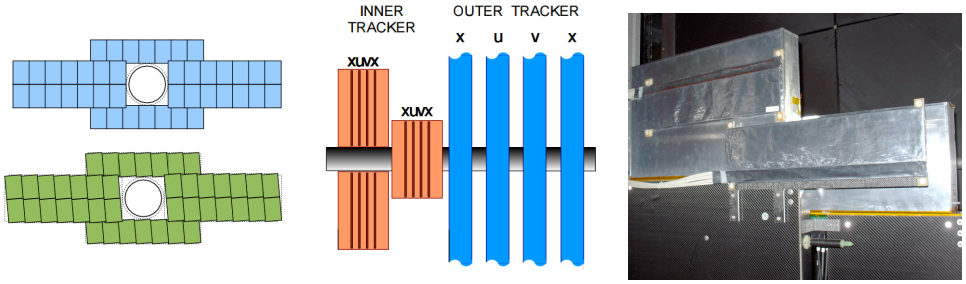

FIGURE 4.9: Front view schematic layout of the IT detector (left), the layout of the IT and OT detector planes in z direction (middle) and a photograph (right) of the the IT boxes. Figures adopted from [62, 73].

The OT detector is settled for the tracking of charged particles and the measurement of their momentum over a large acceptance area [62]. Fig.4.10a illustrates the arrangement of the OT modules. The system is a drift-time detector, where each of the three stations is composed of four layers of drift-tubes with inner diameters of 4.9 mm. Each station is split into two halves, retractable on both sides of the beam line. Each half consists of two independently movable units, known as C-frames. A photograph of the detector unit may be seen in Fig. 4.10b. The geometry of the four layers is identical to that of the TT detector, where the second and third layers are rotated by a *stereo* angle. All modules comprise $53,760$ single straw-tube channels in total. Each drift-tube is filled with a mixture of Argon (70%) and CO_2 (30%), with drift times below 50 ns, and a sufficient drift-coordinate resolution of 200 μm [62]. The hit efficiency near the centre of the straws was measured to be approximately 99% [74].

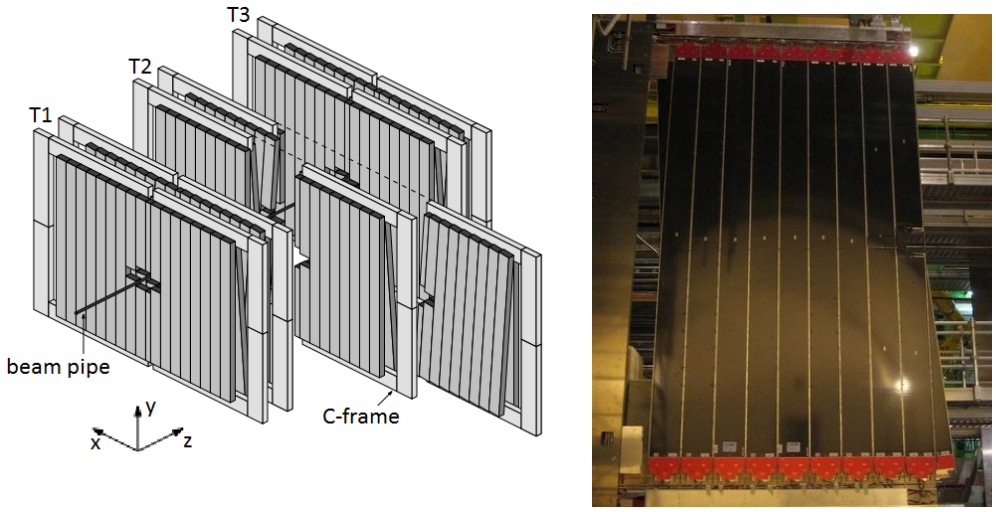

FIGURE 4.10: Arrangement of Outer Tracker straw-tube modules in layers and stations (left) and a photograph (right) of the detector unit for the OT system. The OT is made of twelve such detector units. Figures adopted from [74, 75].

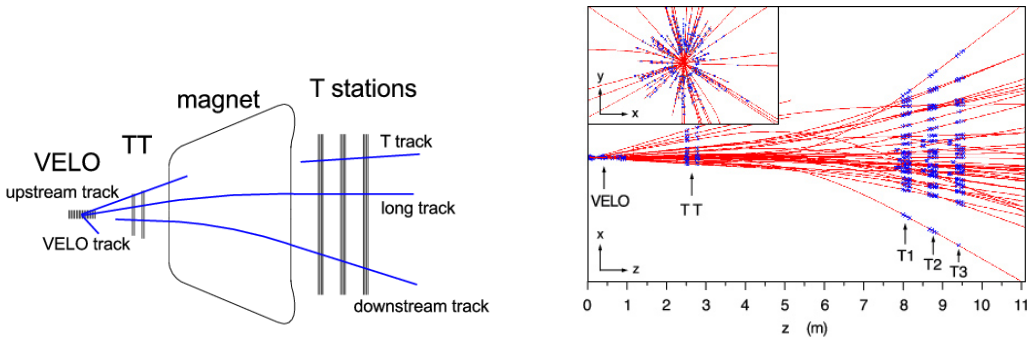

FIGURE 4.11: Tracking detectors and track types reconstructed by the track finding algorithms (left) and the display of the reconstructed tracks and assigned hits (right). The insert shows a zoom into the VELO region. Figures adopted from [76, 66].

The information from all tracking stations is combined with the output from the VELO and the PID system in order to perform a complete reconstruction of the particle's trajectory as well as the track association. This is obtained with the help of suite reconstruction algorithms. The different types of tracks, illustrated in Fig.4.11 (on the left), are grouped in five categories:

- **`VELO track`**: has a signature only in the VELO detector and is used in finding primary vertices. Owing to the lack of the magnetic field, the VELO tracks are always reconstructed as straight lines;
- **`Upstream track`**: reconstructed from a VELO track and TT hits. Usually it is a low momentum track which is bent out of the LHCb acceptance by the magnet;
- **`T track`**: with hits in the main tracking stations T1-T3. The seeds obtained here help the pattern recognition in RICH2;

- **`Downstream track`**: has a signature in both the TT and T1-T3 tracking stations, but does not have it in the VELO detector. This type of a track is important in the reconstruction of long-lived particles, such as K_s^0 or Λ^0, which often decay after passing the VELO detector;

- **`Long track`**: has signatures in all subdetectors, from the VELO detector to the T1-T3 tracking stations. Since these tracks pass through the magnetic field, they have the most accurate measured momentum and thus they are the most useful for analysis.

Fig.4.11 (on the right) shows the reconstructed tracks in a typical event. In a signal triggered event in 2011 or 2012, around 60 long tracks are reconstructed.

The track reconstruction algorithms are implemented in the BRUNEL analysis package [77]. As follows, individually found tracks are combined to reconstruct the b-hadron decays using the standard LHC*b* physics selection algorithms implemented in the DAVINCI analysis package [78]. The full LHC*b* data processing chain can be found in Appendix A.

The tracking efficiency is an important quantity in terms of the studies described in this thesis. It is defined as a probability that the trajectory of a charged particle that has passed through the full tracking system is reconstructed. The approach to determine directly the efficiency of reconstructing charged particles as a long track is the so-called *long method* [76]. It uses probe tracks that have hits in the TT and in the muon stations. Fig.4.12 illustrates the track reconstruction efficiencies obtained with the long method for the 2011 and for 2012 data and for simulation as a function of track momentum, pseudorapidity and multiplicity (see Sect.5.3.1). The average efficiency is higher than 95% in the momentum region $5\,\mathrm{GeV/}c < \mathrm{p} < 200\,\mathrm{GeV/c}$ and in the pseudorapidity region $2 < \eta < 5$, which covers the LHC*b* acceptance.

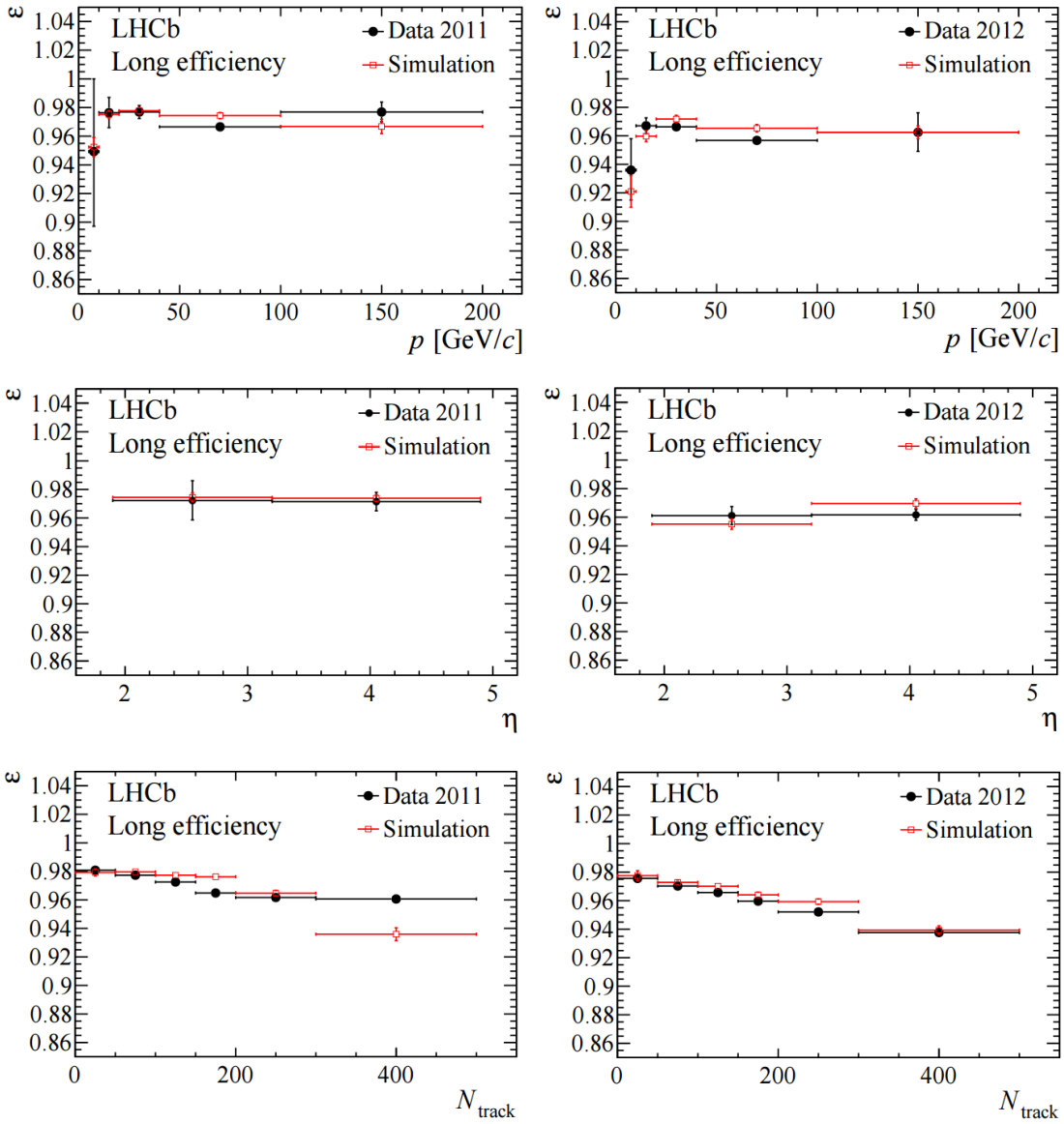

FIGURE 4.12: Track reconstruction efficiencies (ε) for the 2011 and 2012 data and for the simulation. Plots show the results of the long method described in the text. The efficiency is shown as a function of track momentum p (first row), pseudorapidity η (second row) and multiplicity N_{track} (third row). The error bars indicate statistical uncertainties. Plots adopted from [76].

4.2.1.3 The LHC*b* magnet

The LHC*b* warm dipole magnet consists of two huge 27-ton coils mounted inside a 1450-ton iron yoke [62]. The magnet sits between the TT stations and the tracking station T1. A photo of the LHC*b* dipole magnet, taken during the installation of the experiment, is shown in Fig. 4.13.

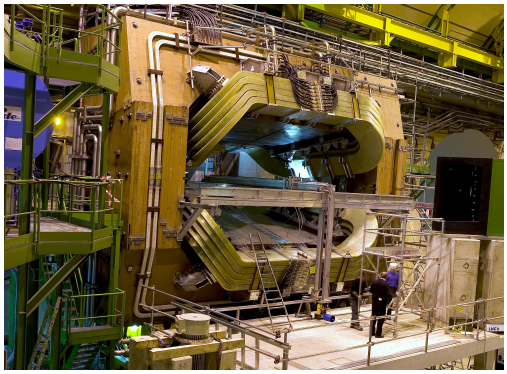

FIGURE 4.13: A photograph of the LHC*b* magnet - two 27-ton coils mounted inside a 1450-ton iron yoke. Figure adopted from [79].

The field of the magnet along z with $x = y = 0$ with both polarities[10] is shown in Fig. 4.14. The field peaks at $1.1\mathrm{T}$ at the centre of the magnet in the $\pm y$ direction. This magnetic field bends particle's trajectories according to their momentum in the $x - z$ plane, and hence makes it possible to measure their momentum as they pass through the detector walls. The impact of the magnetic shielding of RICH1 is clearly visible in a range of 0–2 m.

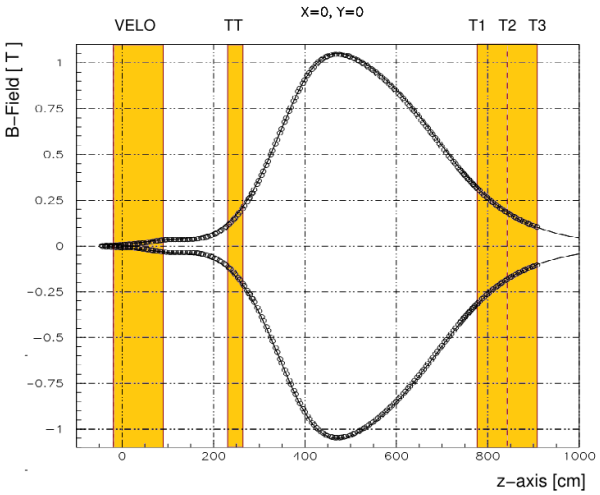

FIGURE 4.14: Measured B-field of the LHC*b* dipole magnet along the z-axis. The positions of the VELO, TT and tracking stations are indicated. Figure adopted from [62].

[10] The polarity of the field is swapped to reduce systematic effects in asymmetry measurements.

4.2.1.4 RICH detectors

A well known technology of particle identification is the Ring Imaging Cherenkov (RICH) detection system. In order to cover the momentum spectrum of the tracks produced in the LHC collisions, different radiators with different optical properties are needed. The Cherenkov angle for different particles as a function of track momentum in different radiators is shown in Fig.4.15 (on the left). As it may be seen, the aerogel radiator is well suited for the identification of low-momentum particles while the CF_4 and C_4F_{10} media provide a good discriminating power at high-momenta (above $20\,\mathrm{GeV}/c$).

The RICH system of the LHC*b* detector is composed of two detectors, RICH1 and RICH2 [62], whose layout can be seen in Fig.4.16. Such a configuration helps to exploit a strong correlation between the polar angle and the track momentum (*cf.* Fig.4.15 (on the right)).

RICH1, presented in Fig. 4.17, is installed upstream the magnet, providing a $300\,\mathrm{mrad}$ polar angle coverage. It is designed for hadron identification of low momentum tracks. It includes two radiators: $5\,\mathrm{cm}$ thick silica aerogel and $95\,\mathrm{cm}^3$ C_4F_{10} gaseous radiators. Spherical mirrors of $190\,\mathrm{cm}$ radius of curvature are tilted by $250\ \mathrm{mrad}$ in order to focus the Cherenkov light onto two photodetector[11] planes ($100\ \mathrm{cm}^2$) outside the detector acceptance.

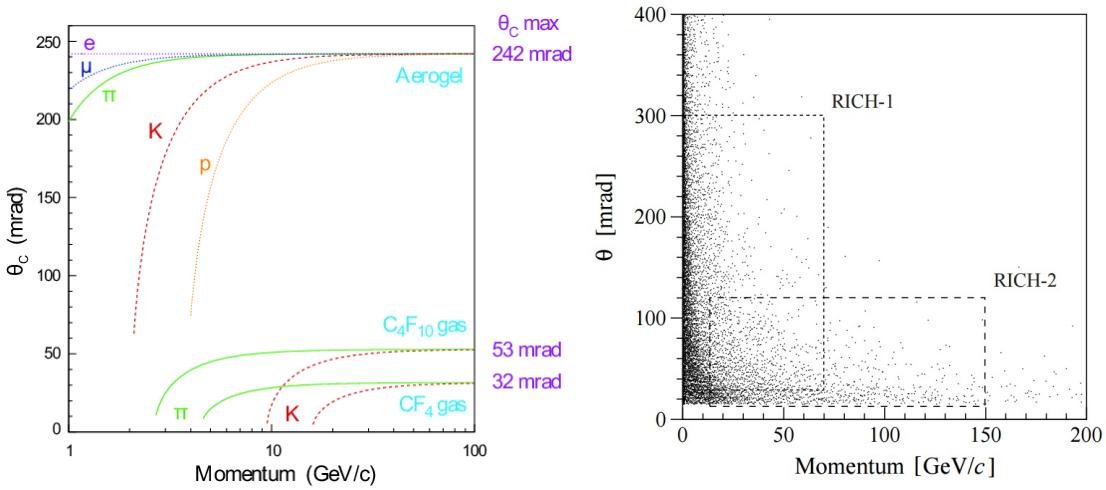

FIGURE 4.15: Cherenkov angles for different particles as a function of track momentum, for different radiators (left) and polar angle correlation with track momentum in the LHC*b* detector. Figures adopted from [62, 80].

[11] RICH utilizes the Hybrid Photon Detectors to measure the spatial positions of emitted Cherenkov photons [62].

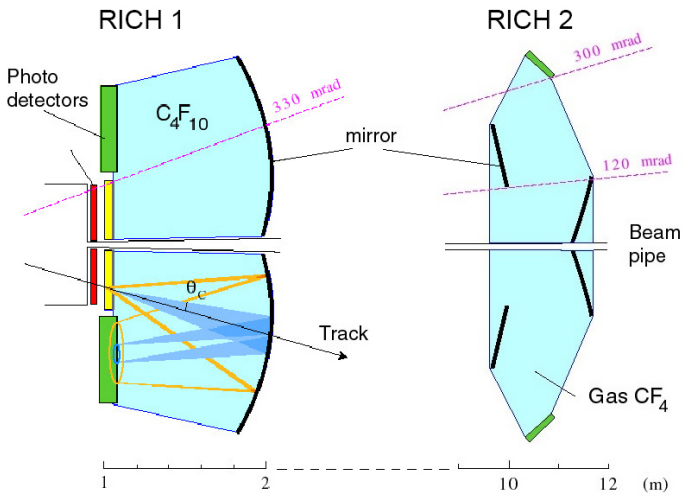

FIGURE 4.16: Schematic layout of the LHC*b* RICH system. Figure adopted from [62].

RICH2, presented in Fig. 4.18, is localized downstream the magnet and in front of the calorimeter. It is intended to measure high momentum and small polar angle tracks. It uses $180\ \mathrm{cm}^3$ of CF_4 gas as a radiator and covers 120 mrad in the bending plane, and 100 mrad in the non-bending plane. The limited RICH2 acceptance covers the region where the majority of high momentum particles are produced. The light reflected with the flat mirror is focused by spherical mirrors (820 cm of radius of curvature) onto two photodetector planes ($120\ \mathrm{cm}^2$) installed outside the detector acceptance.

The PID strategy combines measured quantities by other subsystems, namely the calorimeter and muon systems, that together with those obtained by the RICH system allow the identification of different charged particles produced in a single pp collision. As follows, the overall likelihood is resolved and the difference in logarithmic likelihood is defined as:

$$\mathrm{DLL}_{\mathrm{AB}} = \ln\mathcal{L}_{\mathrm{A}} - \ln\mathcal{L}_{\mathrm{B}}, \tag{4.1}$$

where $\mathcal{L}_A$ and $\mathcal{L}_B$ stand for a likelihood that the particle is identified under the A and B hypothesis, respectively ($\mathrm{A}, \mathrm{B} = \pi, \mathrm{K}, \mathrm{p}, \mu, \mathrm{e}$). In view of the fact that the most numerous particle type produced in the LHC*b* environment is a pion, the DLL is obtained for $e, \mu, \mathrm{K}, \mathrm{p}$ with respect to a pion. For example, in the case of $\mathrm{DLL}_{K\pi} < 0$ the particle is more likely a π, whereas for $\mathrm{DLL}_{K\pi} > 0$ it is more likely a K.

In addition, the approach of the multivariate particle identification classifier is provided within the LHC*b* framework. It is an artificial neural net combining inputs from the PID subdetectors and tracking information of likelihood ratios, called ProbNN [81, 82]. The training is done using MC inclusive b-hadron events and for charged tracks an appropriate set of ProbNN_K, ProbNN_π, ProbNN_p, ProbNN_e variables is determined.

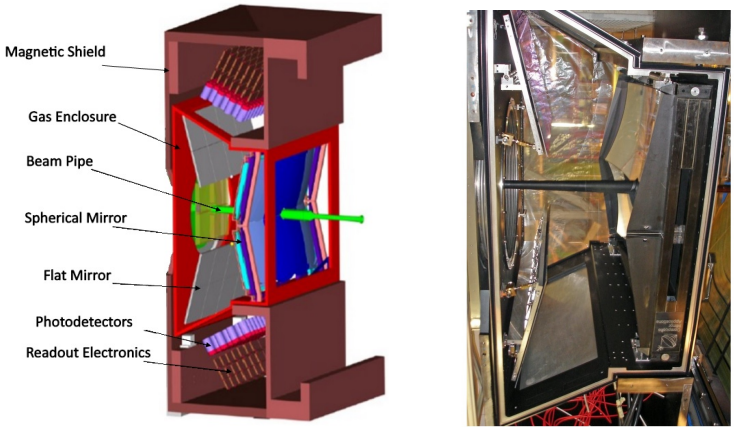

FIGURE 4.17: Geometry of the RICH1 detector (left) and a photograph (right) of the RICH1 gas enclosure containing flat and spherical mirrors. The interaction point is on the left side of the photo. Figures adopted from [62].

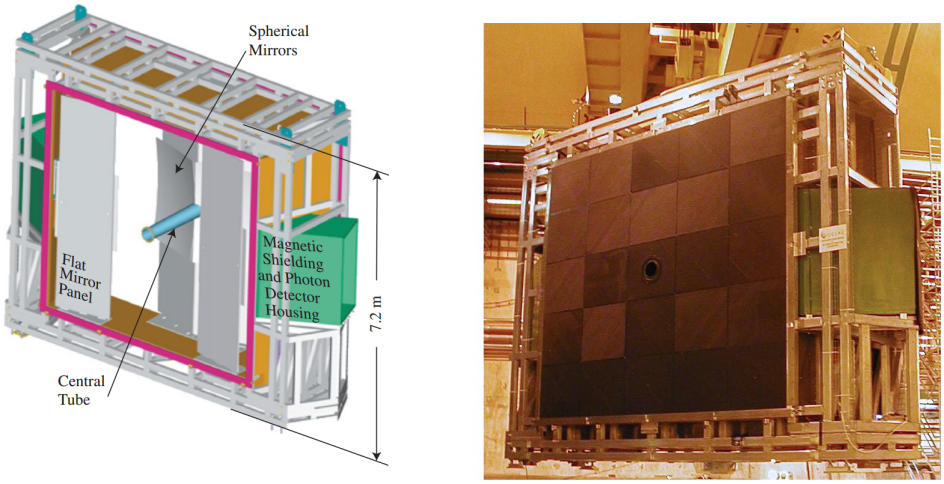

FIGURE 4.18: Geometry of the RICH2 detector (left) and a photograph (right) of the RICH2 detector. Figures adopted from [62, 83].

The RICH system provides good particle identification over a large momentum range from ~ 2 GeV/c up to ~ 100 GeV/c. Fig.4.19 (on the left) demonstrates the kaon identification efficiency and pion misidentification (pions misidentified as kaons) as a function of particle momentum obtained for two different $\mathrm{DLL}_{K\pi}$ requirements. The likelihood for each track with the kaon mass hypothesis is larger than the one with the pion hypothesis ($\mathrm{DLL}_{K\pi} > 0$). Taking the average of the momentum range (2-100) GeV/c, the kaon identification efficiency and pion misidentification fraction are found to be $\sim 95\%$ and $\sim 10\%$, respectively. The alternative requirement of $\mathrm{DLL}_{K\pi} > 5$ shows that the misidentification rate can be significantly reduced to $\sim 3\%$ for a kaon efficiency of $\sim 85\%$. Similarly, Fig.4.19 (on the right) illustrates the discrimination between protons and pions obtained after imposing the requirements $\mathrm{DLL}_{p\pi} > 0$ and $\mathrm{DLL}_{p\pi} > 5$.

In the matter of the analysis performed in this dissertation, the distinction between kaons, protons and pions is crucial, since it is needed to discriminate final states from otherwise identical topology.

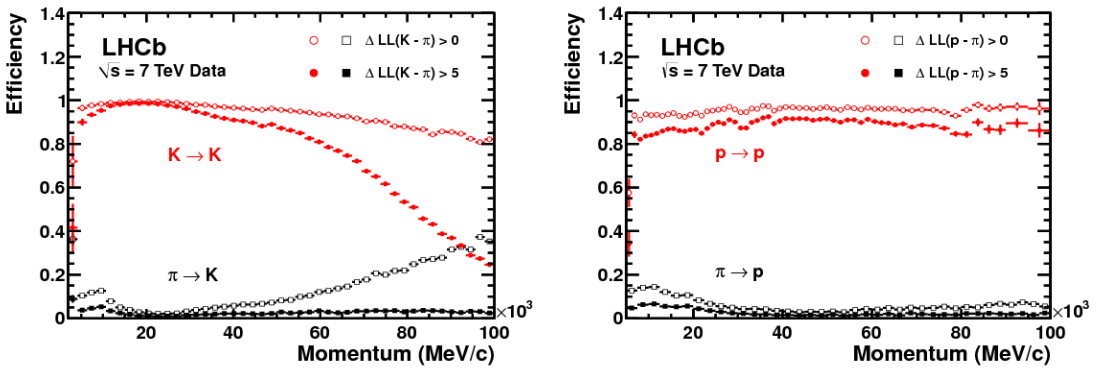

FIGURE 4.19: Kaon identification efficiency and pion misidentification rate (left). Proton identification efficiency and pion misidentification rate (right). Both measured on data as a function of track momentum. Plots adopted from [84].

4.2.1.5 Calorimeter system

The LHC*b* calorimeter system provides measurements of the energies and transverse positions of electrons, photons and hadrons. It is a crucial contribution to the hadronic early stage trigger makes it possible to recognize objects with high transverse energy (E_T). In addition, the system measures the neutral particle energy used in particle identification for offline analysis.

A classic layout of the calorimetric subsystems follows the principle that the energy of an incident particle is lost after a cascade of interaction with the absorber material of the calorimeter. During this process, electromagnetic and/or hadronic showers of secondary particles are produced. The total energy of all showers absorbed in the active material is measured, which corresponds to the initial energy of the incident particle.

The LHC*b* calorimeter system is subdivided into four subsystems. It is composed of the SPD, which is designed to identify charged particles, followed by a wall of lead, and then the PS, ECAL and HCAL [62]. This arrangement comes along with the characteristics of the longitudinal profile of the produced showers, downstream. All subsystems are divided into two halves that can be retracted horizontally from the beam.

The SPD and PS systems presented in Fig. 4.20, were designed to improve the spatial and energy resolutions of electromagnetic showers. They are two almost identical layers of high granularity scintillator pads. Three different pad sizes ranging from $40.4 \times 40.4\,\mathrm{mm}^2$ in the inner region to $121.2 \times 121.2\,\mathrm{mm}^2$ in the outer region were adapted to the particle flux. A lead converter of $15\,\mathrm{mm}$, corresponding to 2.5 radiation length (X_0) of the material involved, is located between the two scintillator planes and allows electrons to start showering before the ECAL.

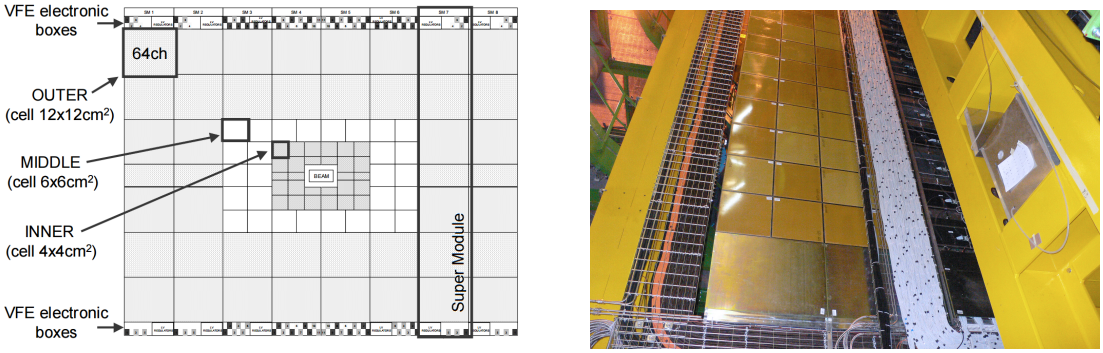

FIGURE 4.20: The layout of the calorimeter system : SPD/ PS detector scheme (left). A photograph (right) from upstream side of the side C of the SPD when opened. A part of the first module of the PS can also be seen. Figures adopted from [85, 86].

Fig.4.21 illustrates the elementary periodic structure of both the ECAL and HCAL calorimeters, while Fig.4.22 shows the granularities for different detector regions. Similarly to the PS/SPD detectors, the ECAL is divided into three regions with different cell sizes, whereas the HCAL has two different cell sizes.

The ECAL is built out of 3300 *shashlik* type detector modules with $4\,\mathrm{mm}$ thick scintillating tiles alternated with $2\,\mathrm{mm}$ thick lead sheets [87]. Scintillation light is captured and transported via wavelength shifting (WLS) fibers running through the holes in the module to photomultipliers located at the module's end. The total depth of the electromagnetic calorimeter is $25X_0$, and the energy resolution is $\sigma_E/E = 10\%/\sqrt{E\,\mathrm{GeV}} \otimes 1\%$ [12] [88].

The HCAL is an iron/scintillator calorimeter with tile geometry. The scintillator tiles are $4\,\mathrm{mm}$ thick alternated with $16\,\mathrm{mm}$ thick iron. Scintillation light is guided through WLS fibers at the edge of the modules to photomultiplers for further readout. The total depth of the hadronic calorimeter is 5.6 of hadronic interaction length (λ_I), and the energy resolution for hadrons is $\sigma_E/E = 69\%/\sqrt{E\,\mathrm{GeV}} \otimes 9\%$ [88].

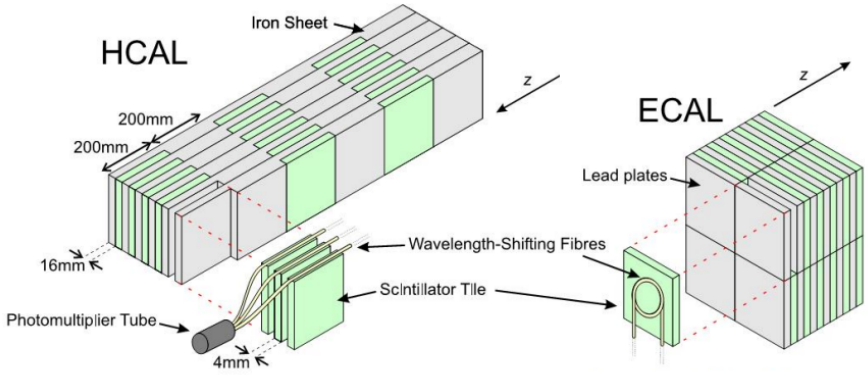

FIGURE 4.21: Elementary periodic structure of calorimeters. Figure adopted from [62].

[12] $\otimes$ - adding in quadrature.

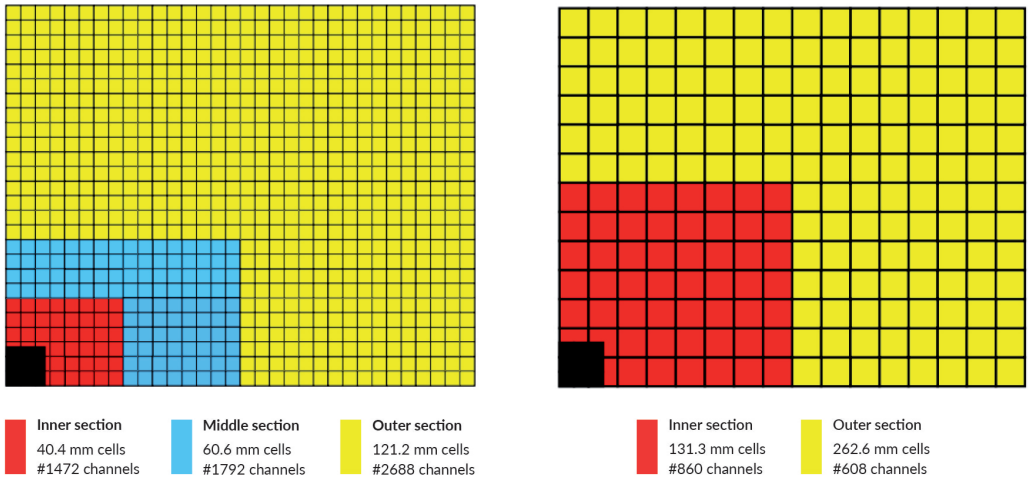

FIGURE 4.22: Granularity for different detector regions of the SPD, PS, ECAL (left) and HCAL (right). One quarter of the detector is shown. The cell dimensions are given for ECAL and reduced by $\approx 1.5\%$ for SPD/ PS. Figures adopted from [62].

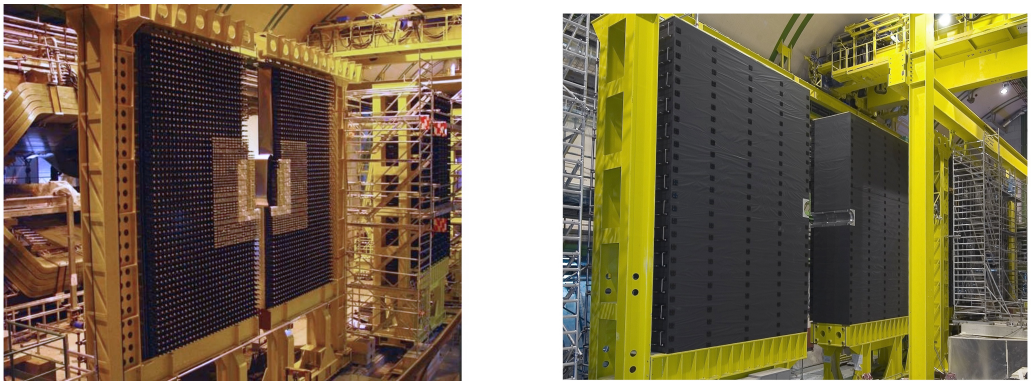

FIGURE 4.23: A photograph from upstream side of the ECAL (left) and HCAL (right) detectors. Figures adopted from [89, 90].

4.2.1.6 Muon system

The LHC*b* muon detection system is primarily used to trigger on high p_T muons at the early level trigger and to identify all final state muons in the offline reconstruction. Consequently, the efficient and accurate detection and identification of muons play a crucial role in many of the key decays defined in the wide LHC*b* physics program, since they are present in the final states of the considered decay channels [91]. The muon identification is an essential feature in the analysis performed in this dissertation.

The muon detection is performed in five stations of muon chambers (M1-M5) of rectangular shape, positioned at the most downstream side of the LHC*b*
spectrometer [62]. Fig.4.24 (on the left) illustrates the layout of the muon system. The station M1 is positioned in front of the SPD and PS. The remaining four

stations (M2-M5) are placed downstream the calorimeter system and are interleaved with $80\,\mathrm{cm}$ thick iron absorbers to absorb hadrons from the calorimeters. In addition, the presence of these iron walls means that muons with momenta below $6\,\mathrm{GeV}/c$ cannot reach the M5 station.

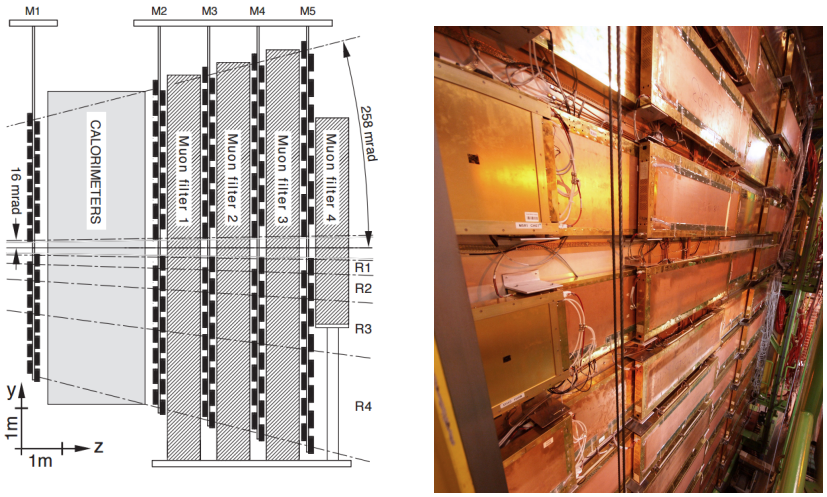

FIGURE 4.24: Side view of the muon system layout(left) and a photograph (right) of the back view of the M5 station wall. Figures adopted from [92, 93].

The muon chambers are gaseous detectors, multi-wire proportional chambers (MWPC) with Ar/CO2/CF4 (40:55:5)% as a gas mixture used for all regions except the inner region (R1) of the station M1. Because of higher occupancy this region is instrumented with gas electron multipliers (GEM) filled with Ar/CO2/CF4 (45:15:40)% [62]. In addition, in a similar way as in the calorimeter, there are different regions in the muon station with different granularity patterns, R1 to R4, with increasing distance from the beam axis. A photograph of the back view of the muon chambers installed in the M5 station can be seen in Fig.4.24 (on the right).

To comply with the stringent requirements of the trigger at its earliest level, the excellent time resolution and efficiency of each muon station are needed. This is obtained with the chamber geometry and gas mixture described above. Moreover, the muon identification procedure should provide high muon efficiency while keeping the incorrect identification probability of hadrons as muons at the lowest possible level. An average muon identification efficiency at 98% level is feasible for pion and kaon misidentification below 1% at high transverse momentum [92]. This excellent performance of the muon system makes the LHC*b* apparatus a perfect experimental environment for studying decays with muons in the final state.

4.2.2 The trigger and stripping

The rate at which data are produced in LHC*b* is far larger than the capacity available to record and store it. Hence, a versatile trigger scheme, efficient

for both leptonic and hadronic final states, is required to cope with a variety of modes with small branching fractions.

For the LHC and LHC*b* operation conditions in 2010-2012 the trigger was responsible for reducing the bunch crossing rate from $\sim 15\,\mathrm{MHz}$ to about $5\,\mathrm{kHz}$ of data recorded and stored [62]. To do this efficiently with the minimum necessary buffering, its architecture had been structured intro three levels: one hardware known as Level-0 (L0), and two software called High-Level-Triggers (HLT1 and HLT2).

In order to make a decision the LHC*b* trigger uses all its sub-systems introduced in the previous paragraphs. The conditions describing trigger decisions are collected in the so-called *trigger lines*. Combinations of the trigger lines, together with a L0 configuration, form an unique trigger which is tagged with the Trigger Configuration Key (TCK). The TCK is a 32 bit unique key which labels a trigger configuration where lower 16 bits specify L0 one. For each event the TCK number is stored along with the information which trigger lines accepted this event. During the data taking period the trigger was re-optimized, *i.e.* in 2011 and 2012 two and eight different TCKs were used, respectively. General features of each trigger level are introduced below, while a comprehensive treatment can be found in [62].

The stored data are filtered further through a set of offline selections called the *stripping*, performed centrally by the LHC*b* computing services. To save the disk space and to speed up access to the data, the stripping output files are grouped into *streams* which contain similar selections. The general features of the stripping selection are addressed below.

4.2.2.1 Hardware trigger

The L0 trigger stage has to quickly find general signatures of interesting decays and reduce the event rate from $15\,\mathrm{MHz}$ to $870\,\mathrm{kHz}$[13]. At such a high rate the L0 bases its decision on information from calorimeters and muon chambers. Events with either high p_{T} muons or E_T deposits in the calorimeter are selected. Subsequently, different L0 decisions are assigned to the candidate if the following conditions are satisfied:

- **`L0-Muon`** : occurrence of one stub[14] in the muon chambers with transverse momentum above $1.48\,\mathrm{GeV}/c$;
- **`L0-DiMuon`** : presence of a pair of stubs in the muon chambers with a product of the transverse momenta above $1.296(\,\mathrm{GeV}/c)^2$;
- **`L0-Hadron`** : occurrence of one cluster in the HCAL with transverse energy above $3.5\,\mathrm{GeV}/c^2$;
- **`L0-Photon`** : presence of one cluster in the ECAL with transverse energy above $2.5\,\mathrm{GeV}/c^2$, hits in the PS and no hits in the SPD;

[13] $\sim$1 MHz is the frequency at which the full detector can be read out.

[14] A track segment within one station in the (x, z) projection.

- **`L0-Electron`** : occurrence of one cluster in the ECAL with transverse energy above $2.5\,\mathrm{GeV}/c^2$, hits in the PS and at least one hit in the SPD.

The threshold on the number of tracks is set to be lower than 900 hits for L0-DiMuon and lower than 600 hits for other trigger decisions. It allows the L0 trigger to reject candidates with too many particles.

The analysis described in this dissertation uses the L0-Muon and L0-Hadron triggers. The L0-Muon is the main trigger for particle decays with one or more muons in the final state, while the L0-Hadron selects heavy flavour decays with hadrons in the final state.

4.2.2.2 Software trigger

All candidates accepted by the L0 trigger are processed by a purely software trigger, composed of HLT1 and HLT2 stages, running on a PC farm. The HLT1 reduces the output rate of the L0 down to about $50\,\mathrm{kHz}$ and, subsequently, the HLT2 decreases it to $3\,\mathrm{kHz}$ and $5\,\mathrm{kHz}$ in 2011 and 2012, respectively.

The HLT1 examines the L0 decisions with progressively more information from the VELO and the tracking stations. It performs a partial reconstruction of tracks and muon identification by employing a combination of requirements on tracks with a high $\mathrm{p_T}$ and large displacement from the PV.

The HLT2 trigger contains algorithms which are more time-consuming; however, it provides a more precise reconstruction. It reconstructs all tracks in the event with $p_\mathrm{T} > 500\,\mathrm{MeV}/c$ and selects candidates based on the lepton identification, lifetime information and invariant mass [68].

The candidates accepted by the trigger are split into three categories:

- **`Triggered On Signal (TOS)`**: a candidate for which a positive trigger decision is generated owing to the sufficient presence of the signal, *i.e.* the signal under study is sufficient to trigger the event;

- **`Triggered Independently of Signal (TIS)`**: a candidate for which a positive trigger decision is generated independently of the presence of the signal, *i.e.* the event would also have been triggered without the signal under study;

- **`Triggered On Both (TOB)`**: a candidate which is neither `TIS` nor `TOS`.

The LHC*b* trigger system allows the trigger efficiency to be evaluated in a data-driven way, which is called the `TISTOS` technique [94]. A general formula for the trigger efficiency evaluated on the selected events reads

$$\varepsilon_{TOS}^{Trig/Sel} = N_{TISTOS}^{Trig/Sel} / N_{TIS}^{Trig/Sel}, \tag{4.2}$$

which determines the TOS efficiency over a TIS subsample, where all quantities can be measured directly from the data. The assumption that TIS efficiency is independent from the chosen subsample is the main assumption of this approach.

4.2.2.3 Stripping selections

The stripping is a preselection of the channel in question. Each of such loose set of preselection criteria is embedded in a *stripping line*. In the case when stripping lines are updated or new ones are introduced, the data are successively re-stripped. The stripping selection reduces the event rate further by a factor of 10^4. These kinds of selections are offline, *i.e.* they are performed with the data stored on tape. The latest stripping for data from Run 1 is tagged as `S21r0` for 2012 and `S21r1` for 2011. Knowledge of the reconstruction and stripping versions is the most important to identify the data set used in a specific physics analysis. The main groups of similar selections are distributed into the following stripping streams: `Bhadron`, `Charm`, `Dimuon`, `EW`, `Leptonic`, `Semileptonic`, `Radiative`. These selections allow different working groups to avoid processing of the whole triggered dataset. Each individual LHC*b* user can provide his/her set of loose selection criteria for his/her decay in question in a dedicated *stripping line*. However, in the central processing of data, the stripping lines have a finite bandwidth. They must therefore make an initial selection of the decays for general purpose, which preserves as much signal as possible while keeping the retention of candidates within acceptable limits.

Chapter 5

Search for the decay $X_b \to K^- \mu^+$

These studies are devoted to the search for the phenomenon of baryon ($\mathcal{B}$) and lepton ($\mathcal{L}$) number violation, with the $\mathcal{B}$–$\mathcal{L}$ conservation. Many modern extensions of the SM postulate that the baryon number is only an approximate symmetry which is broken by small amounts. If confirmed, it would have a deep impact on our understanding of the evolution of the Universe, both its early history and the late-time future. The violation of the baryon number is an essential ingredient for the creation of an asymmetry between matter and antimatter observed in the present Universe.

The LHC offers a plethora of opportunities in flavour physics, since a complete spectrum of b–hadrons is available at LHC*b*, including $B_{(s)}$, $B^+_{(c)}$ mesons and Λ_b baryons. The work described in the present thesis aimed mostly at searching for baryon and lepton number violation in the decay of $X_b \to K^- \mu^+$ ($X_b = \Lambda_b, \Xi_b^0$). The LHC*b* experiment has already measured a series of quantities related to heavy baryons, which are summarized in Tab.5.1.

TABLE 5.1: Overview of b–baryons considered in the motivated search.

Review of Particle Physics [1]:					
Particle	quark content	mass (MeV/c^2)	lifetime τ (ps)	$c \cdot \tau$ (mm)	$I(J^P)$
Λ_b	udb	5619.5 ± 0.4	1.451 ± 0.013	0.435	$0(\frac{1}{2}^+)$
Ξ_b	usb	5793.1 ± 2.5	1.49 ± 0.19	0.446	$\frac{1}{2}(\frac{1}{2}^+)$
LHCb measurements:					
Measured quantity			Reference		
$m(\Lambda_b) = (5619.53 \pm 0.45)\ \mathrm{MeV}/c^2$			[95]		
$m(\Xi_b) - m(\Lambda_b) = (172.44 \pm 0.39)\ \mathrm{MeV}/c^2$			[96]		
$\to m(\Xi_b) = (5791.9 \pm 0.6)\ \mathrm{MeV}/c^2$					
$\tau(\Lambda_b) = (1.48 \pm 0.01)$ ps			[97]		
$\tau(\Xi_b)/\tau(\Lambda_b) = 1.006 \pm 0.021$			[96]		
$\to \tau(\Xi_b) = (1.477 \pm 0.026)$ ps					
$\frac{f_{\Xi_b^0}}{f_{\Lambda_b}} \frac{\mathcal{B}(\Xi_b^0 \to \Xi_c^+ \pi^-)}{\mathcal{B}(\Lambda_b \to \Lambda_c^+ \pi^-)} \frac{\mathcal{B}(\Xi_c^+ \to pK^-\pi^+)}{\mathcal{B}(\Lambda_c^+ \to pK^-\pi^+)} = (1.88 \pm 0.04 \pm 0.03) \times 10^{-2}$			[96]		
$\frac{f_{\Lambda_b}}{f_u + f_d} = (0.40 \pm 0.11) \times [1 - (0.031 \pm 0.005) \times p_T(\mathrm{GeV})]$			[98]		

An excellent performance of the LHC*b* apparatus allowed the search for the processes in question to be performed. This chapter describes the details of such a measurement in the context of the LHC*b* environmental framework. The

studies have been carried out within the Rare Decays Working Group [99] of the LHC*b* collaboration. The Author of this thesis got along with the main part of each step of the analysis described below.

The early section of this chapter describes the general analysis strategy followed by an outline of the datasets and simulated samples used in this study. The next sections specify the work performed for developing the selection of the signal extraction and a series of cross-checks performed on control channels. Finally, the experimental results are translated into upper limits on the branching fractions as there is no contribution from the considered signal channels.

5.1 Analysis strategy

The study of the decay of $X_b \to K^-\mu^+$ ($X_b = \Lambda_b, \Xi_b$) is based on the measurement of the relative branching ratio. The $\Lambda_b \to pK^-$ decay, whose decay topology is very similar to that of the signal channels, is chosen to be the normalization mode, as it provides enough statistics and its branching ratio is already measured. The advantage of this approach is that the most of the selection efficiency uncertainties tend to cancel in the ratio to a large extent and only a reduced systematic uncertainty will enter into the final result. One may notice that the present uncertainty of $\mathcal{B}(\Lambda_b \to pK^-)$ is relatively high (*i.e.* $18\,\%$ [1]). However, the relevant hadronization factors cancel in the ratio because of the presence of the same hadron in the final state of both decays. A branching ratio, or its upper limit in the case of null observation, could then be simply evaluated by normalizing all measured events or the obtained upper limit related to the known decay.

The generic formula to calculate the number of triggered and selected events reads:

$$N = \int \mathcal{L}dt \cdot \sigma_{b\bar{b}} \cdot 2 \cdot f_q \cdot \mathcal{B}_{\text{vis}} \cdot \varepsilon^{TOTAL}, \tag{5.1}$$

where $\mathcal{L}$ is the integrated luminosity, $\sigma_{b\bar{b}}$ is the $b\bar{b}$ cross section, the factor 2 accounts for the presence of the $b\bar{b}$ pair in each single process, f_q represents the probability of b hadronization to the relevant hadron, $\mathcal{B}_{\text{vis}}$ stands for the visible branching fraction in a given process and ε^{TOTAL} contains the product of all relevant efficiencies: the LHC*b* acceptance, trigger, reconstruction, stripping and final selection ones.

The search for $X_b \to K^-\mu^+$ decay involves primarily the tracking and the muon systems of the LHC*b* spectrometer, combined with both hardware and software triggers. A distinctive advantage of muon as a final state particle is the fact that they travel all the way through the detector (to the outermost muon system), so the detector can trigger on the muons and measure their transverse momenta with a good precision (see Sec. 4.2.1.6). Furthermore, the PID system provides efficient distinction among kaons, protons and pions (see Sec. 4.2.1.4), which is crucial to distinguish final states of otherwise identical topology.

Introducing the $\Lambda_b \to pK^-$ normalization channel, the branching fractions can be extracted from:

$$\mathcal{B}(\Lambda_b \to K^-\mu^+) = \frac{N(\Lambda_b \to K^-\mu^+)}{N(\Lambda_b \to pK^-)} \times \frac{\varepsilon^{TOTAL}_{\Lambda_b \to pK^-}}{\varepsilon^{TOTAL}_{\Lambda_b \to K^-\mu^+}} \times \mathcal{B}(\Lambda_b \to pK^-), \tag{5.2}$$

$$\mathcal{B}(\Xi_b^0 \to K^-\mu^+) = \frac{f_{\Lambda_b}}{f_{\Xi_b^0}} \times \frac{N(\Xi_b^0 \to K^-\mu^+)}{N(\Lambda_b \to pK^-)} \times \frac{\varepsilon^{TOTAL}_{\Lambda_b \to pK^-}}{\varepsilon^{TOTAL}_{\Xi_b^0 \to K^-\mu^+}} \times \mathcal{B}(\Lambda_b \to pK^-), \tag{5.3}$$

where the latter contains an extra factor related to the b hadronization proportionality between signal and normalization channels.

The determination of the ratio of the efficiencies with respect to the normalization channel in the above equations may be decomposed into six factors:

$$\frac{\varepsilon^{TOTAL}_{\Lambda_b \to pK^-}}{\varepsilon^{TOTAL}_{X_b \to K^-\mu^+}} = \frac{\varepsilon^{GEN}_{\Lambda_b \to pK^-}}{\varepsilon^{GEN}_{X_b \to K^-\mu^+}} \times \frac{\varepsilon^{REC/GEN}_{\Lambda_b \to pK^-}}{\varepsilon^{REC/GEN}_{X_b \to K^-\mu^+}} \times \frac{\varepsilon^{STRIP/REC}_{\Lambda_b \to pK^-}}{\varepsilon^{STRIP/REC}_{X_b \to K^-\mu^+}} \times \frac{\varepsilon^{TRIG/SEL}_{\Lambda_b \to pK^-}}{\varepsilon^{TRIG/SEL}_{X_b \to K^-\mu^+}} \times \frac{\varepsilon^{PID}_{\Lambda_b \to pK^-}}{\varepsilon^{PID}_{X_b \to K^-\mu^+}} \times \frac{\varepsilon^{BDT/PID}_{\Lambda_b \to pK^-}}{\varepsilon^{BDT/PID}_{X_b \to K^-\mu^+}}, \tag{5.4}$$

where different terms refer subsequently to the efficiencies related to the LHCb acceptance, reconstruction, stripping, specific trigger lines over selected signal events, PID criteria and multivariate selection.

The analysis has been performed in a blind approach, *i.e.* without looking at the relevant data distributions during the process of analysing data. It is the optimal way in search analysis to reduce or even eliminate the experimenter's bias, *i.e.* the unintended influence on a result in a certain direction. The implementation of a blind analysis relies on hiding ("closing in the box") signal regions around known masses of mother particles. Any events in the signal regions are kept hidden until the analysis sequence, selection requirements and background estimations are fixed. Since the selection is fully developed and checked, the signal box could then be opened and examined ("opening the box").

The dedicated stripping selection is used and it selects events with the Λ_b absolute mass difference to the Particle Data Group (PDG) reference value, $m_{\Lambda_b,PDG} = 5619.5\,\mathrm{MeV}/c^2$ [1], to be lower than $500\,\mathrm{MeV}/c^2$. The distribution of $K\mu$ invariant mass is divided into the following regions:

- Λ_b signal region: $\mid m_{K\mu} - m_{\Lambda_b,PDG} \mid < 50\,\mathrm{MeV}/c^2$,
- Ξ_b^0 signal region: $\mid m_{K\mu} - m_{\Xi_b^0,PDG} \mid < 50\,\mathrm{MeV}/c^2$,
- middle-sideband region: $m_{K\mu} > 5670\,\mathrm{MeV}/c^2$ and $m_{K\mu} < 5740\,\mathrm{MeV}/c^2$,
- lower-sideband region: $m_{K\mu} < 5570\,\mathrm{MeV}/c^2$,
- upper-sideband region: $m_{K\mu} > 5840\,\mathrm{MeV}/c^2$.

Since both signal regions are kept blinded on data until the analysis strategy is ready and checked, the background expectation is compared with the actual event count. All sideband regions are then used to fit the background spectra and obtain an expectation of the background yield in the signal regions.

The data collected in 2011 and 2012 are processed individually, which is justified by different LHC running conditions, see Tab. 4.1. The selection optimization takes as a starting point signal MC events passing trough the dedicated stripping lines as well as the data samples processed with the same sign of the daughters hypothesis. In this manner the full data sample of the correct sign is actually used to perform the search.

In addition, $B^0 \to K^+\pi^-$ and $B^- \to J/\psi K^-$ decays are used as the control modes to verify various stages of the selection, in particular the trigger and particle identification efficiencies.

5.2 Data and Monte Carlo samples

The study described in this thesis uses LHC*b* data in pp collisions collected in the years 2011 and 2012 (*cf.* Fig.4.4). The integrated luminosities of $1.1\,\text{fb}^{-1}$ and $2\,\text{fb}^{-1}$ are recorded at centre-of-mass energy $7\,\text{TeV}$ and $8\,\text{TeV}$, respectively. The technical specification of the samples processing chain within the LHC*b* framework can be found in Appendix A.0.3.

A full event and detector simulation is used for signal and background studies, and also to estimate the generator and reconstruction efficiency. The MC simulation samples employed in this search can be divided into three classes: signal, normalization/control and physics backgrounds. All these samples are produced centrally and are processed in the same manner as real data, starting from LHC*b* reconstruction stage.

During the event simulation the products of decays are required to have their momentum vectors pointing at the angular acceptance of LHC*b*. This requirement is known as the generator level cut. Only events that pass this requirement are saved and subsequently reconstructed. As this study involves data samples collected in 2011 and 2012 datasets, the MC sets of samples were also created under these two run period conditions, as summarized in Tab. 5.2. Apart from the difference in the centre-of-mass energy ($7\,\text{TeV}$ vs $8\,\text{TeV}$), the beam conditions varied in the z-position of the PV and crossing angle. Moreover, during the data taking the LHC*b* detector was using different trigger configurations to select events of interest that are identified by different TCKs (see Sect.4.2.2). In the MC production the trigger conditions were emulated using the TCKs that were chosen to describe the most common trigger conditions throughout the respective year. For this reason all efficiencies are needed to be given separately for 2011 and 2012 MC.

TABLE 5.2: Experimental conditions relevant for MC simulations.

Year	Energy [TeV]	$z_{\text{PV}}[mm]$	crossing angle in $x(y)$ coordinate [mrad]
2011	3.5	0.5	$-0.520(0)$
2012	4	25.7	$0.236(0.100)$

The complete list of MC samples used in this study can be found in Tab. 5.3. The modes indicated as background channels are considered from the point of view of possible influence of particle misidentification on invariant mass spectrum. Because of the wrong mass hypothesis for at least one of the tracks, the reconstructed invariant mass is shifted (the so-called reflection) and could possibly peak in the proximity of the Λ_b and Ξ_b masses. As follows, a number of b-hadron decays are reconstructed with the $K\mu$ mass hypothesis in order to assess the background contamination in the signal mass regions.

TABLE 5.3: MC simulation samples used for the analysis of data collected in 2011 and 2012. All samples are approximately a $1:1$ mix of magnet-up and magnet-down detector setups.

	Number of events	
	2011	2012
Signal channels:		
$\Lambda_b \to K^-\mu^+$	318,861	276,400
$\Xi_b^0 \to K^-\mu^+$	334,028	315,827
Normalization/Control channels:		
$\Lambda_b \to pK^-$	775,995	1,513,745
$B^0 \to K^+\pi^-$	268,999	531,995
$B^- \to J/\psi K^-$	1,514,494	5,047,185
Background channels:		
$\Lambda_b \to pK^-$	775,995	1,513,745
$B^0 \to K^+\pi^-$	268,999	531,995
$B^0 \to \pi^+\pi^-$	1,160,495	3,067,742
$B_s^0 \to K^-\pi^+$	1,514,494	3,071,739
$B_s^0 \to K^+K^-$	1,532,248	3,052,242
$\Lambda_b \to p\pi^-$	764,750	1,475,492

5.3 Event selection and signal classification

The Λ_b and Ξ_b candidates are reconstructed from two oppositely charged long tracks, where one track is identified as a kaon and the other one as a muon. Owing to the vast amount of background falling in the signal mass window, the selection of these decays is challenging and employs the stripping, trigger and offline selection. To deal effectively with random combinations of track pairs and backgrounds from reflections, a number of variables are used.

In the following section, the variables used in the selection are defined. Afterwards, the stripping requirements and explicit trigger lines are indicated. As a central part, the way of signal and background discrimination including multivariate selection is described. Finally, the background studies and final selection optimization followed by the determination of systematic uncertainties are listed.

5.3.1 Variables used in the selection

The topology of $X_b \to K^- \mu^+$ decay with an illustration of the relevant concepts and parameters is sketched in Fig.5.1. The heavy baryon is produced in the collision of two very high energy protons from the LHC at a location marked as *Primary Vertex*, together with many other particles (shown in grey). After travelling *Flight Distance* this baryon decays into a kaon and muon at a place marked as *Secondary Vertex*. The muons and kaons are traversing the LHC*b* detector where the tracking system is used to reconstruct their trajectories with such a very high precision that it is that clear they do not come from the primary vertex. The fact that the reconstructed tracks do not cross exactly in two points reflects the experimental precision of computer reconstruction. To quantify this issue, the auxiliary variable of impact parameter (IP), the direction angle (DIRA) and the distance of the closest approach (DOCA) are computed. Below, a full list of variables that are used in this study to distinguish the signal from background is given.

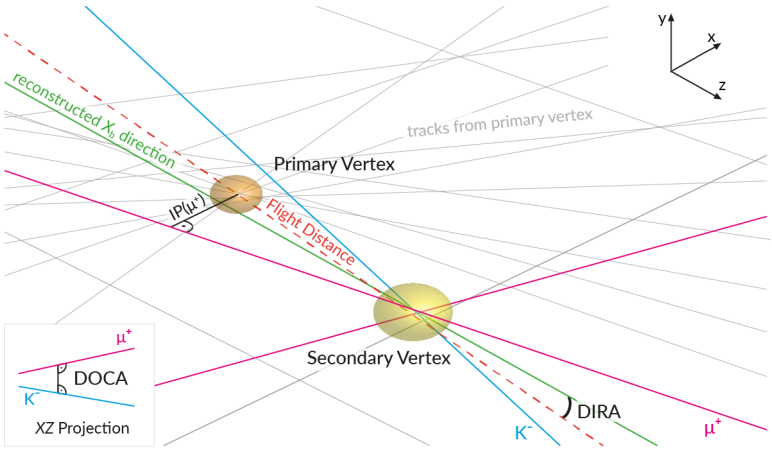

FIGURE 5.1: Illustration of Λ_b decay to a kaon and a muon at the secondary vertex. Basic variables used in the selection are sketched.

Kinematic variables

- ΔM: the difference between the reconstructed mass of an intermediate particle and the world average mass value from PDG [1];
- τ: the proper lifetime of the particle;
- p: the momentum of the particle;
- p_{T}: the momentum of the particle in the plane transversal to the beam direction;
- η: the pseudorapidity of the particle: $\eta = -\ln(\tan\theta/2) = 1/2 \cdot \ln\left(\frac{p+p_{\mathrm{L}}}{p-p_{\mathrm{L}}}\right)$, where θ is the polar angle with respect to the beam axis, p_{L} is the *longitudinal* momentum and p is the momentum of the particle;

Geometric variables

- Impact Parameter, IP: the minimum distance between the PV and particle trajectory;
- $\chi^2(\mathrm{IP})$: the χ^2 of the IP, the PV with the smallest $\chi^2(\mathrm{IP})$ value is considered as the best primary vertex (BPV);
- Flight Distance (FD): the distance between the BPV and the decay vertex;
- $\chi^2(\mathrm{FD})$: the χ^2 of the flight distance;
- DIRA: the angle between the reconstructed momentum of the particle and its direction of flight from the BPV to the decay vertex;
- $\chi^2_{\mathrm{DOF}}(\mathrm{Vtx})$: the χ^2 of the decay vertex fit over the degrees of freedom;

Track variables

- $\chi^2_{\mathrm{DOF}}(\mathrm{Tr})$: The χ^2 of the track fit over the degrees of freedom;
- $\mathrm{P(Gh)}$: The probability that a track is a ghost[15];
- PID variables:
  - $\mathrm{DLL_{X\pi}}$: the delta log likelihood value for a certain particle hypothesis X with respect to the pion hypothesis, as defined in Sec.4.2.1.4;
  - ProbNN_X: the output of the neural network based on the evaluation of the likelihood that the track is a particle of type x $= \{e, \mu, \pi, K, p\}$, as defined in Sec.4.2.1.4.

Isolation variables[16]

- $\mathrm{Iso_{CDF}}$: the CDF isolation [100], defined as follows:

$$I_{CDF} = \frac{p_{\mathrm{T}}(\Lambda_b)}{p_{\mathrm{T}}(\Lambda_b) + \sum_{\mathrm{track}} p_{\mathrm{T}}(\mathrm{track})},$$

  where $p_{\mathrm{T}}(\Lambda_b)$ is the transverse momentum of the Λ_b candidate. The summation is made over all other tracks for which the condition $\sqrt{\delta\eta^2 + \delta\phi^2} < 1.0$ is satisfied, where $\delta\eta$ and $\delta\phi$ are respective differences in the pseudorapidity and the polar angle ϕ between the track and the Λ_b candidate;
- Iso5: the number of non-isolated tracks for a given track in a cone, ignoring the other tracks in the subsequent decay chain.

[15] The ghost particle is a wrongly reconstructed track which combines hits that are not left by the same particle.

[16] They measure the level of geometrical separation of the given particle with respect to the others.

In addition, the maximum of distance of the closest approach between two daughter particles and the track multiplicity (N_{track}), which is the number of unique tracks measured in an event in VELO, are defined.

5.3.2 Stripping selection

As mentioned in Sec. 4.2.2, each stripping processing has its unique number. The detailed specification of the stripping lines used in this study may be found in Appendix A.0.3, while the exact selection criteria defined within these lines are reported in Tab.5.4. All lines have very similar selection criteria and are identical to 2011 and 2012 data. In this stripping selection, the first step after prerequisite PID cuts are the requirements on the tracks and their combinations. The latter, labelled as *TrackCuts* and *CombinationCuts* were applied to the vertex fit. The selection applied after the vertex fit is called *MotherCuts*.

TABLE 5.4: Stripping selections criteria for given channels.

Decay channel:	$X_b \to K^-\mu^+$	$\Lambda_b \to pK^-$	$B^0 \to K^+\pi^-$	$B^- \to J/\psi\ (\mu^+\mu^-)K^-$
ParticleIdentificationCuts:				
Daughter#1	$\text{DLL}_{K\pi} > 0$	–	$\text{DLL}_{K\pi} > -5$	–
Daughter#2	$IsMuon = \text{true}$	–	–	$IsMuon = \text{true}$
Daughter#3	n/a	n/a	n/a	$IsMuon = \text{true}$
TrackCuts:				
p_{T}	$> 250\,\text{MeV}/c$	$> 250\,\text{MeV}/c$ and $< 40\,\text{GeV}/c$		$> 250\,\text{MeV}/c$
p	–	$< 500\,\text{GeV}/c$		–
$\chi^2(\text{IP})$	> 25	> 25		> 25
$\chi^2_{\text{DOF}}(\text{Tr})$	< 3	< 3		< 3
P(Gh)	< 0.3	< 0.3		–
CombinationCuts:				
DOCA	$< 0.3\,\text{mm}$	$< 0.3\,\text{mm}$		$< 0.3\,\text{mm}$ for J/ψ selection
MotherCuts:				
ΔM	$< 500\,\text{MeV}/c^2$	$< 500\,\text{MeV}/c^2$		$< 500\,\text{MeV}/c^2$ and $< 100\,\text{MeV}/c^2$ for J/ψ selection
p_{T}	–	$> 350\,\text{MeV}/c$		–
τ	–	$< 13.248\text{ps}$		–
DIRA	> 0	> 0		> 0 for J/ψ selection
$\chi^2_{\text{DOF}}(\text{Vtx})$	< 9	< 9		< 45 and < 9 for J/ψ selection
$\chi^2(\text{IP})$	< 25	< 25		< 25 and < 25 for J/ψ selection
$\chi^2(\text{FD})$	> 100	> 225		> 169 for J/ψ selection

5.3.3 Prompt trigger lines

An explicit requirement is made on each trigger level. In this search the most relevant LHC*b* triggers are those focusing on hadronic and muon final states with a two prong track topology. Tables 5.5 and 5.6 list the benefits from each chosen trigger line, where the last raw in each trigger level stands for the

efficiency taken as the sum of all specified lines, in which the indicated errors are binomial ones. These efficiencies are determined on the signal MC true matched events which have passed the dedicated stripping line. Going from stripping $\to$ L0 $\to$ HLT1 $\to$ HLT2, at the former trigger level, the logical sum from selected lines decision is required. The listed lines have been found to be most efficient on the signal channel - the other tested trigger lines bring no extra bandwidth.

At the L0 level the `L0Hadron` is used which is based on signatures in the calorimeter system and sets up the E_T threshold. The second line used is the `L0Muon`, based on a standalone track reconstructed in the muon system with the requirement for p_{T} to be larger than $1.468\,\mathrm{GeV}/c$. In addition, `L0Global` line is chosen, which performs general selection of candidates which are accepted by any L0 line. At the HLT1 trigger level the topological lines are used (`Hlt1TrackAllL0`, `Hlt1TrackMuon`) where the decision depends on *e.g.* quality of the reconstructed tracks. The chosen HLT2 lines introduce multivariate training to make a decision (`Hlt2Topo2BodyBBDT`, `Hlt2TopoMu2BodyBBDT`).

All lines are required to be `TOS` except for `L0Global`, for which the `TIS` flag is used. This has been done on the L0 level to enhance the sample while discarding candidates passing the non-hadronic and non-muon triggers. This increases the L0 efficiency for a combined L0 trigger stage to the level of about 92% (89%) in 2011 (2012) data sample, where the `L0Global_TIS` requirement increases the efficiency of about 4%. As it may be seen in the tables below, by adding the `L0Global_TIS` a higher gain on control channels ($\sim$15%) is achieved. The combination of all trigger levels (L0&HT1&HLT2) gives the efficiency of 65.20% and 71.41% for the signal for 2011 and 2012 MC datasets, respectively. As expected, the muon type lines are of minor importance for the control and normalization channels, where the same set of trigger lines are used to keep the selection strategy as similar as possible. They give comparable but slightly lower overall efficiency, staying anyway at the reasonable level above 40%.

TABLE 5.5: The trigger efficiencies listed for 2011 datasets of signal and control channels. For a given trigger level a final decision is taken as the logical sum of all specified lines, while among levels a logical conjunction is used.

Trigger stage	Trigger line	$\varepsilon^{Trig/Strip}_{\Lambda_b\to K^-\mu^+}$ [%]	$\varepsilon^{Trig/Strip}_{B^0\to K^+\pi^-}$ [%]	$\varepsilon^{Trig/Strip}_{\Lambda_b\to pK^-}$ [%]
L0	`L0MuonDecision_TOS`	81.11 ± 0.12	1.14 ± 0.06	0.82 ± 0.02
	`L0HadronDecision_TOS`	28.61 ± 0.14	49.29 ± 0.27	48.26 ± 0.12
	$\hookrightarrow$ `Sum of L0Muon and L0Hadron`	88.78 ± 0.09	50.13 ± 0.27	48.86 ± 0.12
	`L0Global_TIS`	32.84 ± 0.14	32.11 ± 0.25	33.11 ± 0.11
	$\hookrightarrow$ `Sum of all selected L0 lines`	92.21 ± 0.08	64.86 ± 0.26	64.50 ± 0.11
HLT1	`Hlt1TrackAllL0_TOS`	75.64 ± 0.13	52.87 ± 0.27	53.49 ± 0.12
	`Hlt1TrackMuon_TOS`	67.13 ± 0.14	0.77 ± 0.05	0.54 ± 0.02
	$\hookrightarrow$ `Sum of all selected HLT1 lines`	81.60 ± 0.12	52.95 ± 0.27	53.55 ± 0.12
HLT2	`Hlt2Topo2BodyBBDT_TOS`	56.95 ± 0.15	41.86 ± 0.26	42.01 ± 0.12
	`Hlt2TopoMu2BodyBBDT_TOS`	65.20 ± 0.15	0.96 ± 0.05	0.69 ± 0.02
	$\hookrightarrow$ `Sum of all selected HLT2 lines`	65.20 ± 0.15	41.92 ± 0.26	42.07 ± 0.12

TABLE 5.6: The trigger efficiencies listed for 2012 datasets of signal and control channels. For a given trigger level a final decision is taken as the logical sum of all specified lines, while among levels a logical conjunction is used.

Trigger stage	Trigger line	$\varepsilon^{Trig/Strip}_{\Lambda_b\to K^-\mu^+}$ [%]	$\varepsilon^{Trig/Strip}_{B^0\to K^+\pi^-}$ [%]	$\varepsilon^{Trig/Strip}_{\Lambda_b\to pK^-}$ [%]
L0	`L0MuonDecision_TOS`	77.48 ± 0.14	0.96 ± 0.05	0.74 ± 0.02
	`L0HadronDecision_TOS`	26.98 ± 0.15	45.48 ± 0.27	44.74 ± 0.12
	↪ `Sum of L0Muon and L0Hadron`	85.96 ± 0.12	46.21 ± 0.27	45.29 ± 0.12
	`L0Global_TIS`	31.61 ± 0.16	30.40 ± 0.24	31.49 ± 0.12
	↪ `Sum of all selected L0 lines`	89.96 ± 0.11	61.38 ± 0.26	61.16 ± 0.12
HLT1	`Hlt1TrackAllL0_TOS`	72.84 ± 0.15	49.29 ± 0.27	49.89 ± 0.12
	`Hlt1TrackMuon_TOS`	66.97 ± 0.16	0.73 ± 0.01	0.52 ± 0.01
	↪ `Sum of all selected HLT1 lines`	80.51 ± 0.14	49.43 ± 0.27	49.97 ± 0.12
HLT2	`Hlt2Topo2BodyBBDT_TOS`	62.96 ± 0.17	43.75 ± 0.27	43.53 ± 0.12
	`Hlt2TopoMu2BodyBBDT_TOS`	71.41 ± 0.15	0.89 ± 0.05	0.67 ± 0.02
	↪ `Sum of all selected HLT2 lines`	71.41 ± 0.15	43.81 ± 0.26	43.58 ± 0.12

5.3.4 MVA classification

To discriminate the signal from background in the sample that passed the above mentioned stripping and trigger criteria, the probability of being signal- or background-like is attributed to each event. The determination of such a probability is performed using a multivariate analysis classifier (MVA) [101], which uses the multi-dimensional observable space rather than each observable separately. Obviously, sequential requirements on each observable are not able to exploit possible correlations among different observables. Therefore, the MVA techniques give better performance in terms of higher efficiency for the same misclassification rate.

Two types of dedicated MVA discriminants are built on topological variables and PID information from different detector sub-systems. The first one has been developed by the Author of this thesis while the latter one is provided by the DAVINCI package [78] and is trained by the respective PID working group of the LHC*b* collaboration [102]. The detail features of both discriminants are given below.

5.3.4.1 Boosted Decision Tree classifier

The selection described in this section has been developed following the MVA methods implemented in the TMVA package [103]. The Boosted Decision Tree (BDT) discriminant [104, 105] has been constructed as the one which gives a high background rejection across a wide range of signal efficiencies, *i.e.* this approach gives the best performance as compared to other MVA methods. BDT combines many different *decision trees*, which together form a *forest*. In this procedure different *boost recipees* can be adopted. In this studies the so-called ADABOOST (adaptive boost) algorithm [106] is used.

The training of the classifier

For the multivariate approach, the data sample is split into training and testing samples where the class membership of the events is known. To train the BDT a data-driven approach is employed for the combinatorial background representation, while the MC sample is used for the signal. The 2012 data sample reconstructed with the same sign (SS), namely the $\Lambda_b \to K^+\mu^+$, is used as a source of background distributions for the training. For testing of the background category the middle and upper 2012 data sidebands are used. The comparison of invariant mass distribution from the data sidebands and SS data is presented in Fig. 5.2. For the signal training and testing samples, the $\Lambda_b \to K^-\mu^+$ MC is split in half. Each of these halves consists of equal parts of magnet up and magnet down events. All events of the BDT input samples pass the stripping and prompt trigger requirements indicated in Sect. 5.3.2, 5.3.3. However, there is no PID criteria on the simulated samples required in order to keep the similarity of the signal, control and normalization channels, to which the resulting BDT discriminant is applied.

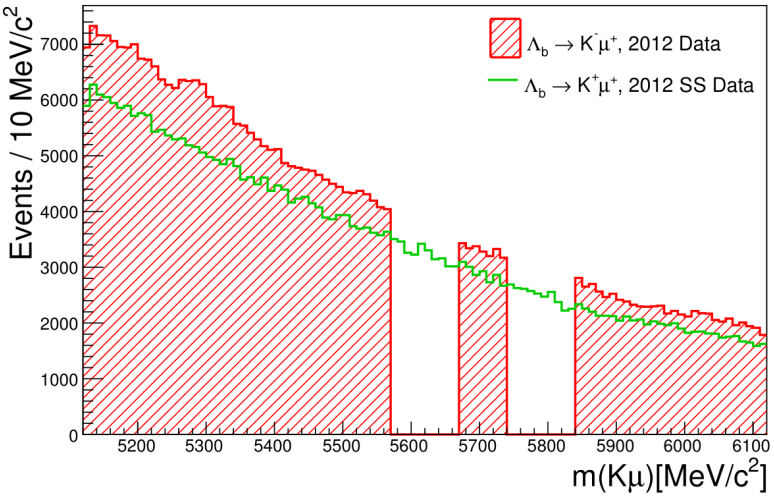

FIGURE 5.2: The comparison of data sidebands and the same sign Kμ combination of 2012 data after the stripping and trigger requirements.

The BDT classifier is designed to suppress combinatorial background and is based on the kinematic and geometric variables with the best separation power. The list of input BDT variables is given in Tab. 5.7.

TABLE 5.7: Input variables to the BDT method. Their definitions are provided in the text.

Mother particle:	Daughter particles:
χ^2 (IP)	Max(χ^2 (Tr)/DOF)
χ^2 (FD)	Max(IP)
χ^2 (Vtx)/DOF	Max(Iso5)
DIRA	DOCA
$\mathrm{Iso}_{\mathrm{CDF}}$	Min(p_{T})
p_{T}	

In fact, the choice of discriminating observables is vital, and special care should be taken to remove variables which do not give additional information. The linear correlation coefficients for input variables have been studied for signal and background samples. Fig.5.3 presents linear correlations for the set of input variables that defines the final BDT discriminant. It is clearly visible that there is a strong linear correlation between DOCA and $\chi^2(\Lambda_b, \mathrm{Vtx})/\mathrm{DOF}$ variables reaching $78\%(80\%)$ for the signal (background). Since the decision trees are mostly inert against useless variables, the impact on the BDT performance resulting from removing one of these two variables has been verified. However, the BDT with both mentioned variables is found to be the most robust one.

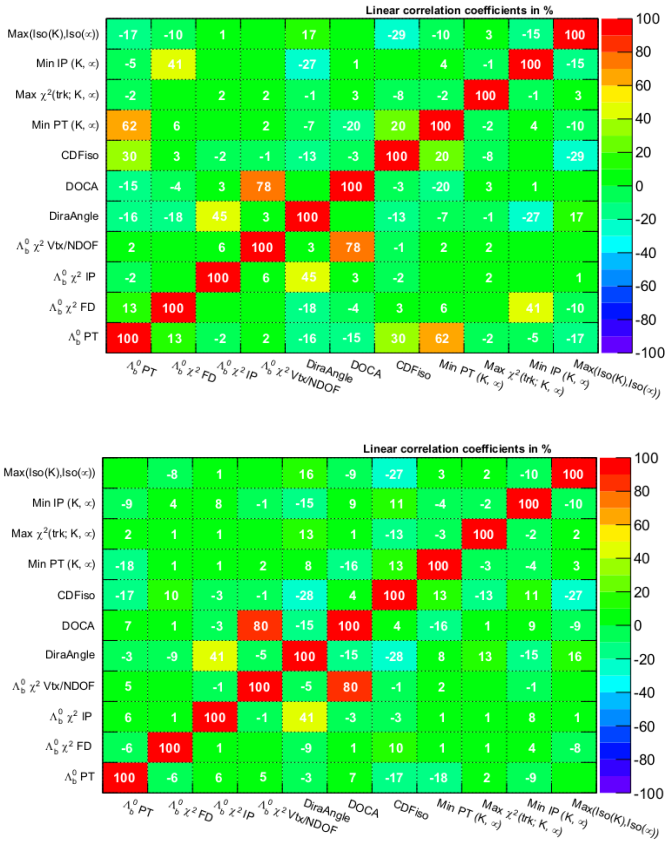

FIGURE 5.3: The linear correlation coefficients of BDT input variables for signal (top) and background (bottom) samples.

Following the BTD training on simulated events, the distributions of the key variables have been verified on the control channel which is kinematically similar to the signal one. The distributions are extracted from the control channel on data and compared to the ones simulated on MC. The details are given in Sect. 5.4. By studying the input variables in one-dimensional projections, some MC/Data discrepancies have been spotted. Since the MVA selection tries to disentangle complicated correlations among the observables, it is more prone to systematic uncertainties owing to a possible mismodelling of these correlations. However, the MVA output distributions clearly show differences among the data that differ in the correlations. Hence, it is easy to spot systematic differences between the data and the simulation in the MVA analysis by comparing the MVA outputs. On the basis of this fact the calibration has to be performed.

In addition, the BDT method has to be protected against overtraining, which occurs when the discriminant is determined to recognized statistical fluctuations of the training sample. For this purpose the performance of both the training and testing samples has been compared, since any difference among the results can indicate the overtraining.

Apart from the aforementioned MVA training issues there is a possibility to modify the internal training parameters of the chosen classifier. For example, the optimal tree depth depends on the degree of correlations between variables, hence it should be optimized for each case. The other parameters taken for the optimization are the number of trees in the forest, the minimum number of training events in a leaf node and the number of steps during the optimization of the number of nodes. The parametric scan has been performed, where a given set of values for the internal parameters was considered as the best one if the signal efficiency had the highest value at the level of 99% of background rejection.

Performance of the trained classifier

Apart from the input variables, the choice of the classifier is crucial. Since the best choice is not always obvious, the comparison of the performance of different classification techniques on the same sample has been performed. It has been visualised with the Receiver Operating Characteristics (ROC) curves that may be seen in Fig. 5.4. The BDT classifier is compared to another commonly used classifier techniques: BDT with the gradient boost algorithm (BDTG), k-nearest neighbour discriminant (KNN) and 1-dimensional likelihood discriminant with decorrelated input variables (LikelihoodD). The BDT classifier has been chosen as the one yielding the best performance for the present search.

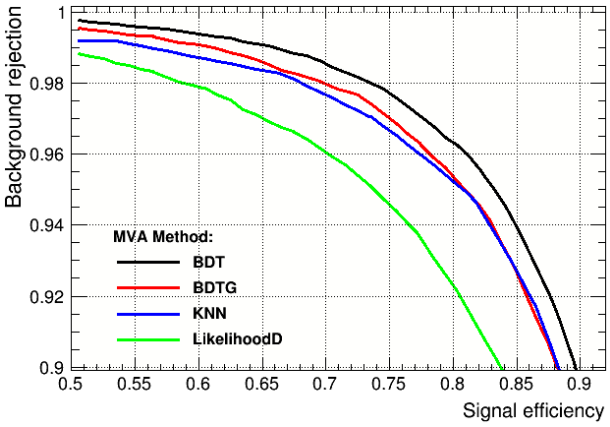

FIGURE 5.4: Receiver Operating Characteristics for trained classifiers. The names of the classifiers are explained in the text.

The BDT response for signal and background training samples superimposed with testing samples is presented in Fig. 5.5, while the overall performance of the final BDT classifier for different channels is compiled in Fig. 5.6. As it may be seen, the BDT operand exhibits a similar performance on control and normalization channels, being also close to the one for the signal channels. In addition, the BDT discriminant gives a comparable performance on both 2011 and 2012 datasets.

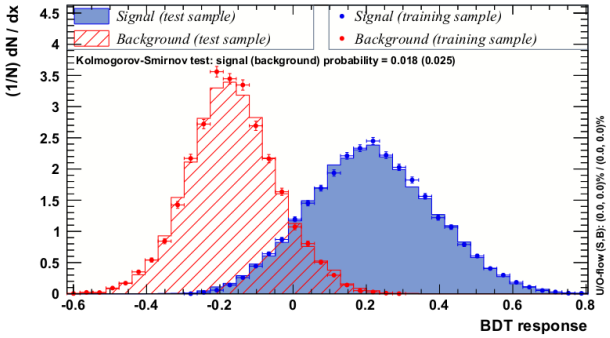

FIGURE 5.5: The BDT discriminant response on training and testing samples

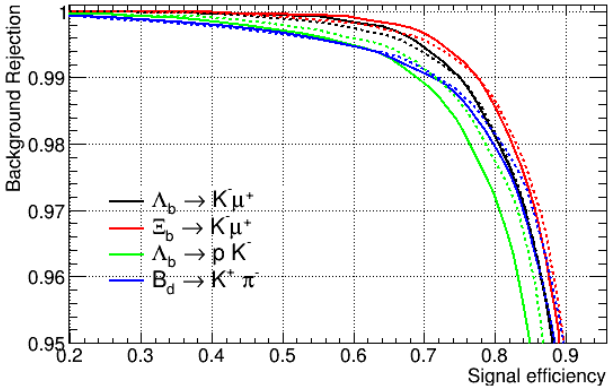

FIGURE 5.6: Performance of the BDT classifier for different channels. The dashed lines indicate the ROC curves obtained for 2011 dataset while the solid lines for 2012 one.

5.3.4.2 Calibration of the BDT classifier response

Following the differences in the distributions of the BDT response for MC and data, the BDT selection efficiency obtained from simulated events might be overestimated. Such an effect is studied in Sect. 5.4.3. As a consequence, the BDT response on MC events is needed to be calibrated to the data. The control channel is used as a reference sample, relying on its topological similarity. The discrepancy between the data and simulation is assumed to be the same comparing the reference and signal channels. The BDT PDFs obtained from fitting to the BDT response distribution of $sWeighted$[17] $B^0 \to K^+\pi^-$ data and MC allow the extraction of the BDT weight for a given selection requirement ($BDT > x$) according to the relation:

$$\varepsilon^{MCcalib}_{\Lambda_b\to K^-\mu^+}(BDT > x) = \frac{\varepsilon^{Data}_{B^0\to K^+\pi^-}(BDT > x + a)}{\varepsilon^{MC}_{B^0\to K^+\pi^-}(BDT > x + a)} \cdot \varepsilon^{MC}_{\Lambda_b\to K^-\mu^+}(BDT > x). \quad (5.5)$$

Using the above formula, the shift (a) between the signal and simulated reference distribution is handled. The BDT responses on simulated samples are then calibrated event-by-event using the corresponding weight. The results of the calibration procedure may be seen in Fig.5.7.

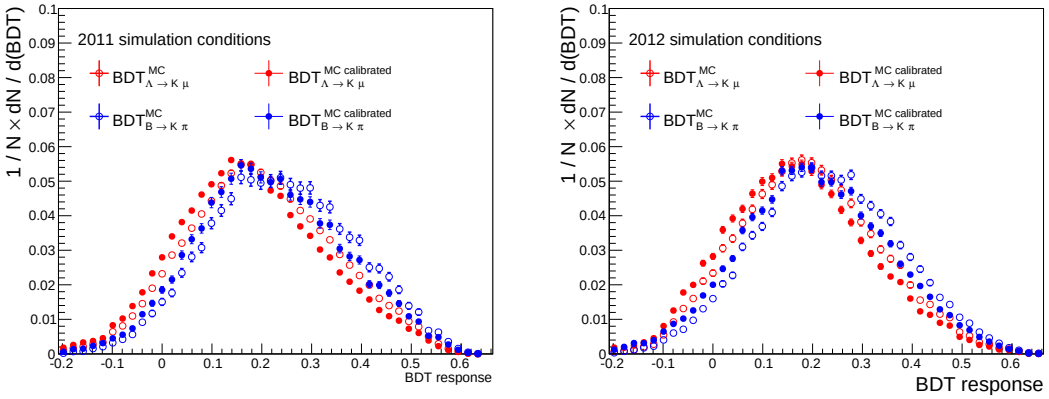

FIGURE 5.7: The BDT response for 2011 (left) and 2012 (right) MC samples. The distributions before and after the calibration for signal and control samples are showed.

5.3.4.3 Calibration of the ProbNN_X classifier response

The powerful PID selection is being used for reducing the potential sources of background that come from misidentification of one or both daughter particles. The optimization of the PID selection criteria relies on ProbNN_μ and ProbNN_K distributions. There is one classifier for each particle hypothesis distributed between 0 and 1. For a given particle hypothesis it is peaked at 1, while the distributions for all other hypotheses are peaked at 0.

Since the classifier is determined on the basis of not perfect simulation, it needs to be calibrated. There are two approaches associated with this issue,

[17] The so-called sWeight arises from the ${}_s\mathcal{P}\mathrm{lot}$ technique [107], as described in Appendix C.0.1

both relying on the phase space binning in transverse momentum, multiplicity and pseudorapidity of the daughters. Then, the calibration is performed as an evaluation of the efficiency for a given PID requirement or correcting the ProbNN_X distribution in the simulated samples, which are both used in the case of this analysis.

To perform the PID calibration, all considered MC signal modes were prepared without any PID requirements. This was done on special data samples available within the `PIDCalib` framework. Using such samples for each track in the signal MC, the efficiency to pass the given PID requirements is evaluated and averaged over the whole phase space. In addition, the corrected ProbNN_X distributions as a function of definite kinematic variables are obtained. The results of the calibration procedure may be seen in Fig.5.8.

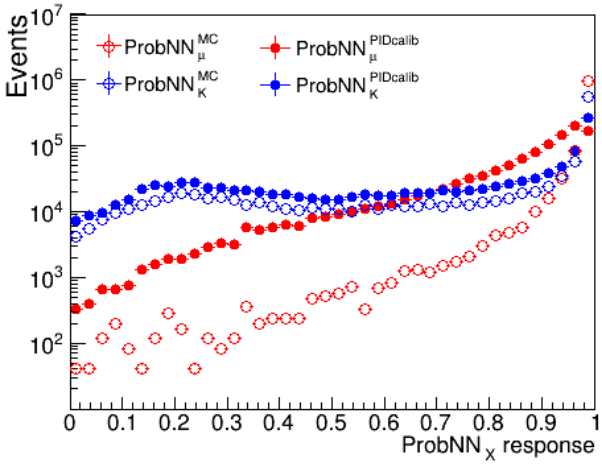

FIGURE 5.8: The ProbNN_X classifier responses for MC and calibrated samples for 2012 data and simulation.

5.3.4.4 MVA discriminants and invariant mass correlation

Since the strategy of this study relies on the determination of the number of expected background events by looking at invariant mass variable with the requirement set on MVA responses, it is relevant to verify whether these variables are uncorrelated. The average MVA response over invariant mass for three different discriminants is plotted in Fig. 5.9. As it has been shown, the final constructed discriminant variables are not correlated with the invariant mass variable.

It is expected that the performance of the ultimate selection is entangled with each of the defined MVA classifiers. In this way the optimization of the final selection is performed relying on simultaneous a parametric scan, which is described in the following section.

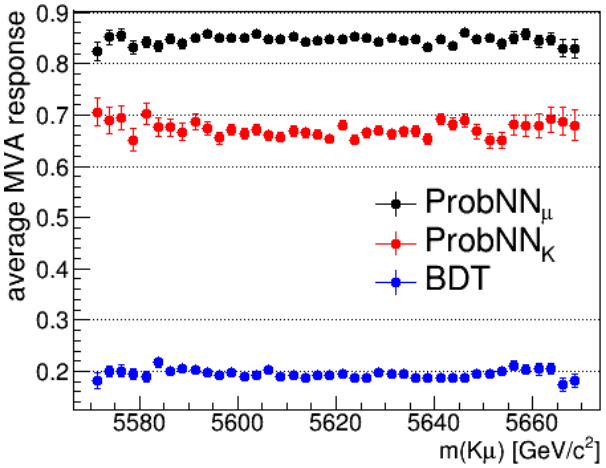

FIGURE 5.9: The average response of the MVA discriminants over invariant mass for the signal channel of MC 2012. Error bars stand for standard error of the mean.

5.3.4.5 The optimization of the MVA selection

To evaluate the levels of consistency of the data samples with background b and signal plus background $\mathrm{s}+\mathrm{b}$ hypotheses, the samples of the selected signal candidates are analyzed, where 2011 and 2012 data samples are treated as two independent bins for the confidence level computation [108]. To determine the maximum sensitivity point of the measurement, an event selection has been optimized using CL_s technique, described in Appendix C.0.2.

The selection is optimized in a three-dimensional space of MVA classifiers (ProbNN_μ, ProbNN_K and BDT) simultaneously. The parametric scan has been performed with an upper limit at 90% confidence level used as the figure of merit. The number of expected background events for the CL_s evaluation is estimated using the SS data sample, on which the $\varepsilon^{Bgd}_{Selection}$ is determined. The subscript $Selection$ stands for the ProbNN_μ, ProbNN_K and BDT requirements, varying in steps. Then the expected background yields within the signal regions read:

$$N^{Bgd}_{\Lambda_b,\Xi^0_b} = \varepsilon^{Bgd}_{Selection} \times N^{Bgd}_{init}, \tag{5.6}$$

where the N^{Bgd}_{init} stands for the initial number of expected background events, determined from the middle and upper data sidebands. The signal efficiency is taken from the corresponding MC simulation, calibrated to data, as it has been described in the previous section. The outcome of this procedure is indicated in Tab.5.8.

TABLE 5.8: The optimized offline selection requirements obtained from parametric scan performed for $X_b \to K^-\mu^+$ sample.

Dataset	BDT	ProbNN_K	ProbNN_μ
2011	> 0.22	> 0.45	> 0.45
2012	> 0.22	> 0.65	> 0.55

5.4 Studies on control channels

The measurement of the branching fraction of $\Lambda_b \to K^-\mu^+$ has been performed relative to that of the normalization channel $\Lambda_b \to pK^-$. In addition, the supplementary studies have been performed relying on two extra control channels, namely $B^0 \to K^+\pi^-$ and $B^- \to J/\psi\, K^-$.

In fact, the control channel $B^0 \to K^+\pi^-$ is kinematically very similar to the signal mode and much more abundant when compared to the normalization mode. Hence, the use of such a control channel is twofold. First, the efficiency of each step of the selection could be verified, where possible MC/data discrepancies could be estimated and the calibration might be performed. Then, the direct double-check of the correctness of the selection could be completed using the $B^0 \to K^+\pi^-$ sample, since its exact branching fraction is known.

The other control channel, $B^- \to J/\psi\, K^-$, has been selected to get an additional insight into the analysis aspects related to muon selection. The offline selection requirements indicated in Tab. 5.9 have been defined for the control channels as the ones that give a higher signal purity.

TABLE 5.9: The offline requirements for event selection of the control channels.

Channel	BDT	ProbNN_K	ProbNN_π	ProbNN_μ
$B^0 \to K^+\pi^-$	> 0.15	> 0.8	> 0.9	—
$B^- \to J/\psi\, K^-$	—	> 0.8	—	> 0.95

5.4.1 Fit to the $B^0 \to K^+\pi^-$ data sample

The unbinned maximum likelihood fit is performed, being implemented as the minimization of a ROOFIT [109] calculated likelihood function by the ROOT implementation of MINUIT [110]. This fitting procedure is used for any fits described in this thesis.

The fit to the distribution of the $\mathrm{K}\pi$ invariant mass is performed for two different event selections, both defined to handle possible MC/Data discrepancies.

The first selection follows a similar strategy to the one optimized for the signal channel, except the BDT requirement. It is used to select the BDT calibration sample. The second one, dedicated to the $B^0 \to K^+\pi^-$ signal selection exclusively, includes BDT and PID requirements. This selection is used to verify the exactness of the event selection defined in the analysis strategy. The offline requirements of the defined selections are indicated in Tab. 5.9.

The physical background is composed of two body b-hadron decay reflections and partially reconstructed decays. The event selection of the $B^0 \to K^+\pi^-$ is assumed to yield data samples composed of classes of modes listed in Tab.5.10.

The fitting procedure includes scaling of the contamination from different decay modes, as explained in Sect.5.5. The outcome of the invariant mass fitting procedure performed for the two selections described above may be seen in Fig. 5.10 and Fig. 5.11. For the purpose of the calibration procedure on top of the

fitted model PDF the ${}_s\mathcal{P}\mathrm{lot}$ technique has been employed. General ideas behind this method are given in Appendix C.0.1. The exactness of the event selection strategy is verified by comparing the fitted yield after full offline selection with the expected one. The details are given below.

TABLE 5.10: Classes of modes assumed to be present in selected data samples for $B^0 \to K^+\pi^-$ control channel studies.

Misidentified modes:	Partially reconstructed background:
$B_s^0 \to \pi^+K^-$	$B^0 \to K^+K^-\pi^0$
$B_s^0 \to K^+K^-$	$B^0_{(s)} \to K^+\pi^-\pi^0$
$B^0_{(s)} \to \pi^+\pi^-$	

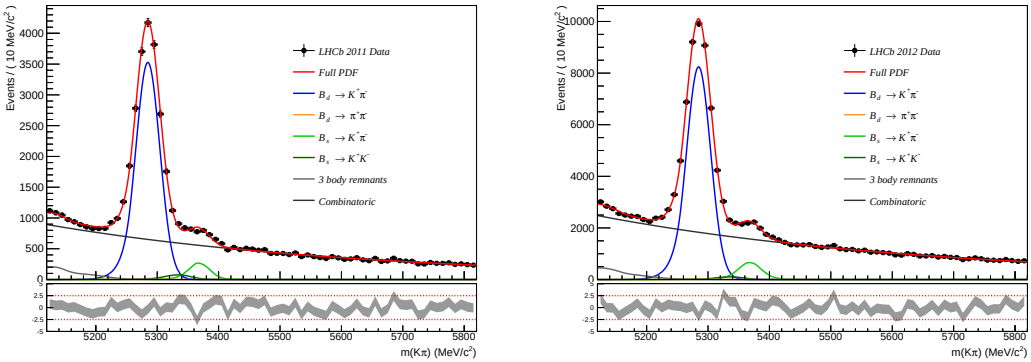

FIGURE 5.10: Fits to the Kπ invariant mass for 2011 (left) and 2012 (right) datasets after the selection defined for BDT calibration procedure. The individual contributions are shown as curves labelled in the legend. The resulting pull distributions are attached in the bottom of the plots. This convention will be followed in many subsequent plots.

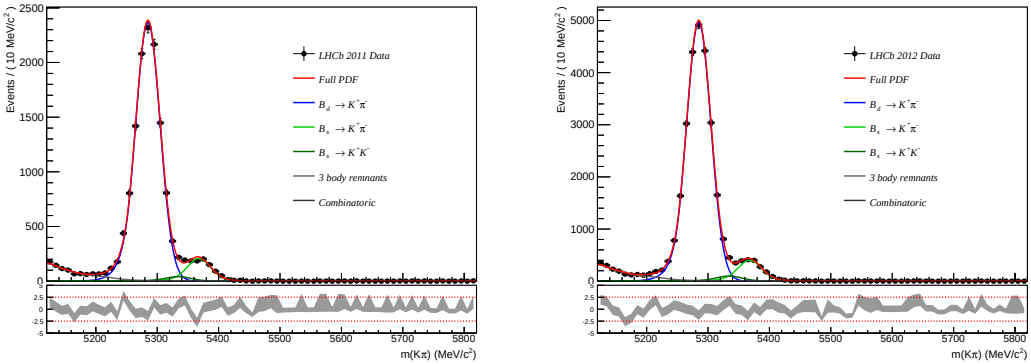

FIGURE 5.11: Fits to the Kπ invariant mass for 2011 (left) and 2012 (right) datasets after full off-line selection. The individual contributions are shown as curves labelled in the legend.

5.4.2 Fit to the $B^- \to J/\psi K^-$ data sample

The event selection for the $B^- \to J/\psi K^-$ control channel indicated in Tab.5.9 is assumed to yield the data sample composition of a clear signal mode which is modelled as a double CrystalBall PDF [111]. The final fit to the 2012 dataset is presented in Fig. 5.12. On top of the fitted model PDF the outcome of the ${}_s\mathcal{P}\mathrm{lot}$ technique has been applied.

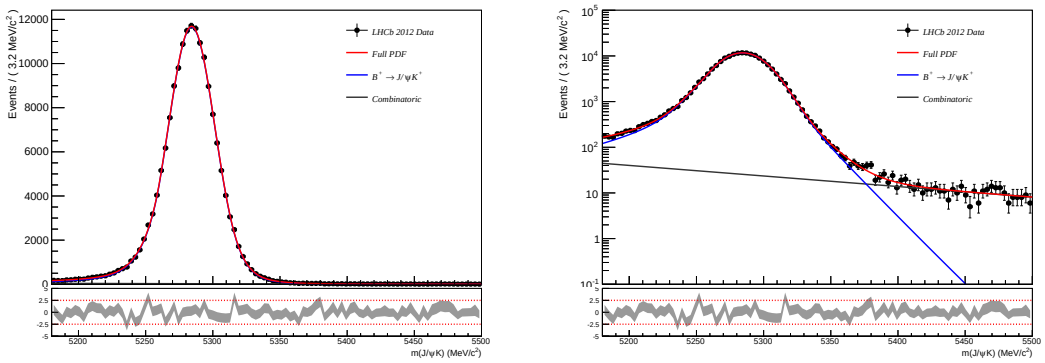

FIGURE 5.12: Fit to the J/ψ K invariant mass for 2012 dataset after full offline selection. The individual contributions are shown as curves labelled in the legend.

5.4.3 MC/data discrepancies

Using the above mentioned control channel data sample, the $sWeighted$ distributions of the key variables for data are compared to the simulated ones. The calibrated distributions are used for the MC MVA event selection, as described in Sect.5.3.4.2 and Sect.5.3.4.3. The exemplary distributions for the 2012 dataset are presented in Fig.5.13, while the additional ones may be seen in Appendix B. To quantify the discrepancy between the two distributions of a given variable, the Separation Power (SP) variable is introduced. The value of SP is determined from two normalized histograms and their bin contents $h_X(i)$, $h_Y(i)$ and it is as follows:

$$SP(X,Y) = \frac{1}{2}\sum_{i}^{N} |h_X(i) - h_Y(i)|. \tag{5.7}$$

Its value lies within the range $0-1$, where 0 means total agreement of both distributions with no separating power, and 1 stands for total disagreement with the maximum separating power.

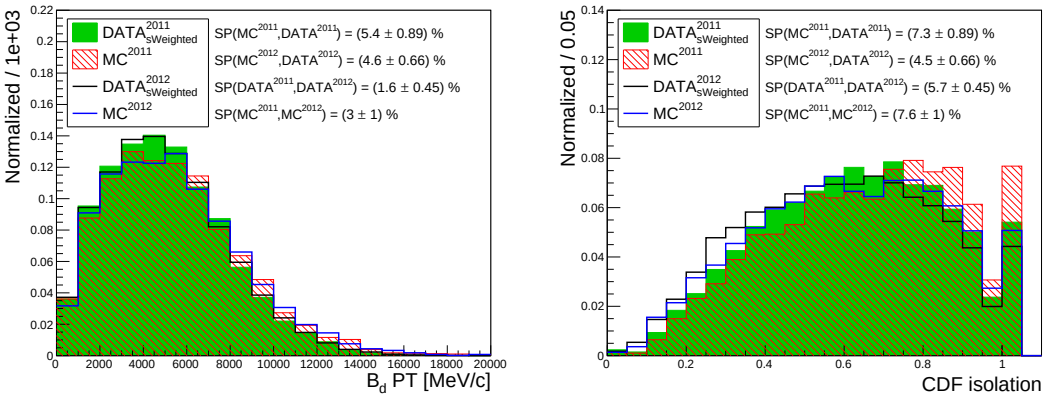

FIGURE 5.13: MC/Data discrepancies in kinematic variables for considered datasets. The mother transverse momentum (left) and CDF isolation (right) variables are presented. The value of SP is given for quantitative comparison of different datasets. The individual distributions are labelled in the legend.

Since the discrepancies in the MC simulation compared to the data have been spotted, they have to be taken into account as they may possibly influence the BDT classifier output. This is verified by direct comparison of the BDT response distributions from the control channel for the simulation and the signal extracted from data, as illustrated in Fig. 5.14. As follows, the BDT calibration is applied according to the description in Sect.5.3.4.2.

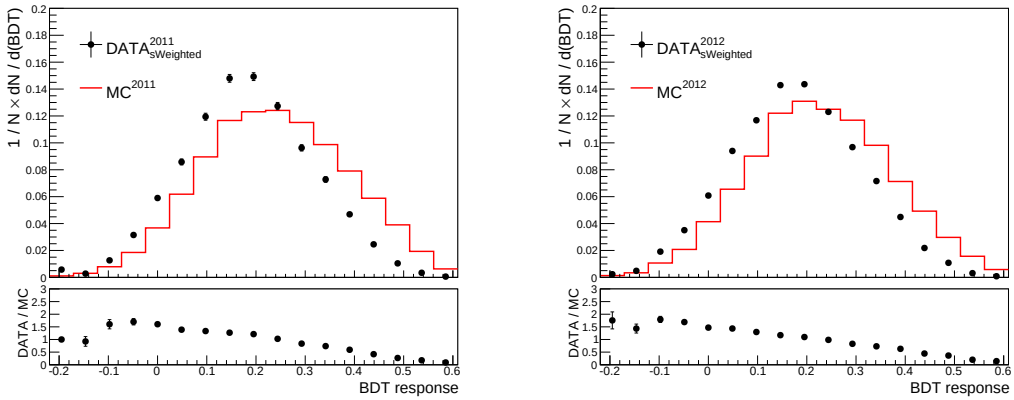

FIGURE 5.14: BDT responses on $B^0 \to K^+\pi^-$ sample for data (calibration sample) and MC for 2011 (left) and 2012 (right) datasets.

5.4.4 The comparison of expected and observed $B^0 \to K^+\pi^-$ yields

The expected $B^0 \to K^+\pi^-$ yield has been estimated from Eq. 5.1. The comparison with the observed number of events determined from the fit to the data may be treated as the the final test of the exactness of the selection. The expected yields are evaluated for the integrated luminosity of the whole

available data, processed as indicated in Sect.5.2. The integrated luminosities are taken with $1.71(1.16)\%$ uncertainty for 2011(2012) data, respectively [112]. The cross-sections $\sigma(pp \to b\bar{b}X)$ for the two given energies are:

$$\sigma_{b\bar{b}} = (284 \pm 20 \pm 49)\,\mu\mathrm{b}\sqrt{\mathrm{s}} = 7\mathrm{TeV}, \tag{5.8}$$

$$\sigma_{b\bar{b}} = (329 \pm 20 \pm 57)\,\mu\mathrm{b}\sqrt{\mathrm{s}} = 8\mathrm{TeV}, \tag{5.9}$$

where the value for 2011 conditions has been adopted from the LHC*b* measurement [51], while for 2012 it has been extrapolated from theory prediction [18].

Referring to Eq.5.4 the subsequent factors for a total efficiency are determined and averaged over different magnet polarities. All efficiencies have been obtained relying on MC samples and are compiled in Tab.5.11, where the quoted errors are statistical ones, added in quadrature for the total efficiency.

The generator level cut efficiencies, denoted as ε^{Gen}, correspond to the detector acceptance of $10 < \theta < 400$ mrad. After event generation only those events are saved where all daughter tracks traverse through the detector. Such events can be then correctly reconstructed. The fraction of such events determines the generator level cut efficiency.

The efficiencies related to the reconstruction, namely $\varepsilon^{Rec/Gen}$, denote the efficiencies for all daughter particles reconstructed as `Long` tracks with respect to the ones generated within the LHC*b* acceptance. The value may be misleading when compared to the excellent performance of the muon track reconstruction, presented in Fig.4.12. The difference lies in the definition of the reconstruction efficiency. Extracting the efficiency from MC, one calculates its value with respect to the fraction of generated tracks within the LHC*b* acceptance. The quoted data-driven method determines the value with respect to the tracks which are reconstructible (with enough number of hits in the appropriate tracking detectors). To be more specific, the MC based method is embedding two factors, *i.e.*:

$$\varepsilon^{Rec/Gen} = \frac{N^{Reconstructible}}{N^{Generated}} \times \frac{N^{Reconstructed}}{N^{Reconstructible}}. \tag{5.10}$$

Combining reconstruction efficiencies for different track types (as it has been done in this analysis), one should consider non-negligible differences in the interaction cross-section for kaons, pions and muons which propagate relatively long distances (interact only through the weak and electromagnetic forces), which affects the $\varepsilon^{Rec/Gen}$. In addition, a small difference between the 2011 and 2012 efficiency is due to changes that have been performed at the level of tracks reconstruction algorithms.

The events passing the physics trigger requirements are then filtered offline by the stripping requirements indicated in Sec. 5.3.2. The stripping selection efficiency, $\varepsilon^{Strip/Rec}$, is determined as the fraction of a certain stripping line which accepts tracks from those being reconstructed.

[18] Scale factor has been calculated for PYTHIA $b\bar{b}$ cross-section used for 2011 and 2012 simulation in LHC*b*.

Subsequently, the trigger efficiency for the considered channel is taken for MC events after the full selection, $\varepsilon^{Trig/Sel}$. The following section shows that this approach is compatible with the data-driven method for the trigger efficiency determination.

Finally, the MVA discriminant selection efficiency is calibrated to data. The PID efficiency, ε^{PID}, is evaluated using the `PIDCalib` method, as described in Sect.5.3.4.3, while the efficiency for the BDT selection is calibrated to data, as described in Sect.5.3.4.2.

TABLE 5.11: Efficiencies determined on MC for $B^0 \to K^+\pi^-$ sample. Binomial errors are quoted and their relative values are added in quadrature for total efficiencies.

Efficiency [%]	2011	2012
ε^{Gen}	18.50 ± 0.08	19.01 ± 0.01
$\varepsilon^{Rec/Gen}$	52.69 ± 0.16	50.21 ± 0.14
$\varepsilon^{Strip/Rec}$	23.91 ± 0.19	24.66 ± 0.17
$\varepsilon^{Trig/Sel}$	44.51 ± 0.31	43.03 ± 0.49
ε^{PID}	33.56 ± 0.66	30.87 ± 0.19
$\varepsilon^{BDT/PID}$	63.56 ± 1.45	60.86 ± 1.87
ε^{TOTAL}	0.221 ± 0.007	0.190 ± 0.007

The corresponding fragmentation factor and branching ratio are:

$$f_d = (40.5 \pm 0.6)\%, \tag{5.11}$$

$$\mathcal{B}(B^0 \to K^+\pi^-) = (1.96 \pm 0.05) \times 10^{-5}, \tag{5.12}$$

whose values were taken from PDG [1]. Using all assumed values of the parameters listed in Tab.5.11, the expected yields read:

$$N^{B^0\to K^+\pi^-}_{expected}(2011) = 9981 \pm 2117, \tag{5.13}$$

$$N^{B^0\to K^+\pi^-}_{expected}(2012) = 20444 \pm 3906. \tag{5.14}$$

The yields obtained from fitting to the $B^0 \to K^+\pi^-$ data sample read:

$$N^{B^0\to K^+\pi^-}_{fitted}(2011) = 12212 \pm 139, \tag{5.15}$$

$$N^{B^0\to K^+\pi^-}_{fitted}(2012) = 27728 \pm 196. \tag{5.16}$$

The obtained expected $B^0 \to K^+\pi^-$ yield is then $\sim 1.1\sigma$ ($\sim 1.9\sigma$) away from the yield extracted from the fit for 2011 (2012) dataset, which shows that the efficiency calculation has been performed in a proper way.

5.4.5 Verification of the trigger efficiency

To mimic the selection defined for the signal mode, the same set of trigger lines has been used for the control channels, as it is stated in Sect.5.3.3. To verify the efficiencies determined on MC the `TISTOS` method (see Sect.4.2.2.2) has been applied to the control channels. The overall trigger efficiency evaluated on the selected events, $\varepsilon^{Trig/Sel}$ is factorized as follows:

$$\varepsilon^{Trig/Sel} = \varepsilon^{Trig/Sel}_{L0} \times \varepsilon^{Trig/Sel}_{HLT1|L0} \times \varepsilon^{Trig/Sel}_{HLT2|HLT1L0}, \tag{5.17}$$

$$\varepsilon^{Trig/Sel}_{L0} = \varepsilon^{Trig/Sel}_{L0TOS} + \varepsilon^{Trig/Sel}_{L0TIS}(1 - \varepsilon^{Trig/Sel}_{L0TOS}). \tag{5.18}$$

Since at the L0 trigger level the different trigger flags are used. Asking for a positive decision of the HLT2 trigger reduces the statistics considerably, thus the $\varepsilon^{Trig/Sel}_{HLT2|HLT1L0}$ is determined from the simulation. The true trigger efficiency from MC determined using the `TISTOS` tagging provides a reference point and allows to verify how well the `TISTOS` method performs. In addition, it makes possible to evaluate the bias on the `TISTOS` method and use this bias as a systematic uncertainty assigned to this kind of approach.

The general formula of the method applied to the TIS type of trigger tag reads:

$$\varepsilon^{Trig/Sel}_{TIS} = N^{Trig/Sel}_{TISTOS}/N^{Trig/Sel}_{TOS}, \tag{5.19}$$

which is used to determine the TIS efficiency over the TOS subsample for the `L0Global` line. Similarly, for the TOS type of trigger tag the TOS efficiency over the TIS subsample for all specified signal trigger lines at each trigger stage is defined:

$$\varepsilon^{Trig/Sel}_{TOS} = N^{Trig/Sel}_{TISTOS}/N^{Trig/Sel}_{TIS}. \tag{5.20}$$

The results from different methods of trigger efficiency evaluation are given in Tab.5.12 for both control channels. It has been found that the trigger is well simulated, where the overall trigger efficiency taken from MC amounts to $(44.51 \pm 0.64)\%$ and $(43.03 \pm 0.49\%)$, which are 1.45σ and 0.56σ away from the values evaluated from data driven method for the 2011 and 2012 dataset, respectively. The discrepancy between the values determined on MC and data is accounted as respective systematic uncertainty.

The final cross-check performed on the $B^- \to J/\psi\, K^-$ sample allowed the verification of the quality of simulation of the muonic trigger type. It has been found that the trigger efficiency on this channel determined from the simulation amounts to $(86.24 \pm 0.21)\%$ which is 0.61σ away from the value that has been found using the data-driven method.

TABLE 5.12: Trigger efficiencies determined for the simulation of the control channels and verified with TISTOS method. The value of $\varepsilon^{Trig/Sel}$ variable has been determined from the number of events after the full offline selection.

Channel	Dataset	$\varepsilon^{Trig/Sel}$ [%]		
		MC	TISTOS (Data)	TISTOS (MC)
$B^0 \to K^+\pi^-$	2011	44.51 ± 0.64	40.47 ± 2.79	39.08 ± 4.09
$B^0 \to K^+\pi^-$	2012	43.03 ± 0.49	43.33 ± 1.77	40.26 ± 2.97
$B^- \to J/\psi\, K^-$	2012	86.24 ± 0.21	88.03 ± 2.89	87.52 ± 1.46

5.4.6 Trigger bias on BDT output

Extended studies have been performed to verify the effect of possible discrepancies that could come from the hadronic and muon trigger type when the BDT calibration coefficient is translated from $B^0 \to K^+\pi^-$ to the signal sample. The relation between these two types of triggers has been evaluated for the BDT response taken for $B^- \to J/\psi\, K^-$ after the selection specified in Tab.5.9. The trigger bias on the BDT response is defined as the ratio of two normalized histograms of the BDT response distribution for two different types of trigger at the L0 level, where the effect is assumed to be critical. Such a trigger bias has been studied by comparing the simulated distribution to the one obtained from $sWeighted$ distribution on data. The results related to the BDT range of interest may be seen in Fig. 5.15.

The conclusion is that the difference in the BDT response with respect to the trigger bias (different trigger type) is negligible - the ratio stays close to 1. Thus, the trigger bias is not taken into account during the BDT calibration procedure. However, it is taken into consideration in the final systematic uncertainty evaluation, see Sect.5.7.

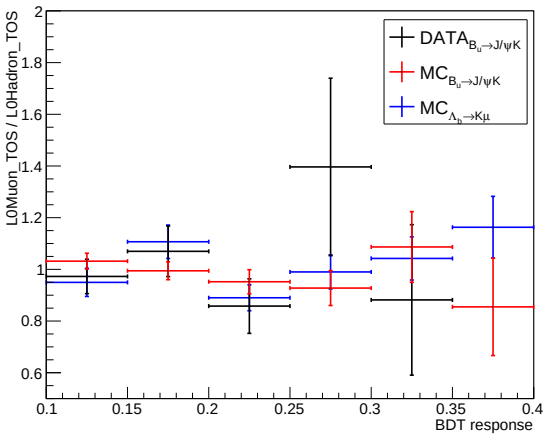

FIGURE 5.15: Trigger bias as a function of the BDT response determined on $B^- \to J/\psi\, K^-$ control channel.

5.5 Background characterization

The fit to the data samples is needed to handle the contamination of b-hadron misidentified backgrounds that have survived the selection. The following channels with corresponding branching ratios [1] are considered as sources of backgrounds due to reflections:

- $\mathcal{B}(B^0 \to K^+\pi^-) = (1.94 \pm 0.06) \times 10^{-5}$,
- $\mathcal{B}(B_s^0 \to K^+K^-) = (2.49 \pm 0.17) \times 10^{-5}$,
- $\mathcal{B}(B_s^0 \to \pi^+K^-) = (5.5 \pm 0.06) \times 10^{-6}$.

All of them are kinematically similar to $X_b \to K^-\mu^+$. To assess these background contributions to the Λ_b and Ξ_b^0 mass regions, the $B^0 \to K^+\pi^-$ control sample is used. As follows, the control sample is considered with $K\mu$ invariant mass hypothesis which gives access to the backgrounds due to reflections. Appropriate ProbNN_X requirements, indicated in Tab.5.13, have been found to access an invariant mass shape for each contributing misidentified channel. The BDT requirements when extracting those shapes are the same as for the final selection of $X_b \to K^-\mu^+$ (*cf.* Tab.5.8). The invariant mass distributions of each misidentified channel are modelled with the Crystal Ball PDF. The exponential and Gaussian PDFs are used, when needed, to model the partially reconstructed, combinatoric and peaking backgrounds. Figures 5.16,5.17, 5.18, 5.19 show the fitted shapes of the invariant mass distributions for considered misidentified channels and different datasets.

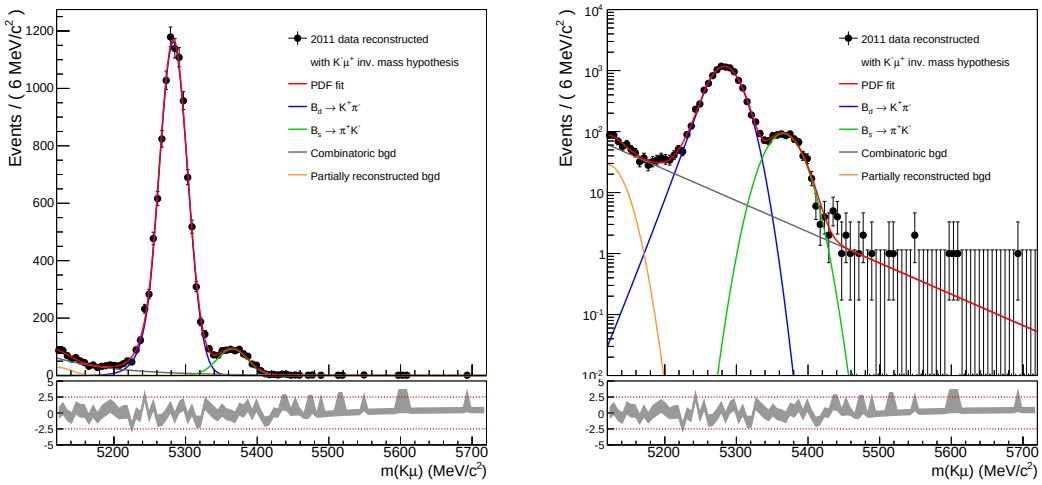

FIGURE 5.16: Distribution of $K\mu$ invariant mass for reconstructed $B^0_{(s)} \to \pi^+K^-$ events after full selection applied on 2011 data. A linear (left) and logarithmic (right) scales are used.

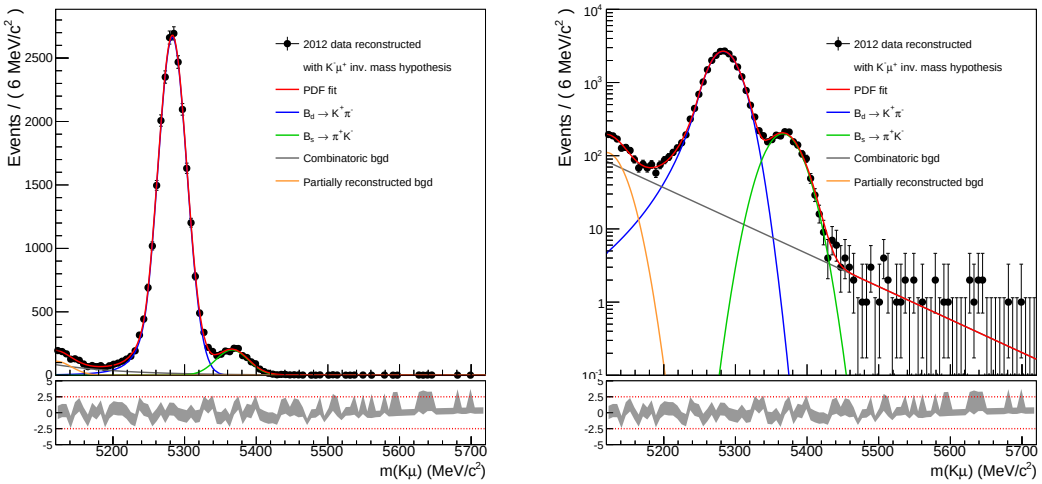

FIGURE 5.17: Distribution of $K\mu$ invariant mass for reconstructed $B^0_{(s)} \to \pi^+ K^-$ events after full selection applied on 2012 data. A linear (left) and logarithmic (right) scales are used.

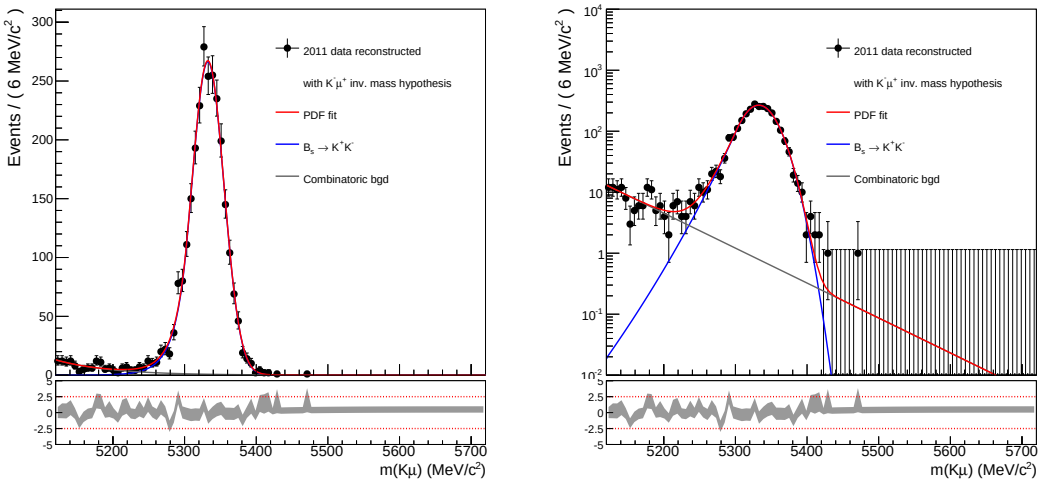

FIGURE 5.18: Distribution of $K\mu$ invariant mass for reconstructed $B^0_s \to K^+ K^-$ events after full selection applied on 2011 data. A linear (left) and logarithmic (right) scales are used.

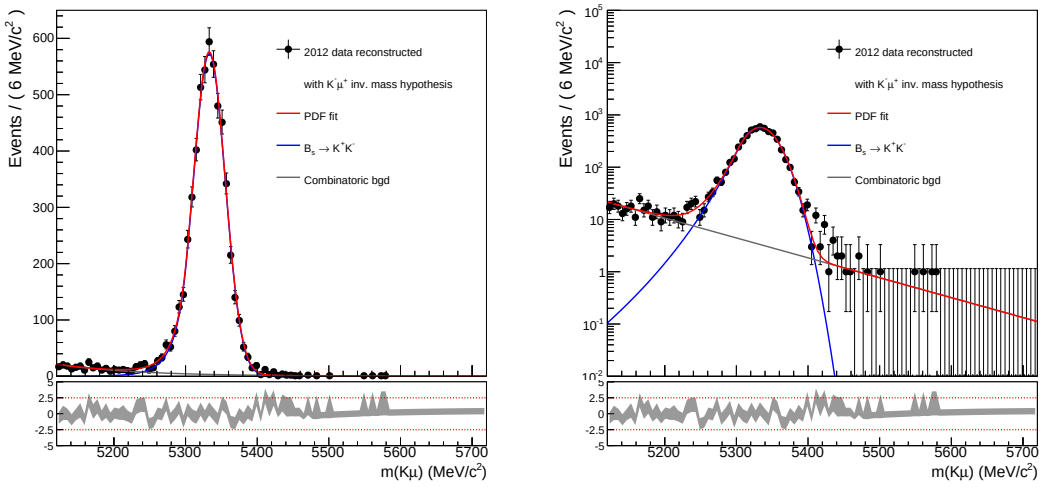

FIGURE 5.19: Distribution of $K\mu$ invariant mass for reconstructed $B_s^0 \to K^+K^-$ events after full selection applied on 2012 data. A linear (left) and logarithmic (right) scales are used.

TABLE 5.13: The offline ProbNN_X selection requirements for misidentified channels.

Channel	Kaon ProbNN_K	Pion ProbNN_K	Pion ProbNN_π
$B^0_{(s)} \to \pi^+K^-$	> 0.8	–	> 0.95
$B^0_s \to K^+K^-$	> 0.8	0.95	–

The $\Lambda_b \to h^+h'^-$ class of decays can potentially provide a contamination of the Λ_b signal region. The following decays with corresponding branching ratios are investigated [1]:

- $\mathcal{B}(\Lambda_b \to pK^-) = (5.3 \pm 1.0) \times 10^{-6}$,
- $\mathcal{B}(\Lambda_b \to p\pi^-) = (4.4 \pm 0.8) \times 10^{-6}$.

For the final selection defined for the $X_b \to K^-\mu^+$ the total efficiency, including the PID and BDT requirements, for the above mentioned channels is found to be $(4.2 \pm 0.8) \times 10^{-7}$ for $\Lambda_b \to p\ K^-$ and $(6.4 \pm 1.2) \times 10^{-7}$ for $\Lambda_b \to p\ \pi^-$. In conclusion, the full selection reduces significantly the contamination from these sources. Owing to the fact that these efficiencies are two orders of magnitude lower with respect to the other considered b–hadron decays, and taking into account the branching ratio of the $\Lambda_b \to h^+h'^-$, these processes are assumed to be negligible within the fit to the signal data sample.

5.5.1 Background in the signal mass regions

The particular PDFs of peaking backgrounds have been fitted separately to the distribution on the control channel using events surviving the BDT selection and appropriate ProbNN_X requirements, as described in the previous subsections. Then, the physical background PDF is taken as a product of PDFs of each misidentified channel with the coefficients left as free parameters in the full model PDF. The combinatorial background is modelled with the exponential function.

The results of the fitting procedure performed on signal channel data are presented in Fig.5.20 and Fig.5.21. The number of expected background events with uncertainties in each dataset, together with the observed number of events, is given in Tab.5.14. For the number of expected background events the error is statistical one. The procedure of estimating the systematic uncertainty, which turned out to be negligible, is given in Sect.5.7.

TABLE 5.14: The number of expected background events obtained from the fits to the sidebands of the Λ_b and Ξ_b^0 baryon masses. The number of observed events after opening the box is given.

Channel:	Dataset	Expected	Observed
$\Lambda_b \to K^-\mu^+$	2011	3.5 ± 1.1	5
	2012	5.8 ± 1.3	3
$\Xi_b^0 \to K^-\mu^+$	2011	1.2 ± 0.5	1
	2012	1.7 ± 0.5	3

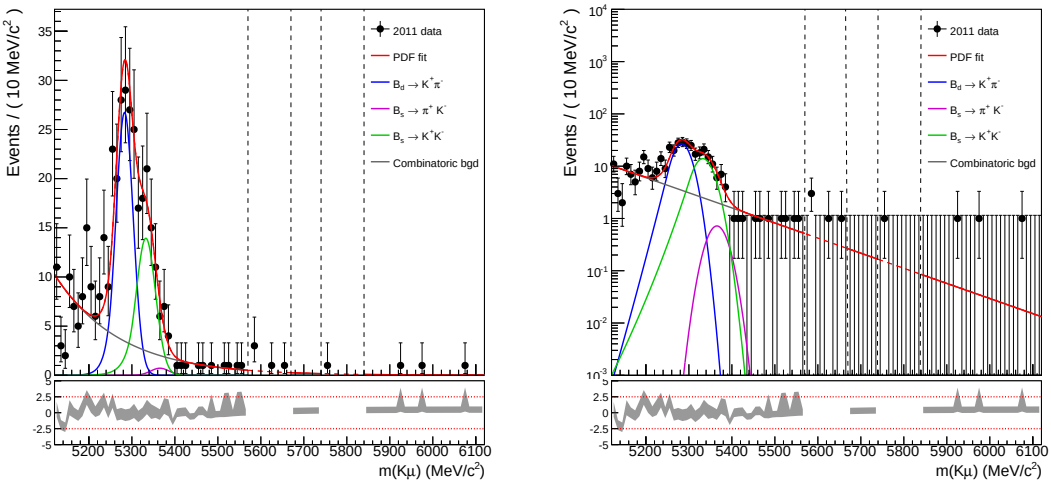

FIGURE 5.20: Distribution of $K\mu$ invariant mass for the 2011 sample after full optimized selection. The vertical dashed lines define the blinded regions during selection optimization. The red solid line shows the result of the fitting procedure to a defined background model PDF in the sidebands of the (K^+ μ^-) invariant mass. A linear (left) and logarithmic (right) scales are used.

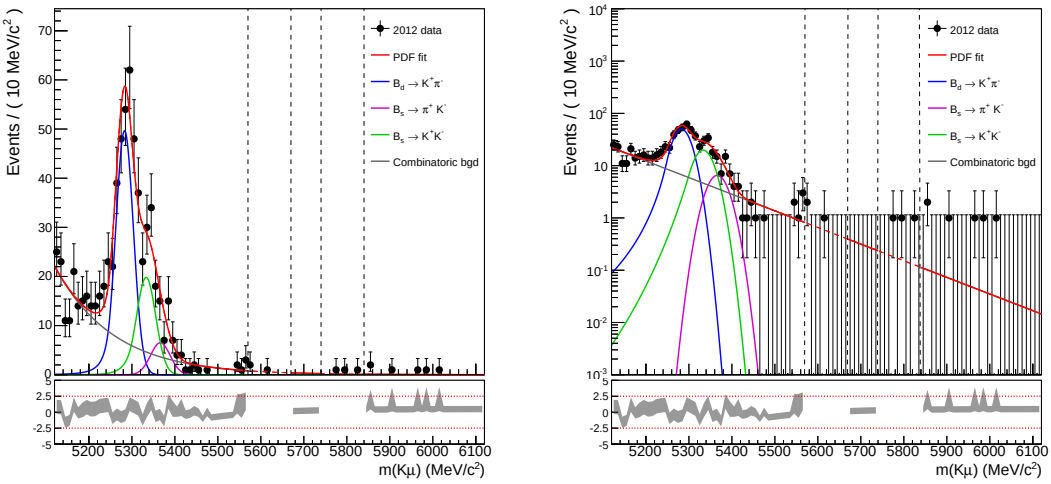

FIGURE 5.21: Distribution of $K\mu$ invariant mass for the 2012 sample after full optimized selection. The vertical dashed lines define the blinded regions during selection optimization. The red solid line shows the result of the fitting procedure to a defined background model PDF in the sidebands of the (K^+ μ^-) invariant mass. A linear (left) and logarithmic (right) scales are used.

5.6 Normalization of the signal yield

To estimate the signal branching fraction for $X_b \to K^-\mu^+$, the number of the observed signal events, $N(X_b \to K^-\mu^+)$ is normalized to the number of events in the $\Lambda_b \to pK^-$ channel. This procedure is performed according to the formulas defined in Sect.5.1, which can be generalized as follows:

$$\mathcal{B}(X_b \to K^-\mu^+) = \alpha_{X_b} \times N(X_b \to K^-\mu^+), \tag{5.21}$$

where α_{X_b} is the overall normalization factor, defined for two signal channels:

$$\alpha_{\Lambda_b} = \frac{\mathcal{B}(\Lambda_b \to pK^-)}{N(\Lambda_b \to pK^-)} \times \frac{\varepsilon^{TOTAL}_{\Lambda_b \to pK^-}}{\varepsilon^{TOTAL}_{\Lambda_b \to K^-\mu^+}}, \tag{5.22}$$

$$\alpha_{\Xi_b^0} = \frac{\mathcal{B}(\Lambda_b \to pK^-)}{N(\Lambda_b \to pK^-)} \times \frac{\varepsilon^{TOTAL}_{\Lambda_b \to pK^-}}{\varepsilon^{TOTAL}_{\Xi_b^0 \to K^-\mu^+}} \times \frac{f_{\Lambda_b}}{f_{\Xi_b^0}}. \tag{5.23}$$

The branching fraction used in the normalization of the signal yield amounts to:

$$\mathcal{B}(\Lambda_b \to pK^-) = (4.9 \pm 0.9) \times 10^{-6}, \tag{5.24}$$

which corresponds to the current estimate as given by the PDG [1]. An extra factor that enters the normalization factor for the $\Xi_b^0 \to K^-\mu^+$ decay, stands for the relative rate of Λ_b to Ξ_b^0 baryon production. The measurement performed by LHC*b*, indicated in Tab. 5.1, makes it possible to estimate its value to be $f_{\Lambda_b}/f_{\Xi_b^0} = 0.19 \pm 0.01$, assuming $\mathcal{B}(\Xi_b^0 \to \Xi_c^+\pi^-)/\mathcal{B}(\Lambda_b \to \Lambda_c^+\pi^-) \approx 1$ and $\mathcal{B}(\Xi_c^+ \to pK^-\pi^+)/\mathcal{B}(\Lambda_c^+ \to pK^-\pi^+) \approx 0.1$.

The MVA event selection poses the following requirements: BDT> 0.15, $\mathrm{ProbNN}_K > 0.8$ and $\mathrm{ProbNN}_p > 0.9$ for normalization channel. This reduces the background from the misidentification of one or both decay daughters particles and rejects a combinatoric background, the latter having a wide range of signal efficiencies. The efficiencies of the ProbNN_X discriminant are calibrated to data in the same manner as described in 5.3.4.3. The BDT classifier trained on the $\Lambda_b \to K^-\mu^+$ signal channel is applied to the normalization mode, where the selection efficiency is extracted from the data driven way. The efficiencies for all introduced steps of the event selection for signal and normalization channels are summarized in Tab. 5.15 and Tab.5.16 for 2011 and 2012 datasets, respectively.

TABLE 5.15: Efficiencies determined for signal and normalization channels for 2011 dataset. Binomial errors are quoted and their relative values are added in quadrature for total efficiencies.

Efficiency [%]	$\Lambda_b \to K^-\mu^+$	$\Xi_b^0 \to K^-\mu^+$	$\Lambda_b \to pK^-$
ε^{Gen}	18.68 ± 0.06	18.68 ± 0.06	19.09 ± 0.07
$\varepsilon^{Rec/Gen}$	60.15 ± 0.18	60.72 ± 0.17	48.47 ± 0.11
$\varepsilon^{Strip/Rec}$	56.55 ± 0.23	56.94 ± 0.22	47.12 ± 0.16
$\varepsilon^{Trig/Sel}$	75.14 ± 0.56	76.18 ± 0.49	47.42 ± 0.64
ε^{PID}	71.95 ± 0.32	73.42 ± 0.34	21.97 ± 0.24
$\varepsilon^{BDT/PID}$	35.64 ± 0.22	39.56 ± 0.21	71.60 ± 4.36
ε^{TOTAL}	1.224 ± 0.014	1.428 ± 0.017	0.325 ± 0.009
$\varepsilon^{TOTAL}_{\Lambda_b \to pK^-} / \varepsilon^{TOTAL}_{X_b \to K^-\mu^+}$	0.266 ± 0.035	0.228 ± 0.009	—

TABLE 5.16: Efficiencies determined for signal and normalization channels for 2012 dataset. Binomial errors are quoted and their relative values are added in quadrature for total efficiencies.

Efficiency [%]	$\Lambda_b \to K^-\mu^+$	$\Xi_b^0 \to K^-\mu^+$	$\Lambda_b \to pK^-$
ε^{Gen}	18.92 ± 0.08	18.92 ± 0.06	19.9 ± 0.1
$\varepsilon^{Rec/Gen}$	57.02 ± 0.19	57.62 ± 0.18	45.9 ± 0.08
$\varepsilon^{Strip/Rec}$	54.36 ± 0.25	55.70 ± 0.23	45.99 ± 0.12
$\varepsilon^{Trig/Sel}$	81.91 ± 0.83	81.54 ± 0.49	43.75 ± 0.47
ε^{PID}	57.45 ± 0.37	59.22 ± 0.38	21.18 ± 0.24
$\varepsilon^{BDT/PID}$	34.99 ± 0.38	38.70 ± 0.24	66.29 ± 2.74
ε^{TOTAL}	0.966 ± 0.017	1.135 ± 0.014	0.258 ± 0.006
$\varepsilon^{TOTAL}_{\Lambda_b \to pK^-} / \varepsilon^{TOTAL}_{X_b \to K^-\mu^+}$	0.267 ± 0.011	0.227 ± 0.008	—

The full selection applied for the normalization channel gives a clear signal. The signal yield that fulfils Eq. 5.2 is evaluated from the unbinned maximum likelihood fit. The exponential PDF for combinatorial background and the Gauss PDF for the signal have been used to model the (pK) invariant mass distribution. The output of the performed fits is shown in Fig. 5.22 for 2011 and 2012 datasets. The resulting yields obtained from fitting to the $\Lambda_b \to pK^-$ data samples together with overall normalization factors are indicated in Tab.5.17.

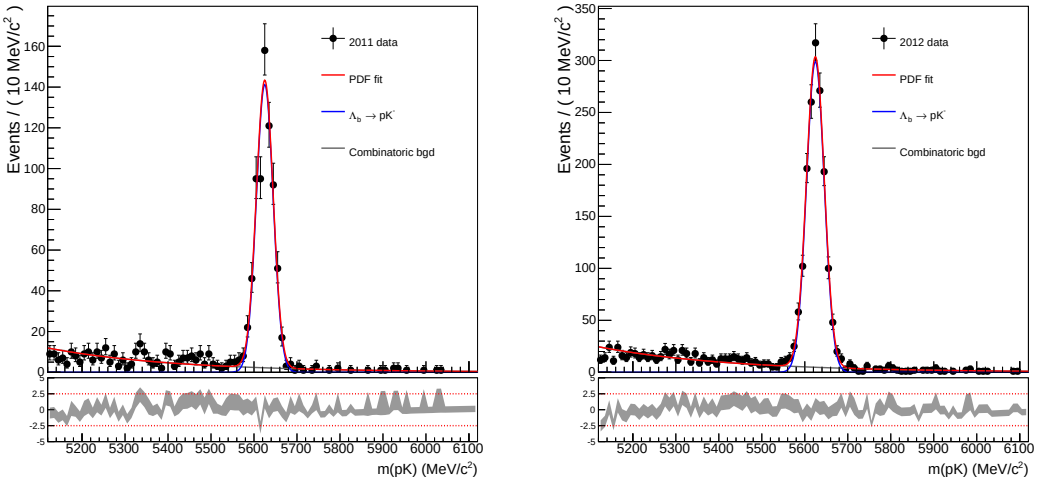

FIGURE 5.22: Fit to the pK invariant mass for 2011 (left) and 2012 (right) data after full selection.

TABLE 5.17: Yields obtained from the fit to the $\Lambda_b \to pK^-$ data samples and the final normalization factors used to estimate the signal branching fraction for $X_b \to K^- \mu^+$.

CMS energy	7 TeV	8 TeV
$N_{fitted}^{\Lambda_b \to pK^-}$	$689 \pm 27^{stat} \pm 13^{syst}$	$1552 \pm 41^{stat} \pm 30^{syst}$
α_{Λ_b}	$(1.89 \pm 0.42) \times 10^{-9}$	$(0.84 \pm 0.16) \times 10^{-9}$
$\alpha_{\Xi_b^0}$	$(8.52 \pm 1.68) \times 10^{-9}$	$(3.78 \pm 0.74) \times 10^{-9}$

5.7 Systematic uncertainties

Several systematic uncertainties have been already discussed. In addition, the internal consistency of the analysis has been verified by performing appropriate cross-checks, in particular comparing data and MC distributions or by splitting data into independent subsets.

Here an additional source of *external* uncertainty is taken into account, which is due to (known) uncertainties of input parameter values. Owing to the normalized measurement, the number of such parameters is limited - the systematics uncertainties including those coming from luminosity, cross-section and fragmentation are simply cancelled. The most significant uncertainty of this kind is related to the branching ratio of the normalization channel, which amounts to a relative value of 18.38%.

In case of measurement of the branching fraction for the decay channel $\Xi_b^0 \to K^- \mu^+$ an additional factor appears, namely the ratio of fragmentation fraction of $b \to \Xi_b^0$ and $b \to \Lambda_b$. The latter is known with the relative error of 5.25%, as adopted from [96].

In addition to the indicated external errors, the *experimental* systematic uncertainty may be defined, based on incomplete knowledge about detector acceptances or trigger efficiencies, incorrect background characterization *etc.* More potential sources of experimental systematic uncertainty are specified below.

Another possible source of systematic uncertainty is related to the detector geometric acceptance due to imperfect MC description of the detector. However, all other LHC*b* studies revealed that the the MC description of the detector is reasonable. In addition, most of the potential imperfections of this kind cancel in the normalization procedure. Hence no systematic uncertainty is set to the ratio of generator level efficiency.

Since this analysis is probing the branching ratio, the track reconstruction efficiency is an important quantity to be estimated. It expresses the feasibility of reconstructing trajectories of charged particles that have passed through the whole tracking system. In view of estimating this efficiency from the simulation, it is relevant to assign a systematic uncertainty to this method. For the momentum spectrum of the J/ψ decay products, the efficiency ratio of data and simulation amounts to $(100.9 \pm 0.6)\%$ for 2011 data [113]. This introduces the systematic uncertainty of about 0.4%. In addition, the effect of hadronic interactions leads to the the systematic uncertainty for hadrons as well, owing to their interactions with the material. This effect is assumed to be at the level of about 1.1%. In general, these two types of uncertainties are partially cancelled within the normalization procedure. However, the signal channel includes a muon in the final state in contrary to the fully hadronic normalization channel. Thus, the overall systematic uncertainty related to this issue is taken as the sum of squares of the two above mentioned systematic uncertainty sources accounting to be of 1.17%.

The trigger efficiencies have been assessed on MC for all the modes. The consecutive TCK configuration over the 2011 and 2012 data taking has been

verified as a potential source of systematics, since the MC samples are produced using a single, representative TCK per year. Hence, on top of the centrally produced MC files additional TCKs have been simulated using appropriate MOORE versions. These studies yielded small fluctuations, below 1%.

The more thorough cross-checks of the trigger efficiency evaluation have been performed with the data-driven method using more abundant control channels. The details may be found in Sect. 5.4.5 where data-MC discrepancies are estimated and the impact of different trigger types on the relative trigger efficiency determination is studied. Relaying on the `TISTOS` technique, it has been found that the trigger itself and the ratio of different trigger types are reasonably well simulated within the errors. Finally, 2% of systematic uncertainty is assigned to the relative trigger efficiency, which is assumed to account for all trigger related issues discussed here.

There is also a noticeable source of systematics uncertainty in the PID calibration procedure. It is related to the choice of binning for variables, where we assume that the PID response of the RICH detectors can be accurately described by these variables alone. In particular, the MC does not correctly reproduce the multiplicity distribution. To handle this issue, PID efficiencies have been extracted for the control channel with two different binning schemes: without the multiplicity distribution and with the one corrected to data. The variation here amounts to 0.8% of the relative difference with respect to the binning which includes the corrected multiplicity variable. This error is assumed to cancel within the normalization. The independent cross-check has involved the PID efficiency value extracted from the yields obtained from fits to the control channel data. The results of this method are compared with those obtained from the 2-dimensional `PIDCalib` evaluation. The relative difference between these two efficiencies amounts to 5.97% with respect to the one obtained from the control channel. To account for the uncertainty related to the PID calibration the 6% uncertainty is assigned for the relative PID selection efficiency determination.

The BDT discriminant is optimised using MC events for the signal, hence it relies on an accurate description of the input variables. Thus, any discrepancy between data and MC is the source of systematic uncertainty on the BDT selection, where the MVA method itself does not introduce additional systematic uncertainties. To deal with the data-MC discrepancies spotted within compared BDT responses, the calibration procedure using the control channel has been performed. In addition, the possible trigger bias has been studied and concluded to be negligible. The BDT selection efficiency, related to the differences arising from its determination from MC and data in the normalization channel, amounts for 5%. However, this uncertainty partially cancel in the normalizing procedure. In conclusion, the 2% uncertainty has been assigned to the relative BDT selection efficiency determination.

The systematic uncertainties coming from the fitting procedure applied to the invariant mass distributions are the last studied source of systematics. They might arise from a non-perfect knowledge of the models used to fit the mass distributions (*e.g.* PDF shapes assumed). With regards to the evaluation of normalization yield, the signal and combinatorial shape modelling has been

checked by refitting the data with variations of the assumed PDFs. The relative difference between the yields extracted from the performed fits is taken as the systematic uncertainty. The overall systematic uncertainty assigned to the $\Lambda_b \to pK^-$ yield corresponds to the sum of the squares of the two indicated sources of systematic uncertainty and amounts to 1.95%.

The source of systematic uncertainty on the background yield in the signal region is related to the modelling of the background in the full model PDF. The classes of misidentified modes are modelled using PDFs extracted from data, as described in Sect. 5.5. The systematic uncertainty arising from the parameters corresponding to the contributing PDFs has been studied together with the combinatoric background modelling. This has been checked by performing the fit on toy Monte Carlo samples, corresponding to variations in the fit model parameters. As follows, the Cholesky decomposition [114] of a given i-th PDF systematics covariance matrix has been done:

$$C_i = L_i \cdot L_i^T, \tag{5.25}$$

where L_i is a lower triangular matrix and L_i^T is its transposition. A statistically large number (100,000 in this analysis) of k element random vectors, $\vec{v}_i^k$ were generated[19] for i-th PDF definition and k fitting parameters. This constitutes the full model PDF where the contributing PDFs correspond to: $B_s \to K^+\pi^-$ PDF (11 free parameters), $B_s^0 \to K^+K^-$ PDF (6 free parameters), $X_b \to K^-\mu^+$ PDF (4 free parameters). A set of weighted vectors $\vec{w}_i^k$ has been calculated using the formula:

$$w_i = L_i \cdot v_i. \tag{5.26}$$

The vectors $\vec{w}_i$ were used to randomly change the estimated number of background events within the uncertainties described in the fitted PDF covariance matrix. The outcome of this procedure is the systematic error for estimated number of background events calculated as the difference between initially estimated value and 68% confidence level values of the distribution obtained from the above described procedure. The calculated systematic error has been found insignificant and, thus, neglected (*cf.* Tab.5.18).

Ultimately, all systematic uncertainties are compiled in Tab.5.18, where the selection efficiency related to $\Lambda_b \to pK^-$ stands for the combined MVA selection uncertainty defined above, taken with a sum of the squares of both the BDT and ProbNN_X. It can be seen that the dominant uncertainty is due to the the branching fraction of the normalization channel, while all the other errors stay at a relatively low level.

[19] The generation has been performed according to the standard Gaussian distribution.

TABLE 5.18: Summary of the systematic uncertainties. The totals correspond to the sum of the squares of corresponding partial uncertainties.

Source of systematic uncertainty	Estimated systematic uncertainty [%]		
	$\Lambda_b \to K^-\mu^+$	$\Xi_b^0 \to K^-\mu^+$	$\Lambda_b \to pK^-$
Branching fraction	n/a	n/a	18.38
Track Reconstruction Efficiency related to $\Lambda_b \to pK^-$	1.17	1.17	n/a
Trigger efficiency related to $\Lambda_b \to pK^-$	2.0	2.0	n/a
Selection efficiency related to $\Lambda_b \to pK^-$	5.4	5.4	n/a
Total efficiency related to to $\Lambda_b \to pK^-$	5.8	5.8	n/a
Signal yield from the mass fit	n/a	n/a	1.95
$f_{\Xi_b^0}/f_{\Lambda_b}$	n/a	2.13	n/a
Total	5.8	6.18	18.43

5.8 Results on the $\mathcal{B}(X_b \to K^-\mu^+)$

After the permission given by the LHC*b* collaboration to unblind the signal region for the purpose of this dissertation, no significant excess of events has been observed there, as it can be seen in Fig.5.20 and Fig.5.21 for 2011 and 2012 dataset, respectively. The numbers of observed events are summarized in Tab.5.14.

Assuming that the full selection yields a number of events S, which is statistically compatible with the average number of expected background events B, the experimental result is translated into an upper limit on the branching ratio.

To quantify that there is no statistically significant contribution from the considered signal channel, a widely used and commonly accepted statistical method called CL_s [115] has been used. The general ideas behind this method are described in Appendix C.0.2. The procedure is applied with the inputs indicated in Sect.5.6.

Additional systematic uncertainties correspond to the so-called nuisance parameters. The latter are defined as a parameters which are not of immediate interest but which must be accounted for in the evaluation of the quantity in question. The nuisance parameters considered in the branching fraction evaluation are associated with founded external and experimental systematic uncertainties specified in Sect.5.7.

The two independent selections defined for 2011 and 2012 datasets are treated as two channels with corresponding systematic uncertainties. The CL_s method is applied to the scenario with expected and observed background yields under the hypothesis to observe background events only in the $X_b \to K^-\mu^+$ selection.

5.8.1 The expected upper limit on the $X_b \to K^-\mu^+$

The distribution of the expected CL_s value versus the assumed branching ratio is shown as a dashed line Fig.5.23. It has been evaluated under the hypothesis to observe background events only in the $X_b \to K^-\mu^+$ selection. At the 95% confidence levels, the expected upper limits (median of all toy experiments in the CL_s method) for the branching fraction of both signals in question, including the systematic uncertainty, are found to be:

$$\mathcal{B}(\Lambda_b \to K^-\mu^+) < 4.3 \times 10^{-9} \ \text{ at } \ 95\% \ \text{ CL}, \tag{5.27}$$

$$\mathcal{B}(\Xi_b^0 \to K^-\mu^+) < 1.3 \times 10^{-8} \ \text{ at } \ 95\% \ \text{ CL}. \tag{5.28}$$

5.8.2 The observed upper limit on the $X_b \to K^-\mu^+$

After opening the blinded signal mass ranges, the distributions of the observed CL_s values are calculated, including the systematic uncertainties. The observed upper limits for the branching fraction of both signals in question are determined:

$$\mathcal{B}(\Lambda_b \to K^-\mu^+) < 3.6 \times 10^{-9} \ \text{ at } \ 95\% \ \text{ CL}, \tag{5.29}$$

$$\mathcal{B}(\Xi_b^0 \to K^-\mu^+) < 1.8 \times 10^{-8} \ \text{ at } \ 95\% \ \text{ CL}. \tag{5.30}$$

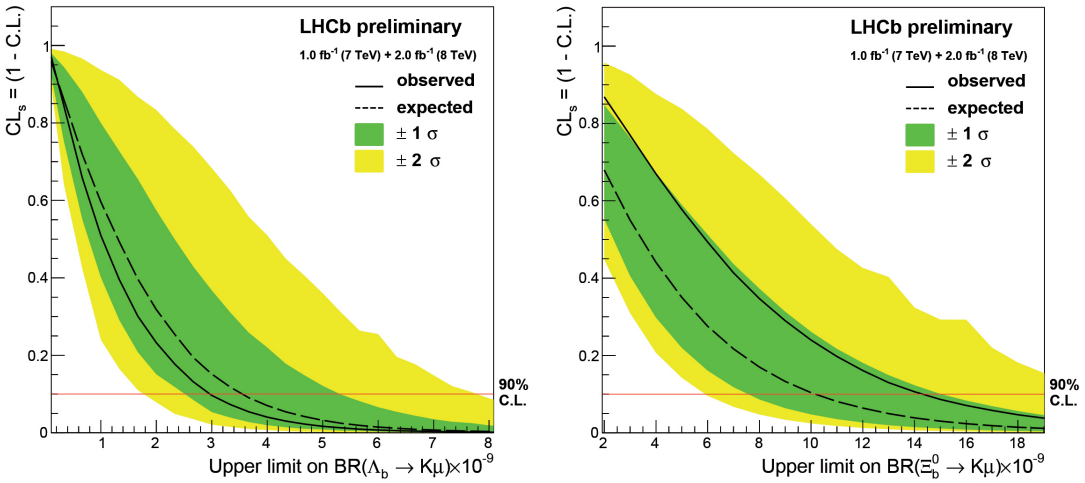

FIGURE 5.23: Expected (dashed) and observed (solid) CL_s curves with 68% (yellow) and 90 % (green) containment bands, under the hypothesis to observe background events only. The black solid line represents the observed value of CL_s, while the dashed one – the expected CL_s value.

As described in Sect.2.2, the processes involving violation of baryon ($\mathcal{B}$) and lepton ($\mathcal{L}$) number are expected in many extensions of the SM. The experimental searches for such phenomena have been summarized in Sect.3.1. However, no previous studies have investigated the possibility of beauty baryon decays violating the $\mathcal{B}$ and $\mathcal{L}$. This study presents the search for the Λ_b and Ξ_b baryon decays to a charged meson and a charged lepton, conserving charge in all decays. No evidence of these decays has been found and the limits indicated above are given. These limits do not violate the predictions of higher generation models [42], which, for B and D decays predict the BNV decay branching ratios of the order below 10^{-28} and 10^{-29}, respectively.

Chapter 6

Background studies for exotic decays

The experimental signature of long-lived exotic particles (LLP) is a displaced vertex (DV) with daughter particles produced at a significant distance from the interaction point of the incoming proton beams.

The reconstructed displaced vertices might be formed from b–hadrons produced in SM processes $pp \rightarrow b\bar{b}X$. Owing to their significant cross section, they are the dominant source of expected background. Hence, an identification of b–hadrons and precision measurements of their properties are crucial for understanding and normalizing the backgrounds for measurements of higher-mass objects that decay into $b\bar{b}$. In addition, theoretical predictions have to be experimentally verified, since they are an integral part of any particle physics experiment, being a helpful tool for designing the detectors and defining their experimental performance.

The measurements performed in pp collisions in different rapidity ranges are generally consistent with the theoretical calculations. However, the comparisons are affected by large theoretical uncertainties (see Sect.3.2).

Within the framework of the LHCb software, external MC generators are incorporated to include theoretical models for pp collisions. As it has been described in Sect.2.3.1, the b–quark production cross section can be computed at NLO accuracy in a pQCD expansion. The key issue is to handle the higher terms in the perturbation series in a proper way, supporting the NLO matrix-element/parton-shower merging procedure. For this purpose, special methods have been proposed for introducing the NLO calculations into the parton shower algorithms. One of them is the POWHEG, implemented in a general computer framework called POWHEG-BOX.

For the studies described in this dissertation, which are among others dedicated to the $b\bar{b}$ production cross section with inclusive final states, the POWHEG has been incorporated to generate and simulate what is observed in a detector by means of a given physics process. As a result, the $b\bar{b}$ and $c\bar{c}$ production cross sections have been measured and the kinematic characteristics of the background have been investigated using the seed-based method.

This chapter describes the Author's implementation of POWHEG to the research in question, namely the exotic decays. At first the special MC samples used are discussed and the measurement of $\sigma(b\bar{b})$ with inclusive final states is described. The central part of this chapter provides a discussion of obtained

characteristics of the generated b-hadrons and of the reconstructed b candidate vertices between the PYTHIA and POWHEG generators. Finally, the chapter is concluded with brief argumentation how this findings could shed some light on the subject of the exotic searches at LHCb.

6.1 Event simulation using POWHEG

The PYTHIA generator provides only the LO calculations of the $b\bar{b}$ and $c\bar{c}$ production. For this reason, its use might only be reasonable to generate samples for the detector acceptance and efficiency studies. Therefore the POWHEG-BOX, which includes calculations at NLO level, is justified to be used to compare the angular characteristics on data with theoretical expectations. The discussion on calculations of the bottom production cross section at the LHC environment is given in Sect.2.3, while the basic ideas of the integration of the NLO calculations with MC event generators are described in Sect.2.3.1.

The PYTHIA as a general purpose event generator is one of the main MC event generators employed in the GAUSS simulation project. Using its LHE interface, the POWHEG method made it possible to perform MC event simulation at NLO accuracy in the official LHCb MC production campaign. The implementation of this issue is based on incorporating the POWHEG-BOX generator and its interfacing with the PYTHIA production tool. The way of interfacing the POWHEG-BOX with the LHCb generator software package, performed by the Author of this dissertation, is described in Appendix A.0.2.

The MC production in the LHCb collaboration is provided centrally by the respective team. The production is performed according to the needs of each analysis team, giving the event type and required statistics to the production system. A substantial part of the MC samples used in the measurement described in the present work has been prepared centrally. However, the local test production has been performed by the Author of this dissertation using the computing resources of ACK CYFRONET AGH [116]. This has been done before the official release of the software package of POWHEG-BOX interface to the LHCb simulation chain, after which the central production could be performed. The statistics of the simulated sample, used in the analysis of the data collected in 2011, are summarized in Tab.6.1. The generator and production types, together with PYTHIA or POWHEG-BOX as the generator, and the *central* or *local* production are specified. The statistics are given for a different event types with reference to the analysis they are dedicated to.

TABLE 6.1: MC samples used in the analysis of data collected in 2011.

Event type	MC sample production	Number of events	Related analyses
$b\bar{b}$ inclusive	*Central* PYTHIA 6&8	4 M	[54] [117] [25]
$b\bar{b}$ inclusive	*Central* POWHEG-BOX	9 M	[54] [117] [25]
$b\bar{b}$ inclusive	*Local* POWHEG-BOX	9 M	[54] [117]
$c\bar{c}$ inclusive	*Central* PYTHIA 6&8	5 M	[54] [117]
$Wb\bar{b}$	*Local* POWHEG-BOX	1.5 M	[117]
WZ	*Local* POWHEG-BOX	1.5 M	[117]
$t\bar{t}$	*Local* POWHEG-BOX	3 M	[117]

6.2 Measurement of $\sigma(b\bar{b})$ with inclusive final states

Experimentally, one can study the production of a bottom quark either from exclusively reconstructed b–hadrons or from secondary vertices identified as decay vertices of b–hadron. The method used in this measurement is based on the latter. Since the b–quark carries heavy mass, the b–hadron characteristics are close to the the quark level (see Sect.6.2.2). Therefore, the procedure based on the inclusive final states depends less on the fragmentation processes as compared to the measurements based on exclusive decay channels. Furthermore, an important advantage of this method is high statistics, which allows for exploring angular correlations between the $b\bar{b}$ pairs, and a larger kinematical region as compared to exclusive reconstruction. On this basis, the measurement of the $b\bar{b}$ production cross section is performed using inclusive b–hadron SV reconstruction, based on an excellent performance of the LHC*b* vertex detector and tracking system.

Since the procedure described above selects also, though with lower efficiency, an inclusive sample of $c\bar{c}$, the $b\bar{b}$ and $c\bar{c}$ cross sections can be measured simultaneously. These measurements based on data collected in 2010 have been concluded and the results published in [54]. For the time being a similar analysis has already been started to get differential cross section.

6.2.1 Analysis strategy

The analysis starts with selecting events with exactly one reconstructed PV, determined by at least five particles having the hits in the VELO detector. Inclusive b or c candidates, the so-called *seeds*, are the SVs reconstructed from two or three tracks likely to be a part of the decay products of a b– or c–hadron. Hence, the seeds are reconstructed based on the criteria similar to those used for the b–hadron reconstruction.

Since it was found that the trigger efficiency as a function of seed pseudo-rapidity forms a plateau in $\eta \in (2.5 - 4.0)$, this interval has been chosen as the fiducial region of the measurement.

The measurement has been performed using data collected by LHCb in pp collisions at the centre-of-mass energy of 7 TeV corresponding to an integrated luminosity of ~ 18 pb^{-1}, since this analysis considers only events with one PV[20].

In LHCb the pp collisions are simulated using PYTHIA 6.4 as the physics event generator. The latter provides only LO of the $b\bar{b}$ production, and is used in this work only for detector acceptance and efficiency studies. For this purpose, PYTHIA LO simulation of MC event samples of $b\bar{b}$-, $c\bar{c}$-inclusive and light quark (minimum bias) events has been used. In addition, the POWHEG NLO simulation of MC event samples, produced with predictions at the NLO level, has been used to compare the measurement performed on data with theoretical expectations. The comparison of these two MC generators has been performed, including angular and momentum correlations.

The selected data sample composition is evaluated using a BDT discriminant with gradient boost algorithm [106]. Finally, the cross sections based on seed pairs from the fiducial region have been determined, following the formula:

$$\sigma(pp \to b\bar{b}(c\bar{c})X) = \frac{N^{obs}_{2seeds} - N^{bkg}_{2seeds}}{\varepsilon^{b\bar{b}(c\bar{c})} \times \mathcal{L}}, \tag{6.1}$$

where N^{obs}_{2seeds} is the sum of $b\bar{b}$ ($c\bar{c}$), N^{bkg}_{2seeds} is the sum of light quark and fake seeds contributions, $\varepsilon^{b\bar{b}(c\bar{c})}$ is the total efficiency for detecting two seeds, and $\mathcal{L}$ is the luminosity corresponding to the events with exactly one PV.

Seed reconstruction

A seed is reconstructed using tracks with high IP with respect to the reconstructed PV. It is made up of two or three tracks from all the tracks in the event which fulfill the requirements defined for the decay products of a b–hadron. The tracks used to form two- or three-track seeds have to satisfy the following conditions: (i) track momentum > 2.0 GeV/c, (ii) track $p_T > 0.6$ GeV/c, (iii) $\chi^2/ndof < 2.5(3.0)$ of first (second and third) track, (iv) track IP significance (IPS[21]) with respect to PV > 2.5.

Reconstructed seeds are required to have $p_T > 1.0$ GeV and $z_{PV} - z_{SV} > 1$ mm. As follows, they are classified according to the sum of their IPS in the case of two-track seeds, or according to the SV χ^2 for three-track seeds. They have to be *unique*, *i.e.* they are not allowed to share any track with any other seed. In general, the reconstructed seeds are characterized by: (i) seed direction - the direction between PV and SV, (ii) seed four-momentum - a sum of the four-momenta of constituting tracks, (iii) seed invariant mass - the invariant mass of all tracks forming the seed.

In the case of two seeds reconstructed very close in azimuthal angle ($\Delta\phi$), they are most likely originating from the same b–hadron or from the chain $b \to c \to$ hadrons. For this reason, a merging procedure has been applied in order to purify

[20] Data were collected at different average number of interactions per bunch crossing, where its average value was $\mu \approx 1.9$.

[21] IP significance is defined as the IP divided by its error.

the sample. It relies on merging pairs of seeds if the invariant mass of all tracks forming the two seeds is below 5.5 GeV/c^2. The merged seed inherits the best parameters (invariant mass, transverse momentum *etc.*) of the initial two seeds, in the sense that it is formed from three tracks with their minimum distance in $\Delta R = \sqrt{\Delta\eta^2 + \Delta\phi^2}$ with respect to the merged seed direction. The seed merging procedure based on the requirement of the invariant mass of all the tracks of the two seeds is justified, since it removes a large fraction of fake seeds at low $\Delta\phi$. In other words, the requirement on seed invariant mass corresponds mainly to seed pairs having low $\Delta\phi$. Hence, the event selection avoids requirements on the variable that is the point of interest, namely $\Delta\phi$, whose correlation distributions give information on different production mechanisms. In this case it is preferable not to bias this variable.

The fraction of light quark seeds has been verified with MC sample. However, no candidate has been found with two seeds out of the 40M minimum bias simulated events after the trigger requirement.

The validation of the method applied to find the inclusive vertices of b– or c–hadrons has been performed on data. An exclusive decay $B^0 \to D^-\pi^+$ (and subsequent $D^- \to K^+\pi-\pi^-$) was fully reconstructed for $b\bar{b}$, and the sample $D^- \to K^+\pi-\pi^-$ for $c\bar{c}$ validation. The particles in the event not belonging to the fully reconstructed signal have been considered as a pseudo sample of inclusive b–hadrons, and they were used to reconstruct seeds.

Event selection and calibration

At the trigger stage it is requested that at least one of the tracks of the seeds has fired the TOS trigger. The L0, HLT1 and HLT2 trigger lines used for the analysis are listed in Tab.6.2. As indicated in the table, at the HLT trigger level all topological lines decisions have been used.

Since there was no dedicated stripping selection for b-inclusive analyses, the set of stripping lines from B hadron stream has been used.

It has been found that the trigger efficiency as a function of seed pseudorapidity forms a plateau in $\eta \in (2.5 - 4.0)$, hence this interval has been chosen as the fiducial region of the measurement. In addition, for the cross section measurement, the seeds where the constituent tracks have $\Delta R = \sqrt{\Delta\eta^2 + \Delta\phi^2} < 0.8$ with respect to the seed direction and seed pairs with $p_T > 5$ GeV/c have been retained. The pointing angle (defined as the angle between the resultant of the tracks forming the seed and the seed direction) has to be less than 5°.

TABLE 6.2: The trigger lines chosen for the measurement.

Trigger stage	Trigger line
L0	`L0Muon, L0Hadron`
HLT1	`Hlt1Track.*`
HLT2	`Hlt2*.Topo`

The seed energy has been calibrated in bins of its corresponding pseudorapidity using events with exactly one b–hadron and one reconstructed seed in the

MC $b\bar{b}$-inclusive sample. First, the seed energy has been calibrated with respect to the energy of true b–hadron. Afterwards, the seed momentum and transverse momentum have been recalculated according to the corrected energy.

Since a significant discrepancy in the track multiplicity is observed when comparing the data and simulation, a reweighting has been applied likewise.

Seed distributions for heavy quarks ($b\bar{b}$- and $c\bar{c}$-inclusive) differ significantly and this accounts for discriminant power which is important for $b\bar{b}$ cross section estimation. Therefore, the contributions from $b\bar{b}$ and $c\bar{c}$ to the selected seeds have been separated by kinematic characteristics which are determined from the MC, using simulated samples of inclusive $b\bar{b}$ and $c\bar{c}$ from minimum bias events. A MVA discriminant, the Gradient Boosted Decision Tree (BDTG), is built on the basis of the set of the following variables:

- seed transverse momentum,
- seed invariant mass,
- sum of χ^2 (IP) of all the tracks assigned to the seed,
- sum of p_T of the seed constituents with respect to the seed direction.

Fig. 6.1 shows the result of the fit to the BDTG response distribution for the data compared to $b\bar{b}$- and $c\bar{c}$-inclusive contributions, from which a composition of the sample is determined (left plot). The validation on data has been performed by fitting the BDTG response shape for data with shapes extracted from the seeds reconstructed from the set of particles opposite to the exclusive decay $B^0 \to D^-\pi^+$, as described before.

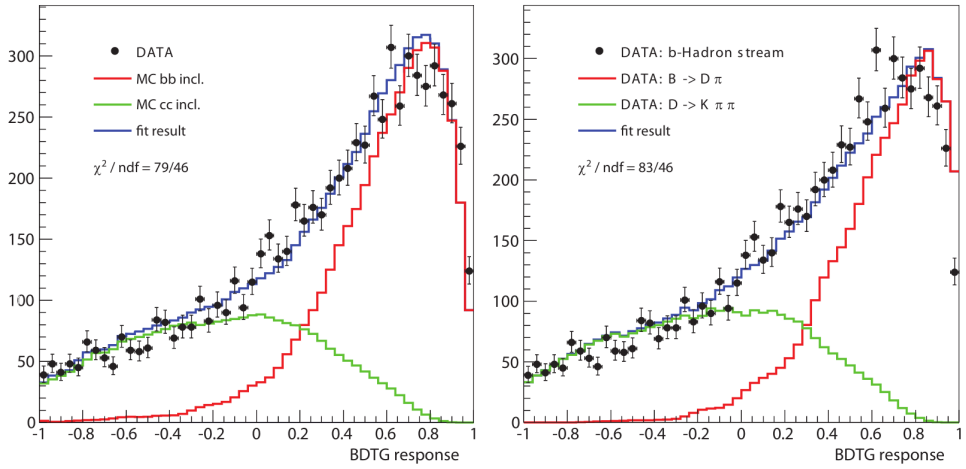

FIGURE 6.1: The BDTG discriminant response for data fitted with distributions obtained from simulation (left) and with shapes extracted from the seeds reconstructed from the set of particles without the ones originating from the reconstructed signal (right), see text for details. The individual contributions are labelled in the legend.

6.2.2 Kinematic characteristics

The three categories of processes describing the hadron production in pp collisions indicated in Sect.2.3 can be identified by their kinematic characteristics, which however differ slightly for different processes. The large samples of $b\bar{b}$ MC simulated events allow us to investigate these characteristics, including the correlations between the b quark and the b–hadron, and between the two b quarks and the two b–hadrons. As follows, the seed-based measurement is based on how well the measured b–hadron approximates the properties of the b quark. The comparison between data and simulation of crucial seed parameters provides a critical test of the proposed method of measurement of the hadron production cross section with inclusive final states.

b–quark / b–hadron correlations

The MC production of inclusive $b\bar{b}$ fully simulated events is used to study the properties of b quarks and b-hadrons. To fully simulate a $b\bar{b}$ event, it is required, at the generator level, that at least one b-hadron is inside the fiducial volume of the spectrometer.

A direct comparison between the b quark and the b–hadron in the pseudorapidity η is presented in Fig.6.2 in terms of the scatter plot of this variable of the b–hadron vs the corresponding quark value for the events simulated inside the LHCb acceptance. It is clearly visible that the b–quark and the b–hadron are very close to each other. This constitutes a direct demonstration how well the heavy hadron approximates the properties of the heavy quark.

Comparisons between the signal and the seeds from data based reconstruction have been performed likewise. Strong correlations in p_T and η between the signal and the seed reconstructed from particles originating from the signal are clearly visible on the left scatter plots in Fig.6.3. The correlation in η disappears while the seeds are reconstructed from particles not belonging to the reconstructed signal (*cf.* plot on the right in Fig.6.3).

Angular and momentum correlations

An essential part of the work described in this dissertation has been devoted to the comparison of the characteristics of the generated b-hadrons with those of the reconstructed seeds between PYTHIA and POWHEG generators. All the distributions are for the events having passed the trigger decision algorithms.

The left plot in Fig.6.4 indicates a different behaviour of the difference in transverse momenta of the two b-hadrons. In the POWHEG sample the two b-hadrons are closer in p_T when compared to PYTHIA. A difference is also observed in the $\Delta\phi$ of the two b–hadrons, plotted on the right of Fig.6.4. The peak at lower $\Delta\phi$ in the POWHEG sample highlights a possible contribution from other mechanisms of $b\bar{b}$ production than the flavour creation, mainly the gluon splitting.

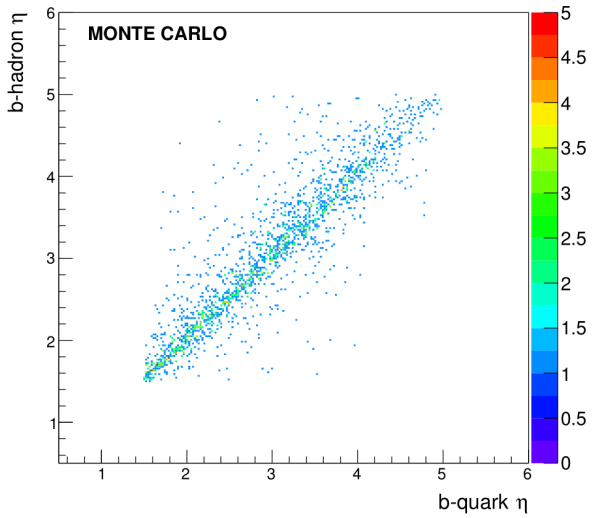

FIGURE 6.2: Correlation in pseudorapidity (η) of the quarks at the production stage vs η of the b–hadron from simulation.

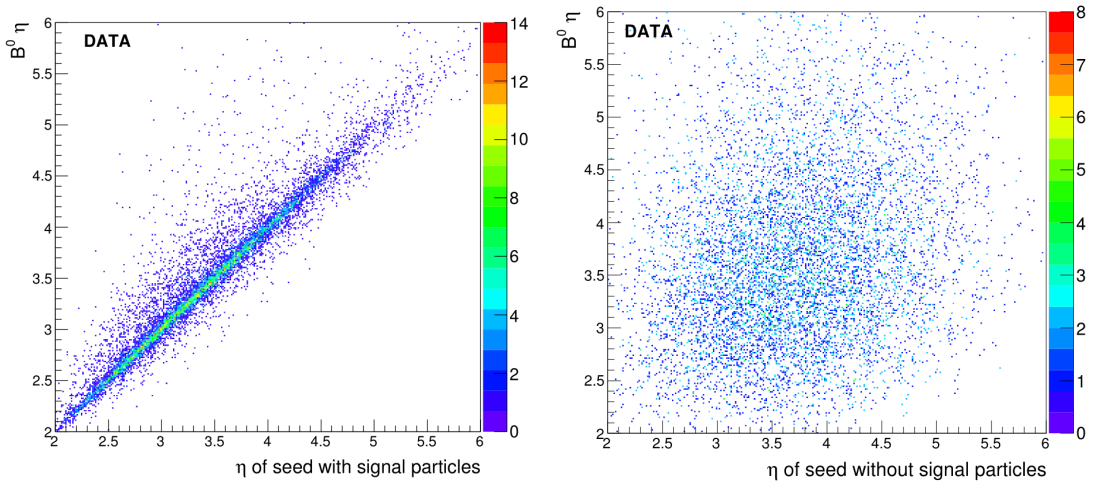

FIGURE 6.3: Correlation in pseudorapidity (η) between $B^0 \to D^-\pi^+$ decay and seeds reconstructed with (left) and without (right) the tracks originating from the signal B^0.

The angular and momentum correlations may provide information on the production subprocesses: for example, at the LO the pair is emitted predominantly in a back-to-back topology (originated from the flavour creation production mechanism), while at the NLO different topologies (such as flavour excitation and gluon splitting) contribute to and interfere with the flavour creation mechanism. The difference in the azimuthal angles ($\Delta\phi$) is correlated in a different way with the gluon splitting mechanism giving $\Delta\phi$ towards $0°$ and flavour excitation contributing in a flatter way, slightly peaking at $180°$.

In Fig. 6.5 $\Delta\phi$ between the two seeds and p_T of each seed are shown, where the data are compared with the expected behaviour from simulated $b\bar{b}$- and $c\bar{c}$-inclusive POWHEG production. The MC statistics were limited at the time of performing this study; however, a reasonable agreement between the data and simulation is observed.

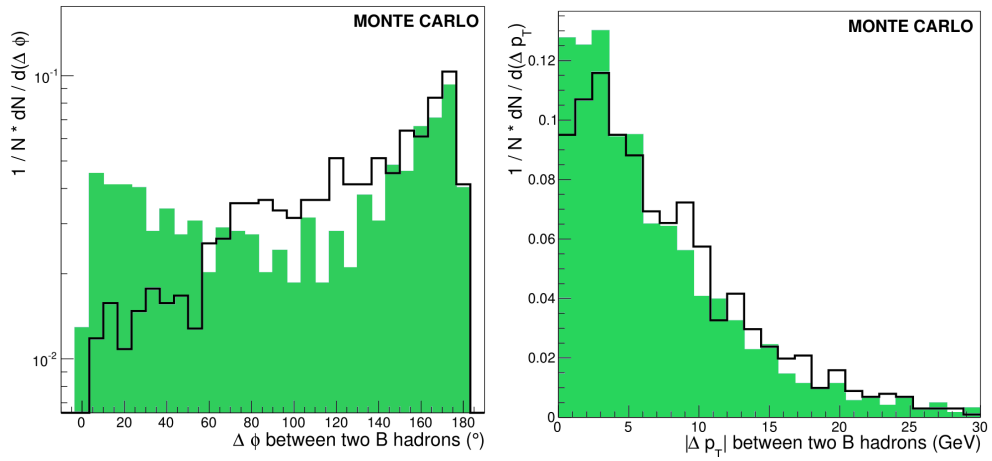

FIGURE 6.4: Difference in azimuthal angles and transverse momentum (taken as an absolute value) of two b–hadrons in the $b\bar{b}$ inclusive events. Distributions are obtained for PYTHIA at the LO approximation (black line) and POWHEG at the NLO approximation (green histogram). Histograms are normalized to 1 and for the $\Delta\phi$ logarithmic scale is used.

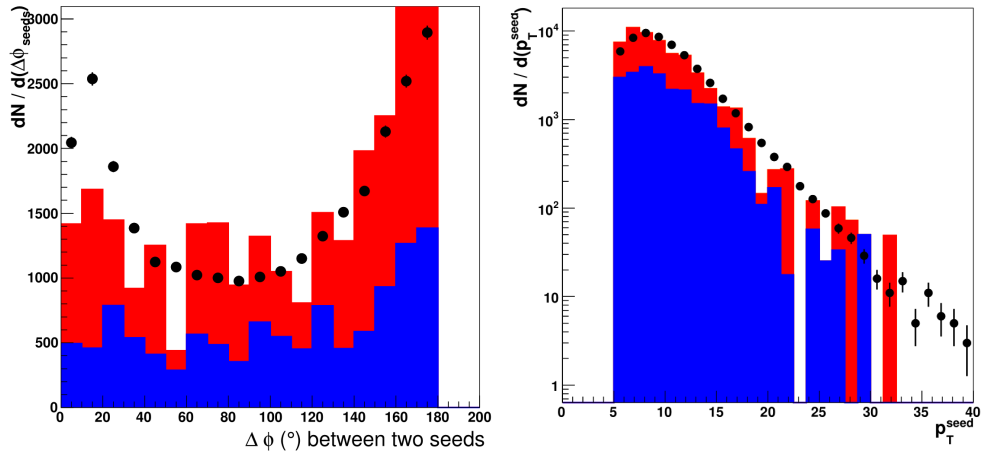

FIGURE 6.5: Difference in azimuthal angles for the two seeds (left) and transverse momentum of the seeds (right). Black dots are the data, the blue histogram is the $c\bar{c}$ contribution and in red the $b\bar{b}$ one added to the previous one is marked. The $b\bar{b}$ contribution is produced with the POWHEG generator while the $c\bar{c}$ with the PYTHIA one.

6.2.3 Results and experimental perspectives

The total efficiency for $b\bar{b}$ and $c\bar{c}$ cross section measurement has been determined as the product of the trigger, stripping and seeding efficiencies, as well as the requirement of seed pairs selection specified in 6.2.1. It amounts to $(6.6 \pm 0.8) \times 10^{-5}$ and $(1.8 \pm 0.2) \times 10^{-5}$ for $b\bar{b}$– and $c\bar{c}$–inclusive, respectively.

As it has been mentioned before, $\mathcal{L}$ is the luminosity corresponding to the event sample with exactly one PV. The fraction of crossings with one PV is estimated by splitting data sample according to the value of the interaction multiplicity per bunch crossings (μ), for which the Poisson probability of one PV has been determined.

The observed number of the selected events with two seeds in the data is 29843. This sample corresponds to a composition of 17757 ± 277 $b\bar{b}$ events and 12086 ± 315 $c\bar{c}$ ones.

Finally, the determined values of cross section read [54]:

$$\sigma(pp \to b\bar{b}X) = (79.7 \pm 1.2 \pm 8.7)\,\mu\mathrm{b}, \tag{6.2}$$

$$\sigma(pp \to c\bar{c}X) = (104.6 \pm 2.7 \pm 11.4)\,\mu\mathrm{b}, \tag{6.3}$$

where the first error is statistical and the second one - systematic. If extrapolated to the full geometrical and kinematical range by applying a factor of 2.72 for extrapolation calculated with POWHEG, one obtains:

$$\sigma(pp \to b\bar{b}X) = (218 \pm 24)\,\mu\mathrm{b}. \tag{6.4}$$

The quoted uncertainty is a sum in quadrature of statistical and systematic uncertainties.

There is an alternative LHC*b* measurement of $\sigma(c\bar{c})$ [118]. However, it was made with an exclusive decay channel in a kinematic range of transverse momentum and rapidity of $(0 < p_T < 8)$ GeV/c and $2 < \eta < 4.5$, respectively. Therefore, these results are only in marginal overlap with the ones used in the analysis described in this thesis.

It is worthwhile to conclude this discussion of the cross section measurement by referring to its experimental perspectives. For searches dedicated to the BSM physics the key issue is to explore the backgrounds. Giving some examples of such searches, already being performed in LHC*b*, there are analyses triggered by models as a hidden valley [25] or mSUGRA [117] with displaced vertices in the final state. All of them exploit the unique LHC*b* experimental environment with long VELO geometry and excellent performance of the whole tracking system.

In the example of the SUSY model of mSugra described in Sect.2.2.2, the search for Higgs-like bosons decaying into long-lived exotic particles is performed on data collected in 2010 corresponding to an integrated luminosity of $35.8\ \mathrm{pb}^{-1}$. The identified DV can be associated with the decay of long-lived neutralino $\widetilde{\chi}_1^0$ and $\widetilde{\chi}_1^0 \to 3\mathrm{quarks}$. From zero signal observed, the upper limit on the production cross-section for a Higgs signal of this model, for different LLP lifetimes, LLP masses and Higgs masses has been computed, given in Tab.6.3. In conclusion, for particular points of the BV model exclusions on production cross-sections have been set.

The measurement of $b\bar{b}$ production cross section together with understanding the properties of background of that kind is a crucial issue when performing searches for exotic decays. This is because the $b\bar{b}$ is the dominant source of visible background. For the time being, the differential cross section measurement is very well motivated work being performed in the LHC*b*. The NLO accuracy in the POWHEG MC generator interfaced with LHC*b* simulation software chain is a kind of a supplementary tool, crucial for understanding what is observed in the detector as a result of the process under study.

TABLE 6.3: Higgs detection efficiencies and 95% CL upper limit on the production cross-section for a Higgs signal of the B-violating (BV) model, for a given LLP lifetimes, LLP masses and Higgs masses. The quoted uncertainties are statistical only. Parameters of the models considered in this study are indicated likewise, where M_1, M_2, $tan\beta$, and μ correspond to standard MSSM parameters [117].

Model	M_1 [GeV/c^2]	M_2 [GeV/c^2]	$tan\beta$	μ [GeV/c^2]	τ_{LLP} [ps]	m_{LLP} [GeV/c^2]	m_{h^0} [GeV/c^2]	ε(%)	σ_{UL} [pb]
BV48	62	250	5	140	10	48	114	0.384 ± 0.007	32
BV48-15	62	250	5	140	10	48	114	0.418 ± 0.017	29
BV20-10	28	250	5	140	10	20	114	0.010 ± 0.003	1425
BV35-10	46	250	5	140	10	35	114	0.146 ± 0.010	84

Chapter 7

Summary and Conclusions

The present thesis is concentrated on the search for the baryon and lepton number violation phenomenon in $X_b \to K^-\mu^+$ ($X = \Lambda_b, \Xi_b^0$) decay using data collected in 2011 and 2012 by the LHC*b* collaboration at LHC. Studies of BNV are of paramount importance to elucidate new theories constituting the extensions of the SM and to shed some light on such phenomena like baryogenesis. This study offers the first direct probe of BNV processes involving beauty heavy baryons in the initial state. No statistically significant signal of the decay $X_b \to K^-\mu^+$ has been found and, as a result, the following upper limits on the branching ratios were set: $\mathcal{B}(\Lambda_b \to K^-\mu^+) < 3.6 \times 10^{-9}$ at 95% CL and $\mathcal{B}(\Xi_b^0 \to K^-\mu^+) < 1.8 \times 10^{-8}$ at 95% CL.

The selection criteria were implemented for the signal decay mode $X_b \to K^-\mu^+$ and for the normalization channel, which was $\Lambda_b \to pK^-$. The discrimination between a potential signal of the decay in question and the background was based mostly on multivariate classifiers. Furthermore, the analysis required a thorough discussion of trigger lines to be applied as well as careful studies of various background sources. The latter was performed using MC events. In particular the background source originating from $B \to h^+h'^-$ decays was found to be the most pronounced in this study.

The other part of the thesis is concentrated on the background studies for exotic searches. Direct and indirect searches for the existence of BSM particles can be performed at the LHC*b* spectrometer exploiting its unique forward acceptance, high vertex and momentum resolution, and excellent particle identification. The LHC*b* collaboration has already performed a series of such searches, where the studies of the expected background from $pp \to b\bar{b}X$ produced in the SM processes play the crucial role.

The seed-based measurement of $\sigma(b\bar{b}, c\bar{c})$ with b-(c-)hadron inclusive final states, performed with data collected in 2010 by the LHC*b* collaboration at LHC, has been described. The determined values of cross section in the fiducial volume are: $\sigma(pp \to b\bar{b}X) = (79.7 \pm 1.2 \pm 8.7)\,\mu$b, $\sigma(pp \to c\bar{c}X) = (104.6 \pm 2.7 \pm 11.4)\,\mu$b. As the main purpose of this part of the dissertation the kinematic characteristics for the hadron production in pp collisions have been obtained. This was possible after the interfacing the new external generator, the POWHEG-BOX, into the LHC*b* software chain by the Author. These characteristics are given with b–quark / b–hadron correlations together with angular and momentum correlations, both for two different generators, namely the PYTHIA and POWHEG. The angular and momentum correlations highlight a possible contribution from

other mechanisms of $b\bar{b}$ production than the flavour creation, mainly the gluon splitting.

All results from searches for exotica at LHC*b* are consistent with the SM expectation. Having so, upper limits have been set to the corresponding production cross-sections of a given model under study.

It is worthwhile to express the fact that Run 2 of the LHC is now well under the luminosity production time. By the end of 2018, LHC*b* expects to have accumulated about $5\ \mathrm{fb}^{-1}$ of integrated luminosity at a centre-of-mass energy of $\sqrt{s} = 13\ \mathrm{TeV}$. The combination of higher luminosity and larger cross-sections should lead to a four-fold increase in statistics relative to Run 1. It will be interesting to see how many of the possible anomalies will stand the test of time.

Appendix A

The LHC*b* software framework

LHC*b* uses a common GAUDI software framework [119] for the data acquisition, simulation and physics analysis that is experiment independent. In addition, there are several different software tools dedicated to specific tasks.

A.0.1 Data and MC processing

A complete LHC*b* application chain and data flow are illustrated in Fig. A.1. The simulation of MC data is performed within the GAUSS project [120, 29]. The pp collisions are generated using external generators (*e.g.* PYTHIA [121]) with decay models handled with EVTGEN [122]. The interactions of the final state particles in the detector are implemented with a GEANT4 simulation [123], including the detector geometry description.

The MOORE project [124] includes all high-level trigger algorithms. The digitisation of the hits in the individual subdetectors is handled in the BOOLE project [125], which constitutes the final stage of the LHC*b* detector simulation. BRUNEL [77] is a reconstruction application that can process identically the results of the BOOLE digitization and data directly from the acquisition system. From this stage of data processing, files containing all reconstructed items, such as calorimeter and trackers clusters, charged tracks, as well as information on particle identification from the RICH, calorimeter and muon subsystems are stored as the so-called DST files. Finally, the DAVINCI application [78] is an analysis framework which supports the selection of events and analysis proceeding from further processing of the DST data. In this package, both the stripping algorithms and the physics analysis software tools are grouped together.

A.0.2 POWHEG interface with the LHC*b* simulation chain

The GAUSS as a simulation application consists of two independent phases, the generation of the primary event and the tracking of produced particles through the detector [29]. At the first step, the event generator as the special external engine plays its own role. At this point, the dedicated interfaces to call external generators are used, which provide tools to steer the execution of different generation sequences. The generation algorithm uses tools that can be plugged in, carrying out specific actions, including the production of N pp interactions (*Production Tool*), generation of a given event sample

(*Sample Generation Tool*), or a decay of unstable particles (*Decay Tool*). Such a tool structure allows different MC generators to be employed for producing events. Furthermore, there is a possibility to use text files (*e.g.* the so-called LHE format) containing parton level events as the production engines. These events, produced in one generator, can then be subsequently fed to parton shower and hadronization phases performed by the other generator, *i.e.* the PYTHIA one - the main generator employed in the LHC*b* simulation framework.

To interface the POWHEG generator, the POWHEG-BOX program [34, 35] has been incorporated. It is a framework with implementation of the theoretical construction of the POWHEG method. Its interface with the GAUSS project includes a new package called `LbPowheg`, which has been written by the Author of the present thesis, following the standard of the configuration management tool of the LHC*b* software facility. The logic of signal sample generation is a special simplified adaptation of the scheme provided in [126].

New *Special Production Tools* for the generation algorithm are coded, each dedicated to a given process available in the POWHEG-BOX. The production tool sets up the hard process, generation of multiple parton-parton interactions and evolution of the partons, up to the formation of hadrons. This is carried out by calling an external generator, *i.e.* the PYTHIA one. However, the POWHEG-BOX is called as the subprocess to generate the hardest emission at first, which is fed into the PYTHIA by storing the hard event information according to the conventions of the Les Houches Event interface [127]. The flowchart showing the simulation chain including the POWHEG-BOX stage is shown in Fig.A.1.

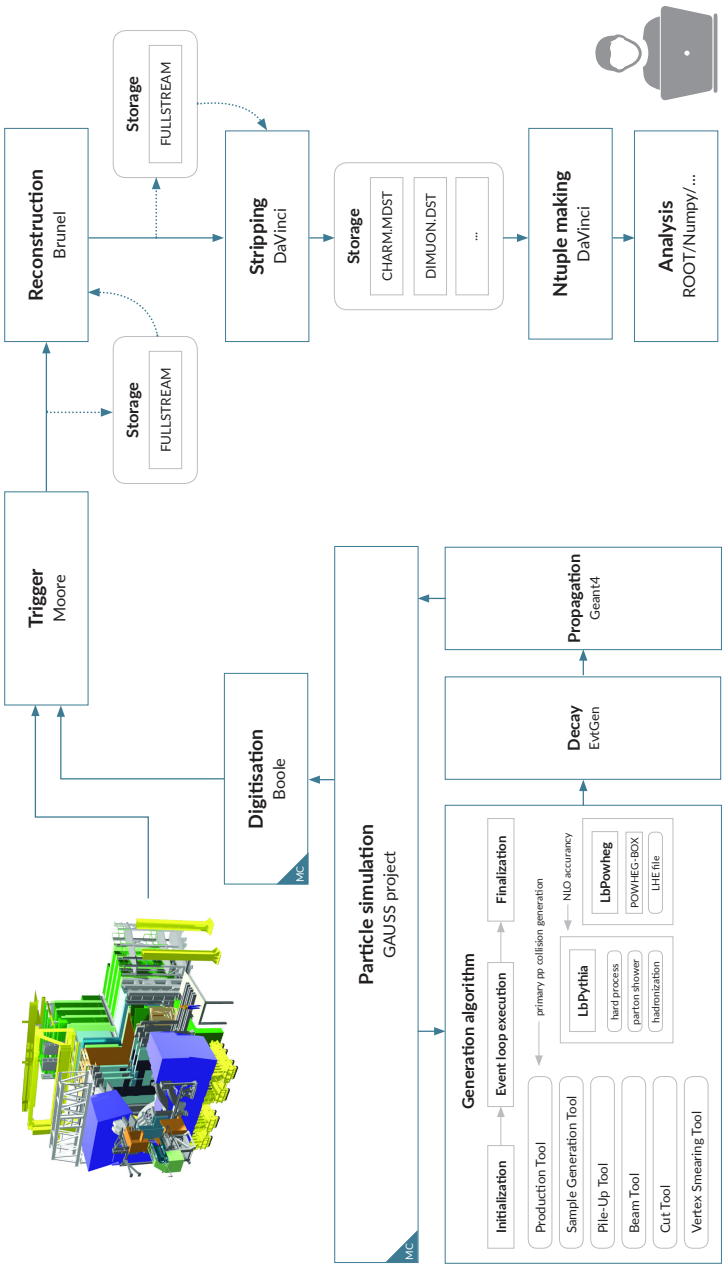

FIGURE A.1: The LHC*b* data processing applications and data flow.

A.0.3 Technical specification of the data and MC samples processing

TABLE A.1: Versions of the LHC*b* applications used for the analysis of data.

Application Name	Version	Purpose
BRUNEL	v43r2	central reconstruction of the data
DAVINCI	v32r2	central stripping selection of the data
DAVINCI	v36r1	physics analysis tools

TABLE A.2: Stripping lines used for the analysis of data.

Stripping Line Name	Purpose
StrippingBLVLinesLb2KmuLine	$X_b \to K^- \mu^+$
StrippingBs2MuMuLinesNoMuIDLine	$B^0 \to K^+ \pi^-$
	$\Lambda_b \to p\ K^-$
StrippingBs2MuMuLinesBu2JPsiKLine	$B^- \to J/\psi\ (\mu^+\mu^-)K^-$

TABLE A.3: MC event types used for the analysis of data. An event type numbering is the explicit LHC*b* internal scheme for MC datasets which describes the way a sample was produced [128]. All samples were generated with PYTHIA 8, where the appropriate TCKs were chosen to describe the most common trigger conditions throughout the respective year, the 0x40760037 and 0x409f0045 for 2011 and 2012, respectively.

Process	Event type
$\Lambda_b \to K^- \mu^+$	15112001
$\Xi_b^0 \to K^- \mu^+$	16112041
$\Lambda_b \to pK^-$	15102001
$B^0 \to K^+ \pi^-$	11102001
$\Lambda_b \to p\pi^-$	15102011
$B_s^0 \to K^- \pi^+$	13102013
$B^- \to J/\psi\, K^-$	12143001
$B_s^0 \to K^+ K^-$	13102002
$B^0 \to \pi^+ \pi^-$	11102013

Appendix B

Supplement distributions

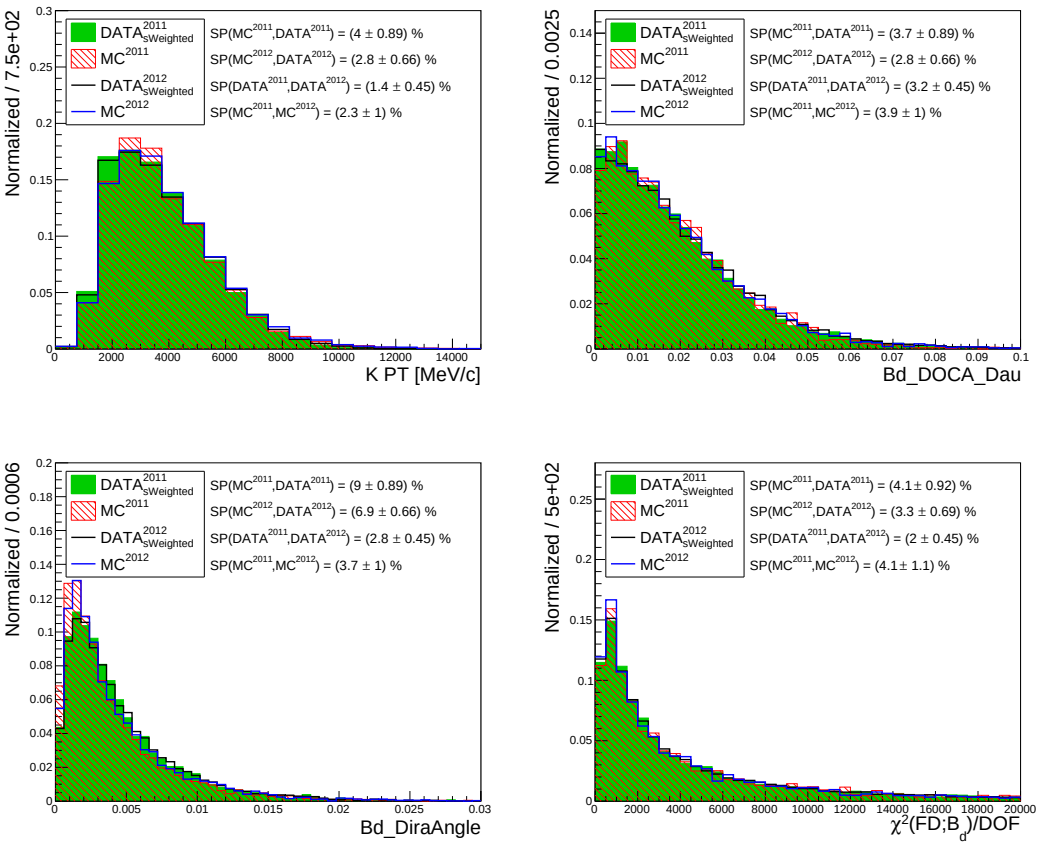

FIGURE B.1: MC/Data discrepancies of keys variables extracted from control channel dataset. The variables were defined in Sect.5.3.1, while the SP value is extracted according to Eq.5.7. The value of SP is given for quantitative comparison of different datasets. The individual distributions are labelled in the legend.

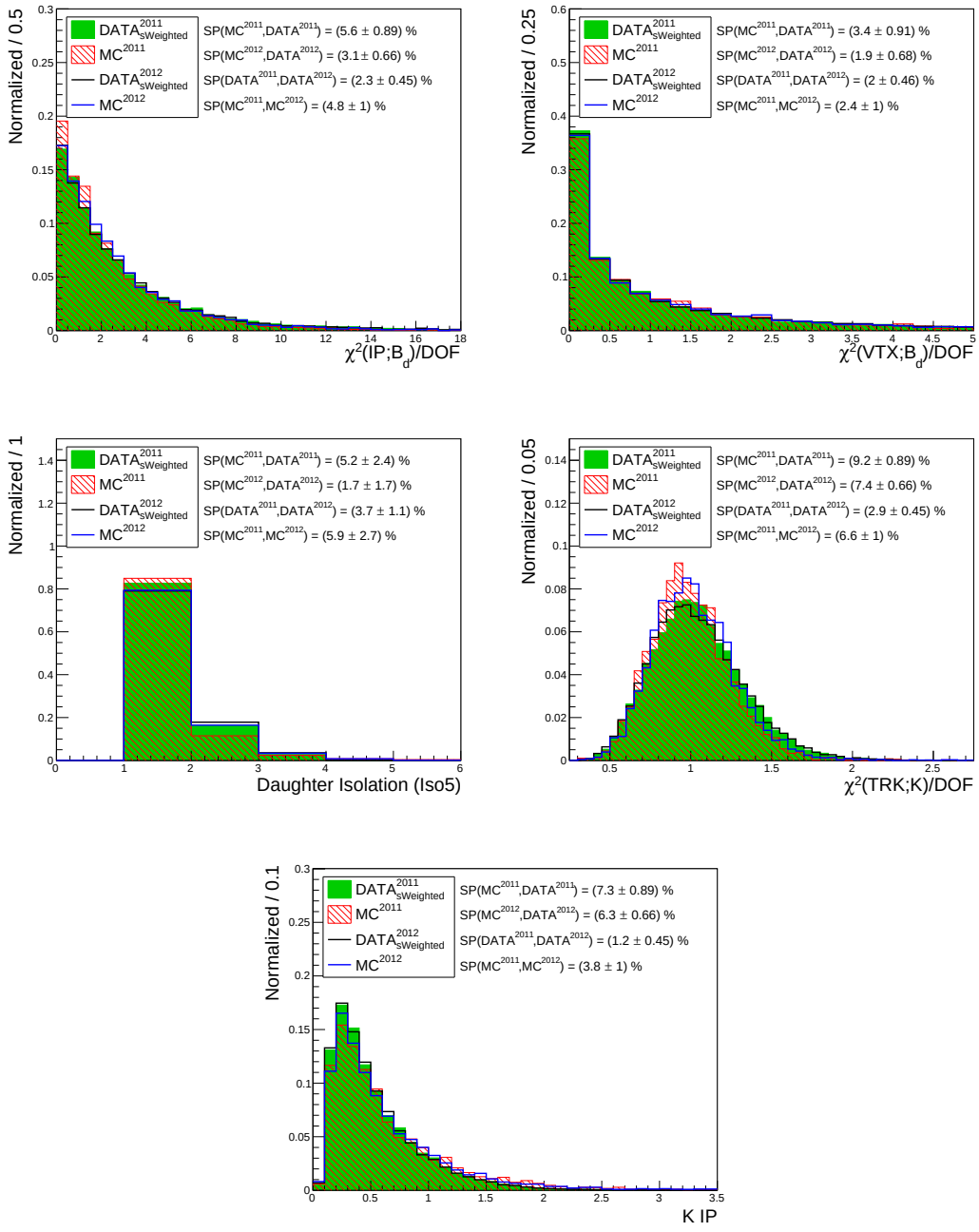

FIGURE B.2: MC/Data discrepancies of keys variables extracted from control channel dataset. The variables were defined in Sect.5.3.1, while the SP value is extracted according to Eq.5.7. The value of SP is given for quantitative comparison of different datasets. The individual distributions are labelled in the legend.

Appendix C

Employed Statistical Tools

C.0.1 ${}_s\mathcal{P}\mathrm{lot}$ technique

In an attempt to have access to the distribution of a given variable that is considered as truly unknown in data, one needs to unfold the contributions of different sources. The ${}_s\mathcal{P}\mathrm{lot}$ technique allows us to enhance the contributions to the data sample of particular sources of events, *i.e.* it gratifies to build histograms in giving variable keeping all signal events while getting rid of all background events, and keeping track of the statistical uncertainties. Full details of the calculations applied to this approach may be found in reference [107]; here general ideas behind ${}_s\mathcal{P}\mathrm{lot}$ technique are described.

The ${}_s\mathcal{P}\mathrm{lot}$ tool applies in the context of an unbinned extended maximum Likelihood fit which is undertaken on the data to determine the yields of the various sources, merged into a single sample of events. The events are assumed to be characterized by the *discriminating* variable (*i.e.* a variable for which the distribution of all the sources of events is known) and the *control* variable (*i.e.* a variable for which the distribution of some sources is considered as truly unknown). The aim of the ${}_s\mathcal{P}\mathrm{lot}$ is to use the knowledge about the discriminating variable to infer the behaviour of the individual sources of events with respect to the control variable.

The crucial point for the reliability of the ${}_s\mathcal{P}\mathrm{lot}$ analysis is to use an exhaustive list of sources of events ($N_k, k \in (1 \ldots N_s)$) populating the data sample combined with an accurate description of the PDFs ($f_i, i \in (1 \ldots N_s)$). If all the f_i PDFs of the discriminating variable are found, the yields N_i can be extracted and the statistical technique ${}_s\mathcal{P}\mathrm{lot}$ can be applied to unfold the true distribution of a control variable for any of the N_s species. This can be obtained with assigning to all events (y_e) the so-called sWeight which is defined as follows:

$$ {}_s\mathcal{P}_{\mathrm{n}}(y_e) = \frac{\sum_{i=1}^{N_s} \mathbf{V}_{\mathrm{n}i} f_i(y_e)}{\sum_{k=1}^{N_s} N_k f_k(y_e)}. \tag{C.1} $$

In final, an estimate of the true x–distribution of the species labelled $\tilde{M}_n$ may be obtained by histogramming events, using sWeight:

$$ N_{\mathrm{n}s}\tilde{M}_{\mathrm{n}}(\bar{x})\delta x \equiv \sum_{e \subset \delta x_s} \mathcal{P}_{\mathrm{n}}(y_e), \tag{C.2} $$

where the sum runs over the events for which the x value lies in the bin centered on $\bar{x}$ and total width δx. On average, one readily reproduces the true binned distribution labelled $\mathbf{M}_n$:

$$\left\langle N_{\mathrm{n}s}\tilde{M}_{\mathrm{n}}(x)\right\rangle \equiv N_{\mathrm{n}}\mathbf{M}_{\mathrm{n}}(x). \tag{C.3}$$

The inverse of the covariance matrix $\mathbf{V}_{ij}$ entering the sWeight formula is given by the second derivatives of log-Likelihood ($-\mathcal{L}$) maximized beforehand to determine the free parameters designed to tune the PDFs on the data sample. The origin of this covariance matrix is in fact the case of the two sets of variables x and y are uncorrelated.

The main properties of the above quoted formalism rely on maximizing the likelihood, which implies that each x–distribution is properly normalized, and in effect for any event:

$$\sum_{l=1\ s}^{N_s} \mathcal{P}_{\mathrm{n}}(y_e) = 1. \tag{C.4}$$

The ${}_s\mathcal{P}\mathrm{lot}$ provides a consistent representation of how all events from the various species are distributed in the control variable. It is worth emphasizing that the obtained reconstructed distribution is pure in a statistical sense: it is free from potential background arising from the other species. In fact, the more discriminating variable is employed, the clearer the ${}_s\mathcal{P}\mathrm{lot}$ is.

The technique is available in the ROOT framework, which has been used in the work described in this thesis.

C.0.2 CL_s technique

When interpreting the result of an experiment, one has to do with hypothesis testing and the derivation of upper limits. To exclude a possible signal or to compute the significance of one that is observed, the measured data must be compared with the predictions of a model which includes new physics, and also a model which does not, to see which of the two (if either) can be excluded and at what confidence level.

The CL_s method [115] is based on the study of two hypotheses: the so called "signal plus background" (denoted as $s+b$) and the null "background only" hypothesis (marked as b). The former describes the cases in which the observed spectrum can be explained in the presence of signal and background components. The latter corresponds to the existence of the background contribution with the lack of the signal. The observed confidence levels for these two hypotheses read:

$$\mathrm{CL_{s+b}} = \mathrm{P_{s+b}}(\mathrm{Q} < \mathrm{Q_{obs}}) = \int_{-\infty}^{\mathrm{Q_{obs}}} \frac{\mathrm{dP_{s+b}}}{\mathrm{dQ}}\mathrm{dQ}, \tag{C.5}$$

$$\mathrm{CL_{b}} = \mathrm{P_{b}}(\mathrm{Q} < \mathrm{Q_{obs}}) = \int_{-\infty}^{\mathrm{Q_{obs}}} \frac{\mathrm{dP_{b}}}{\mathrm{dQ}}\mathrm{dQ}, \tag{C.6}$$

where $\frac{dP_{s+b}}{dQ}$ and $\frac{dP_b}{dQ}$ are the probability distribution functions (PDFs) for the two corresponding hypotheses and Q is called the test statistics. The CL_s value is defined as the ratio between the confidence level for the signal plus background hypothesis to the confidence level for the background hypothesis:

$$\mathrm{CL}_s = \frac{\mathrm{CL_{s+b}}}{\mathrm{CL_b}}. \tag{C.7}$$

The limits obtained with the CL_s method are easily combinable and conservative in the presence of a downward fluctuation of the number of detected signal candidates. When multiple results are combined, the PDFs in Equations C.5 and C.6 are the product of the individual PDFs,

$$\mathrm{CL}_s = \frac{\prod_{\mathrm{i=1}}^{\mathrm{N_{chan}}} \sum_{\mathrm{n=0}}^{\mathrm{n_i}} \frac{\mathrm{e}^{-(\mathrm{s_i}+\mathrm{b_i})}(\mathrm{s_i}+\mathrm{b_i})^{\mathrm{n}}}{\mathrm{n!}}}{\prod_{\mathrm{i=1}}^{\mathrm{N_{chan}}} \sum_{\mathrm{n=0}}^{\mathrm{n_i}} \frac{\mathrm{e}^{-\mathrm{b_i}}\mathrm{b_i^n}}{\mathrm{n!}}} \cdot \frac{\prod_{\mathrm{j=1}}^{\mathrm{n}} \mathrm{s_i S_i(x_{ij})} + \mathrm{b_i B_i(x_{ij})}}{\prod_{\mathrm{j=1}}^{\mathrm{n}} \mathrm{B_i(x_{ij})}}, \tag{C.8}$$

where N_{chan} is the number of results (or decay channels) and for each channel i, n_i is the number of the observed candidates, s_i and b_i are the numbers of signal and background events and S_i , B_i are the PDFs of the discriminating variables. The x_{ij} are the values of the discriminating variables (with index j).

The technique is implemented by Tom Junk [108] and is available in the ROOT framework which has been used in the work described in this thesis. For each dataset the number of expected signal events was estimated using the formula defined in Sect.5.6, which gives:

$$s_i = \frac{\mathcal{B}(X_b \to K^-\mu^+)}{\alpha_{X_b}}, \tag{C.9}$$

where $\mathcal{B}(X_b \to K^-\mu^+)$ is the branching fraction of the searched process and α_{X_b} is the so-called normalization factor.

The signals and backgrounds may depend on a variety of parameters which are not of primary interest (the so-called *nuisance parameters*) but which are needed for the measurement, *e.g.* efficiencies, acceptances, integrated luminosity, and background production cross sections. Their values are needed in order to extract measurements of, or limits on, the parameters of interest, and uncertainty in their values usually results in reduced sensitivity to the parameters of interest. The systematic errors on observables are parametrized in terms of these nuisance parameters. Their systematic uncertainties are evaluated using MC method by running several simulations with different values of nuisance parameters (s_i, b_i). The values are varied according to Gaussian distribution with the width equal to the corresponding systematic uncertainty.

List of Figures

List of Tables

Bibliography

[1] K. A. Olive et al. "Review of Particle Physics". In: *Chin. Phys.* C38 (2014), p. 090001. DOI: 10.1088/1674-1137/38/9/090001.

[2] Abdus Salam. "Weak and Electromagnetic Interactions". In: *Conf. Proc.* C680519 (1968), pp. 367–377.

[3] Steven Weinberg. "A Model of Leptons". In: *Phys. Rev. Lett.* 19 (1967), pp. 1264–1266. DOI: 10.1103/PhysRevLett.19.1264.

[4] S. L. Glashow. "Partial Symmetries of Weak Interactions". In: *Nucl. Phys.* 22 (1961), pp. 579–588. DOI: 10.1016/0029-5582(61)90469-2.

[5] Gerard 't Hooft. "Renormalizable Lagrangians for Massive Yang-Mills Fields". In: *Nucl. Phys.* B35 (1971), pp. 167–188. DOI: 10.1016/0550-3213(71)90139-8.

[6] Peter W. Higgs. "Broken Symmetries and the Masses of Gauge Bosons". In: *Phys. Rev. Lett.* 13 (16 1964), pp. 508–509. DOI: 10.1103/PhysRevLett.13.508. URL: http://link.aps.org/doi/10.1103/PhysRevLett.13.508.

[7] F. Englert and R. Brout. "Broken Symmetry and the Mass of Gauge Vector Mesons". In: *Phys. Rev. Lett.* 13 (9 1964), pp. 321–323. DOI: 10.1103/PhysRevLett.13.321. URL: http://link.aps.org/doi/10.1103/PhysRevLett.13.321.

[8] http://home.cern/about/experiments/atlas.

[9] http://home.cern/about/experiments/cms.

[10] M. J. G. Veltman. "The Infrared - Ultraviolet Connection". In: *Acta Phys. Polon.* B12 (1981), p. 437.

[11] A. D. Sakharov. "Violation of CP Invariance, c Asymmetry, and Baryon Asymmetry of the Universe". In: *Pisma Zh. Eksp. Teor. Fiz.* 5 (1967). [Usp. Fiz. Nauk161,61(1991)], pp. 32–35. DOI: 10.1070/PU1991v034n05ABEH002497.

[12] G. Hinshaw et al. "Nine-Year Wilkinson Microwave Anisotropy Probe (WMAP) Observations: Cosmological Parameter Results". In: *Astrophys. J. Suppl.* 208 (2013), p. 19. DOI: 10.1088/0067-0049/208/2/19. arXiv: 1212.5226 [astro-ph.CO].

[13] B. P. Abbott et al. "Observation of Gravitational Waves from a Binary Black Hole Merger". In: *Phys. Rev. Lett.* 116.6 (2016), p. 061102. DOI: 10.1103/PhysRevLett.116.061102. arXiv: 1602.03837 [gr-qc].

[14] A. Kashlinsky. "LIGO gravitational wave detection, primordial black holes and the near-IR cosmic infrared background anisotropies". In: *Astrophys. J.* 823.2 (2016), p. L25. DOI: 10.3847/2041-8205/823/2/L25. arXiv: 1605.04023 [astro-ph.CO].

[15] Gianfranco Bertone, Dan Hooper, and Joseph Silk. "Particle dark matter: Evidence, candidates and constraints". In: *Phys. Rept.* 405 (2005), pp. 279–390. DOI: 10.1016/j.physrep.2004.08.031. arXiv: hep-ph/0404175 [hep-ph].

[16] H. Georgi and S. L. Glashow. "Unity of All Elementary Particle Forces". In: *Phys. Rev. Lett.* 32 (1974), pp. 438–441. DOI: 10.1103/PhysRevLett.32.438.

[17] Stephen P. Martin. "A Supersymmetry primer". In: (1997). [Adv. Ser. Direct. High Energy Phys.18,1(1998)]. DOI: 10.1142/9789812839657_0001,10.1142/9789814307505_0001. arXiv: hep-ph/9709356 [hep-ph].

[18] Burt A. Ovrut, Austin Purves, and Sogee Spinner. "The minimal SUSY $B - L$ model: from the unification scale to the LHC". In: *JHEP* 06 (2015), p. 182. DOI: 10.1007/JHEP06(2015)182. arXiv: 1503.01473 [hep-ph].

[19] Nobuchika Okada and Nathan Papapietro. "R-parity Conserving Minimal SUSY $B - L$ Model". In: (2016). arXiv: 1603.01769 [hep-ph].

[20] Herbert K. Dreiner and Graham G. Ross. "R-parity violation at hadron colliders". In: *Nucl. Phys.* B365 (1991), pp. 597–613. DOI: 10.1016/0550-3213(91)90443-2.

[21] Linda M. Carpenter, David E. Kaplan, and Eun-Jung Rhee. "Reduced fine-tuning in supersymmetry with R-parity violation". In: *Phys. Rev. Lett.* 99 (2007), p. 211801. DOI: 10.1103/PhysRevLett.99.211801. arXiv: hep-ph/0607204 [hep-ph].

[22] Hitoshi Murayama. "Supersymmetry phenomenology". In: *Particle physics. Proceedings, Summer School, Trieste, Italy, June 21-July 9, 1999*. 2000, pp. 296–335. arXiv: hep-ph/0002232 [hep-ph]. URL: http://alice.cern.ch/format/showfull?sysnb=2177492.

[23] Jonathan M. Butterworth et al. "Discovering baryon-number violating neutralino decays at the LHC". In: *Phys. Rev. Lett.* 103 (2009), p. 241803. DOI: 10.1103/PhysRevLett.103.241803. arXiv: 0906.0728 [hep-ph].

[24] S. Dittmaier et al. "Handbook of LHC Higgs Cross Sections: 1. Inclusive Observables". In: (2011). DOI: 10.5170/CERN-2011-002. arXiv: 1101.0593 [hep-ph].

[25] Roel Aaij et al. "Search for long-lived particles decaying to jet pairs". In: *Eur. Phys. J.* C75.4 (2015), p. 152. DOI: 10.1140/epjc/s10052-015-3344-6. arXiv: 1412.3021 [hep-ex].

[26] Matteo Cacciari and Paolo Nason. "Is there a significant excess in bottom hadroproduction at the Tevatron?" In: *Phys. Rev. Lett.* 89 (2002), p. 122003. DOI: 10.1103/PhysRevLett.89.122003. arXiv: hep-ph/0204025 [hep-ph].

[27] Andy Buckley et al. "General-purpose event generators for LHC physics". In: *Phys. Rept.* 504 (2011), pp. 145–233. DOI: 10.1016/j.physrep.2011.03.005. arXiv: 1101.2599 [hep-ph].

[28] E. Norrbin and T. Sjostrand. "Production and hadronization of heavy quarks". In: *Eur. Phys. J.* C17 (2000), pp. 137–161. DOI: 10.1007/s100520000460. arXiv: hep-ph/0005110 [hep-ph].

[29] M. Clemencic et al. "The LHCb simulation application, Gauss: Design, evolution and experience". In: *J. Phys. Conf. Ser.* 331 (2011), p. 032023. DOI: 10.1088/1742-6596/331/3/032023.

[30] Stefano Frixione and Bryan R. Webber. "Matching NLO QCD computations and parton shower simulations". In: *JHEP* 06 (2002), p. 029. DOI: 10.1088/1126-6708/2002/06/029. arXiv: hep-ph/0204244 [hep-ph].

[31] Stefano Frixione, Paolo Nason, and Carlo Oleari. "Matching NLO QCD computations with Parton Shower simulations: the POWHEG method". In: *JHEP* 11 (2007), p. 070. DOI: 10.1088/1126-6708/2007/11/070. arXiv: 0709.2092 [hep-ph].

[32] Paolo Nason and Bryan Webber. "Next-to-Leading-Order Event Generators". In: *Ann. Rev. Nucl. Part. Sci.* 62 (2012), pp. 187–213. DOI: 10.1146/annurev-nucl-102711-094928. arXiv: 1202.1251 [hep-ph].

[33] E. Boos et al. "Generic user process interface for event generators". In: *Physics at TeV colliders. Proceedings, Euro Summer School, Les Houches, France, May 21-June 1, 2001*. 2001. arXiv: hep-ph/0109068 [hep-ph]. URL: http://lss.fnal.gov/archive/preprint/fermilab-conf-01-496-t.shtml.

[34] Carlo Oleari. "The POWHEG-BOX". In: *Nucl. Phys. Proc. Suppl.* 205-206 (2010), pp. 36–41. DOI: 10.1016/j.nuclphysbps.2010.08.016. arXiv: 1007.3893 [hep-ph].

[35] http://powhegbox.mib.infn.it.

[36] Johan Alwall et al. "MadGraph 5 : Going Beyond". In: *JHEP* 06 (2011), p. 128. DOI: 10.1007/JHEP06(2011)128. arXiv: 1106.0522 [hep-ph].

[37] https://herwig.hepforge.org/.

[38] https://sherpa.hepforge.org/doc/SHERPA-MC-1.2.0.html.

[39] S. Jadach et al. "Matching NLO QCD with parton shower in Monte Carlo scheme — the KrkNLO method". In: *JHEP* 10 (2015), p. 052. DOI: 10.1007/JHEP10(2015)052. arXiv: 1503.06849 [hep-ph].

[40] Borut Bajc et al. "Threshold Corrections to Dimension-six Proton Decay Operators in Non-minimal SUSY SU(5) GUTs". In: (2016). arXiv: 1603.03568 [hep-ph].

[41] M.Ikeda. "Preliminary results for the Super-Kamiokande Collaboration, presented at NNN2015." In: 2015.

[42] Wei-Shu Hou, Makiko Nagashima, and Andrea Soddu. "Baryon number violation involving higher generations". In: *Phys. Rev.* D72 (2005), p. 095001. DOI: 10.1103/PhysRevD.72.095001. arXiv: hep-ph/0509006 [hep-ph].

[43] https://wiki.classe.cornell.edu/CLEO/WebHome.

[44] http://www.slac.stanford.edu/BFROOT.

[45] https://wiki.jlab.org/clas_chair/index.php/CLAS_Collaboration_Information.

[46] P. Rubin et al. "Search for D0 —> anti-p e+ and D0 —> p e-". In: *Phys. Rev.* D79 (2009), p. 097101. DOI: 10.1103/PhysRevD.79.097101. arXiv: 0904.1619 [hep-ex].

[47] P. del Amo Sanchez et al. "Searches for the baryon- and lepton-number violating decays $B^0 \to \Lambda_c^+ \ell^-$, $B^- \to \Lambda \ell^-$, and $B^- \to \bar{\Lambda} \ell^-$". In: *Phys. Rev.* D83 (2011), p. 091101. DOI: 10.1103/PhysRevD.83.091101. arXiv: 1101.3830 [hep-ex].

[48] M. E. McCracken et al. "Search for baryon-number and lepton-number violating decays of Λ hyperons using the CLAS detector at Jefferson Laboratory". In: *Phys. Rev.* D92.7 (2015), p. 072002. DOI: 10.1103/PhysRevD.92.072002. arXiv: 1507.03859 [hep-ex].

[49] Georges Aad et al. "Measurement of the inclusive and dijet cross-sections of b^- jets in pp collisions at $\sqrt{s} = 7$ TeV with the ATLAS detector". In: *Eur. Phys. J.* C71 (2011), p. 1846. DOI: 10.1140/epjc/s10052-011-1846-4. arXiv: 1109.6833 [hep-ex].

[50] Serguei Chatrchyan et al. "Inclusive b-jet production in pp collisions at $\sqrt{s} = 7$ TeV". In: *JHEP* 04 (2012), p. 084. DOI: 10.1007/JHEP04(2012)084. arXiv: 1202.4617 [hep-ex].

[51] R. Aaij et al. "Measurement of $\sigma(pp \to b\bar{b}X)$ at $\sqrt{s} = 7$ TeV in the forward region". In: *Phys. Lett.* B694 (2010), pp. 209–216. DOI: 10.1016/j.physletb.2010.10.010. arXiv: 1009.2731 [hep-ex].

[52] http://mcfm.fnal.gov.

[53] Matteo Cacciari, Mario Greco, and Paolo Nason. "The P(T) spectrum in heavy flavor hadroproduction". In: *JHEP* 05 (1998), p. 007. DOI: 10.1088/1126-6708/1998/05/007. arXiv: hep-ph/9803400 [hep-ph].

[54] "Measurement of $\sigma(b\bar{b})$ with inclusive final states". In: *LHCb-CONF-2013-002, CERN-LHCb-CONF-2013-002* (2013).

[55] Lyndon Evans and Philip Bryant. "LHC Machine". In: *JINST* 3 (2008), S08001. DOI: 10.1088/1748-0221/3/08/S08001.

[56] http://home.web.cern.ch/about/accelerators/linear-accelerator-2.

[57] http://home.web.cern.ch/about/accelerators/proton-synchrotron-booster.

[58] http://home.web.cern.ch/about/accelerators/proton-synchrotron.

[59] http://home.web.cern.ch/about/accelerators/super-proton-synchrotron.

[60] http://home.cern/about/experiments/lhcb.

[61] http://home.cern/about/experiments/alice.

[62] A. Augusto Alves Jr. et al. "The LHCb Detector at the LHC". In: *JINST* 3 (2008), S08005. DOI: 10.1088/1748-0221/3/08/S08005. URL: http://stacks.iop.org/1748-0221/3/i=08/a=S08005.

[63] J.P.Koutchouk. "Luminosity Optimization and Levelling". In: *Proceedings of Chamonix 2010 workshop on LHC Performance*. 2010.

[64] N. Zaitsev. "Study of the LHCb pile-up trigger and the B/s –> J / psi Phi decay". PhD thesis. Amsterdam U., 2000. URL: http://weblib.cern.ch/abstract?CERN-THESIS-2000-043.

[65] http://lhcb.web.cern.ch/lhcb/speakersbureau/html/bb_ProductionAngles.html.

[66] Roel Aaij et al. "LHCb Detector Performance". In: *Int. J. Mod. Phys.* A30.07 (2015), p. 1530022. DOI: 10.1142/S0217751X15300227. arXiv: 1412.6352 [hep-ex].

[67] https://lbgroups.cern.ch/online/OperationsPlots/2012Plots.html.

[68] R Aaij et al. "The LHCb Trigger and its Performance in 2011". In: *JINST* 8 (2013), P04022. DOI: 10.1088/1748-0221/8/04/P04022. arXiv: 1211.3055 [hep-ex].

[69] R. Aaij et al. "Performance of the LHCb Vertex Locator". In: *JINST* 9 (2014), p. 09007. DOI: 10.1088/1748-0221/9/09/P09007. arXiv: 1405.7808 [physics.ins-det].

[70] Christian Urs Elsasser. "LHCb Silicon Detectors: Operational Experience and Run I to Run II Transition". In: *PoS* Vertex2014 (2015), p. 005.

[71] R. Hierck. "Track following for LHCb". In: (2001).

[72] Johan Luisier. "Performance of LHCb Silicon Tracker Detector in the LHC". In: *Phys. Procedia* 37 (2012), pp. 851–858. DOI: 10.1016/j.phpro.2012.04.097.

[73] http://lhcb.physik.uzh.ch/ST/public/photos.

[74] R Arink et al. "Performance of the LHCb Outer Tracker". In: *JINST* 9.01 (2014), P01002. DOI: 10.1088/1748-0221/9/01/P01002. arXiv: 1311.3893 [physics.ins-det].

[75] Bildgalerie des Physikalischen Institutes. http://www.physi.uni-heidelberg.de/Galerie/allpics.php.

[76] Roel Aaij et al. "Measurement of the track reconstruction efficiency at LHCb". In: *JINST* 10.02 (2015), P02007. DOI: 10.1088/1748-0221/10/02/P02007. arXiv: 1408.1251 [hep-ex].

[77] http://lhcb-release-area.web.cern.ch/LHCb-release-area/DOC/brunel.

[78] http://lhcb-release-area.web.cern.ch/LHCb-release-area/DOC/davinci.

[79] https://cds.cern.ch/record/808276.

[80] "LHCb: RICH technical design report". In: (2000).

[81] Liliana Teodorescu. "Artificial neural networks in high-energy physics". In: *Computing. Proceedings, inverted CERN School of Computing, ICSC2005 and ICSC2006, Geneva, Switzerland, February 23-25, 2005, and March 6-8, 2006*. [,13(2008)]. 2008, pp. 13–22. URL: http://doc.cern.ch/yellowrep/2008/2008-002/p13.pdf.

[82] http://twiki.cern.ch/twiki/bin/view/LHCb/GlobalParticleID.

[83] http://hepwww.rl.ac.uk/lhcb/RAEJune08/RAE.htm.

[84] M. Adinolfi et al. "Performance of the LHCb RICH detector at the LHC". In: *Eur. Phys. J.* C73 (2013), p. 2431. DOI: 10.1140/epjc/s10052-013-2431-9. arXiv: 1211.6759 [physics.ins-det].

[85] Eduardo Picatoste Olloqui. "LHCb preshower(PS) and scintillating pad detector (SPD): Commissioning, calibration, and monitoring". In: *J. Phys. Conf. Ser.* 160 (2009), p. 012046. DOI: 10.1088/1742-6596/160/1/012046.

[86] https://cds.cern.ch/record/1329572.

[87] S. Barsuk. "The Shashlik electro-magnetic calorimeter for the LHCb experiment". In: *Calorimetry in particle physics. Proceedings, 11th International Conference, CALOR 2004, Perugia, Italy, March 29-April 2, 2004*. 2004, pp. 61–67.

[88] Frédéric Machefert. "First years of running of the LHCb calorimeter system". In: *Nucl. Instrum. Meth.* A787 (2015), pp. 373–375. DOI: 10.1016/j.nima.2015.01.097.

[89] https://cds.cern.ch/record/835712.

[90] https://cds.cern.ch/record/865949.

[91] R Aaij et al. "Implications of LHCb measurements and future prospects". In: *Eur. Phys. J.* C73.4 (2013), p. 2373. DOI: 10.1140/epjc/s10052-013-2373-2. arXiv: 1208.3355 [hep-ex].

[92] F. Archilli et al. "Performance of the Muon Identification at LHCb". In: *JINST* 8 (2013), P10020. DOI: 10.1088/1748-0221/8/10/P10020. arXiv: 1306.0249 [physics.ins-det].

[93] https://cds.cern.ch/record/1075729.

[94] S Tolk et al. *Data driven trigger efficiency determination at LHCb*. Tech. rep. LHCb-PUB-2014-039. CERN-LHCb-PUB-2014-039. Geneva: CERN, 2014. URL: https://cds.cern.ch/record/1701134.

[95] R Aaij et al. "Measurement of the Λ_b^0, Ξ_b^- and Ω_b^- baryon masses". In: *Phys. Rev. Lett.* 110.18 (2013), p. 182001. DOI: 10.1103/PhysRevLett.110.182001. arXiv: 1302.1072 [hep-ex].

[96] Roel Aaij et al. "Precision measurement of the mass and lifetime of the Ξ_b^0 baryon". In: *Phys. Rev. Lett.* 113 (2014), p. 032001. DOI: 10.1103/PhysRevLett.113.032001. arXiv: 1405.7223 [hep-ex].

[97] Roel Aaij et al. "Precision measurement of the ratio of the Λ_b^0 to $\overline{B}^0$ lifetimes". In: *Phys. Lett.* B734 (2014), pp. 122–130. DOI: 10.1016/j.physletb.2014.05.021. arXiv: 1402.6242 [hep-ex].

[98] R. Aaij et al. "Measurement of b-hadron production fractions in $7\ \mathrm{TeV pp}$ collisions". In: *Phys. Rev.* D85 (2012), p. 032008. DOI: 10.1103/PhysRevD.85.032008. arXiv: 1111.2357 [hep-ex].

[99] http://twiki.cern.ch/twiki/bin/viewauth/LHCbPhysics/RareDecays?redirectedfrom=LHCb.RareDecays.

[100] A. Abulencia et al. "Search for $B_s \to \mu^+\mu^-$ and $B_d \to \mu^+\mu^-$ decays in $p\bar{p}$ collisions with CDF II". In: *Phys. Rev. Lett.* 95 (2005). [Erratum: Phys. Rev. Lett.95,249905(2005)], p. 221805. DOI: 10.1103/PhysRevLett.95.221805. arXiv: hep-ex/0508036 [hep-ex].

[101] Pushpalatha C. Bhat. "Multivariate Analysis Methods in Particle Physics". In: *Ann. Rev. Nucl. Part. Sci.* 61 (2011), pp. 281–309. DOI: 10.1146/annurev.nucl.012809.104427.

[102] http://twiki.cern.ch/twiki/bin/view/LHCb/PIDCalibPackage.

[103] Jan Therhaag. "TMVA: Toolkit for multivariate data analysis". In: *AIP Conf. Proc.* 1504 (2009), pp. 1013–1016. DOI: 10.1063/1.4771869.

[104] Byron P. Roe et al. "Boosted decision trees, an alternative to artificial neural networks". In: *Nucl. Instrum. Meth.* A543.2-3 (2005), pp. 577–584. DOI: 10.1016/j.nima.2004.12.018. arXiv: physics/0408124 [physics].

[105] Leo Breiman et al. *Classification and regression trees*. Chapman and Hall/CRC, 1984. ISBN: 0412048418, 9780412048418.

[106] Yoav Freund and Robert E. Schapire. "A Decision-Theoretic Generalization of On-Line Learning and an Application to Boosting". In: *J. Comput. Syst. Sci.* 55.1 (1997), pp. 119–139. DOI: 10.1006/jcss.1997.1504.

[107] Muriel Pivk and Francois R. Le Diberder. "SPlot: A Statistical tool to unfold data distributions". In: *Nucl. Instrum. Meth.* A555 (2005), pp. 356–369. DOI: 10.1016/j.nima.2005.08.106. arXiv: physics/0402083 [physics.data-an].

[108] Thomas Junk. "Confidence level computation for combining searches with small statistics". In: *Nucl. Instrum. Meth.* A434 (1999), pp. 435–443. DOI: 10.1016/S0168-9002(99)00498-2. arXiv: hep-ex/9902006 [hep-ex].

[109] Wouter Verkerke and David P. Kirkby. "The RooFit toolkit for data modeling". In: *eConf* C0303241 (2003). [,186(2003)], MOLT007. arXiv: physics/0306116 [physics].

[110] F. James and M. Roos. "Minuit: A System for Function Minimization and Analysis of the Parameter Errors and Correlations". In: *Comput. Phys. Commun.* 10 (1975), pp. 343–367. DOI: 10.1016/0010-4655(75)90039-9.

[111] Tomasz Skwarnicki. "A study of the radiative CASCADE transitions between the Upsilon-Prime and Upsilon resonances, Appendix E". PhD thesis. Cracow, INP, 1986. URL: http://lss.fnal.gov/cgi-bin/find_paper.pl?other/thesis/skwarnicki.pdf.

[112] Roel Aaij et al. "Precision luminosity measurements at LHCb". In: *JINST* 9.12 (2014), P12005. DOI: 10.1088/1748-0221/9/12/P12005. arXiv: 1410.0149 [hep-ex].

[113] Andreas Jaeger et al. "Measurement of the track finding efficiency". In: (2012).

[114] http://uk.mathworks.com/help/matlab/ref/randn.html.

[115] Alexander L. Read. "Presentation of search results: The CL(s) technique". In: *J. Phys.* G28 (2002). [,11(2002)], pp. 2693–2704. DOI: 10.1088/0954-3899/28/10/313.

[116] http://cyfronet.krakow.pl/en/4421,main.html.

[117] "Search for Higgs-like bosons decaying into long-lived exotic particles". In: *LHCb-CONF-2012-014, CERN-LHCb-CONF-2012-014* (2012).

[118] R Aaij et al. "Prompt charm production in pp collisions at sqrt(s)=7 TeV". In: *Nucl. Phys.* B871 (2013), pp. 1–20. DOI: 10.1016/j.nuclphysb.2013.02.010. arXiv: 1302.2864 [hep-ex].

[119] http://proj-gaudi.web.cern.ch/proj-gaudi.

[120] http://lhcb-release-area.web.cern.ch/LHCb-release-area/DOC/gauss.

[121] http://home.thep.lu.se/~torbjorn/Pythia.html.

[122] http://www.slac.stanford.edu/~lange/EvtGen.

[123] https://geant4.web.cern.ch/geant4.

[124] http://lhcb-release-area.web.cern.ch/LHCb-release-area/DOC/moore/.

[125] http://lhcb-release-area.web.cern.ch/LHCb-release-area/DOC/boole.

[126] I. Belyaev et al. "Handling of the generation of primary events in Gauss, the LHCb simulation framework". In: *J. Phys. Conf. Ser.* 331 (2011), p. 032047. DOI: 10.1088/1742-6596/331/3/032047.

[127] Johan Alwall et al. "A Standard format for Les Houches event files". In: *Comput. Phys. Commun.* 176 (2007), pp. 300–304. DOI: 10.1016/j.cpc.2006.11.010. arXiv: hep-ph/0609017 [hep-ph].

[128] http://lhcb-release-area.web.cern.ch/LHCb-release-area/DOC/decfiles.